

Andreas G. Strand

The Application of Spaceborne GNSS-Reflectometry for the Study of Ocean Microplastics

Master's thesis in Engineering and ICT

Supervisor: Hossein Nahavandchi

Co-supervisor: Mostafa Hoseini

July 2021

Andreas G. Strand

The Application of Spaceborne GNSS-Reflectometry for the Study of Ocean Microplastics

Master's thesis in Engineering and ICT
Supervisor: Hossein Nahavandchi
Co-supervisor: Mostafa Hoseini
July 2021

Norwegian University of Science and Technology
Faculty of Engineering
Department of Civil and Environmental Engineering



Abstract

From the production of oxygen, food and medicine to transportation and maritime economy, the world oceans play a crucial role in human society. For decades remote sensing satellites have been monitoring the oceans using different methods through microwave signals or optical images. However, a novel technique that has recently drawn attention is remote sensing using the reflected signals of Global Navigation Satellite Systems (GNSS), or GNSS-Reflectometry (GNSS-R). In this thesis, the application of spaceborne GNSS-R observations for detecting and monitoring oceanic microplastics has been studied. A multi-purpose web-based software has been developed and used for the analysis. The study utilizes a large dataset from a NASA GNSS-R mission called Cyclone GNSS (CYGNSS). The dataset covers a period of over four years, from 2017 to 2021. The parameter used for the analysis is the Normalized Bi-static Radar Cross Section (NBRCS) which is retrieved from the Level-1 product of the mission. The NBRCS values are collocated with matchup wind data from European Center for Medium-range Weather Forecast (ECMWF) Re-Analysis (ERA5). The anomalies in NBRCS are investigated to detect abrupt changes which are linked to the presence of microplastics. The microplastics, along with surfactants, can reduce surface stress and suppressing ocean surface roughness. The results of the distribution of microplastics are compared to the available microplastics models. The analogy shows a good agreement with the models suggesting that the spaceborne GNSS-R can be a promising tool for tracking microplastics over the ocean.

Sammendrag

Fra produksjonen av oksygen, mat og medisin til transport og maritim økonomi, spiller verdenshavene en avgjørende rolle i det menneskelige samfunn. Over flere tiår har fjernmåling satellitter overvåket havene ved hjelp av ulike metoder gjennom mikrobølgesignaler eller optiske bilder. Midlertid har en ny teknikk nylig trukket mye oppmerksomhet, nemlig fjernmåling ved hjelp av reflekterte signaler fra Global Navigation Satellite Systems (GNSS), eller GNSS-reflektometri (GNSS-R). I denne oppgaven er anvendelsen av rombaserte GNSS-R observasjoner for å oppdage og overvåke mikroplast i havet studert. En flerbruksbasert programvare er utviklet og benyttet for analysen. Dette studie bruker et stort datasett fra NASA GNSS-R oppdraget kalt Cyclone GNSS (CYGNSS). Dette datasettet dekker en periode på over fire år fra 2017 til 2021. Variabelen brukt for analysen er Normalized Bi-static Radar Cross Section (NBRCS) som er hentet fra Nivå 1-produktet av oppdraget. NBRCS verdiene er samlet med samsvarende vinddata fra European Center for Medium-Range Weather Forecast (ECMWF) Re-Analysis (ERA5). Avvikene i NBRCS blir undersøkt for å oppdage brå endringer knyttet til tilstedeværelsen av mikroplast. Mikroplast, i tillegg til andre overflateliggende stoffer, kan redusere overflatespenningen ved å svekke småbølger. Resultatet fra distribusjonen av mikroplast blir sammenlignet med de tilgjengelige mikroplastmodellene. Analogien viser en god sammenheng med modellene som antyder at rombasert GNSS-R kan være et lovende verktøy for å spore mikroplast over havet.

Preface

This Master's thesis concludes my Master of Science in Engineering and ICT with a specialization in Geomatics at the Norwegian University of Science and Technology (NTNU).

Foremost, I would like to express my sincerest gratitude to my supervisor, Professor Hossein Nahavandchi and my co-supervisor, Mostafa Hoseini, whose continuous support, patience, and valuable help have been critical for the work and writing of this thesis.

I would also like to extend my gratitude to my parents, Mary-Gunn Gaustadnes and Jan-Erik Strand, for all the encouragement and support during my years as a student.

Finally, I would like to thank all my friends and fellow students who have made my years as a student some of the best years I have experienced this far.

Andreas Gaustadnes Strand
July 2021.

Contents

Abstract	i
Sammendrag	ii
Preface	iii
Contents	iv
List of Figures	vii
List of Tables	viii
Acronyms	xi
1 Introduction	1
1.1 Background	1
1.2 Main Objectives and Goals	4
1.3 Outline	5
2 The Theoretical Background	7
2.1 Basic Principles	7
2.1.1 Delay-Doppler Maps	8
2.1.2 The GNSS-R Bi-static Radar Equation	9
2.1.3 Mean Square Slope	10
2.2 Examples of GNSS-R Applications	12
2.2.1 Altimetry	12
2.2.2 Wind Speed Estimations	14
2.2.3 Soil Moisture and Vegetation	16
2.2.4 The Cryosphere	17
2.2.5 The Detection of Microplastics	18
3 The Issue of Microplastics In the Ocean	19
3.1 The Origins of Microplastics	20
3.2 Consequences of Microplastics	22
3.3 Remote Sensing of Marine Debris	23
4 Data-set Description	25
4.1 Cyclone Global Navigation Satellite System	25
4.2 ECMWF Reanalysis v5 (ERA5)	27
4.3 Global Estimation Models of Microplastics	28

5	Data handling & Methodology	33
5.1	A Web-based GNSS-Reflectometry Toolbox	33
5.1.1	Data Collection	35
5.1.2	Track Demonstration Tool	37
5.1.3	Data Clipping Tool	39
5.1.4	Ground-based GNSS-R	41
5.2	Detection of Microplastics	44
6	Results & Discussion	53
6.1	A Global Picture	53
6.1.1	The Effect of Ocean Currents	55
6.1.2	Seasonal Changes in Data	56
6.1.3	Average Global Peak Density	58
6.2	Inspection of Basins	59
6.2.1	The North Pacific Ocean	59
6.2.2	The South Pacific Ocean	61
6.2.3	The North Atlantic Ocean	64
6.2.4	The South Atlantic Ocean	66
6.2.5	The Indian Ocean	69
6.2.6	The Mediterranean Sea	71
7	Conclusion	75

List of Figures

1.1	GNSS-Reflectometry concept	2
1.2	Render of a CYGNSS satellite	3
2.1	Example of reflection on a beach	8
2.2	Example of a Delay Doppler Map (DDM)	9
2.3	Example of altimetric measurements	13
2.4	Example of a simulated tropical cyclone	14
2.5	Example of CYGNSS wind measurements	15
2.6	Example of soil moisture maps	16
2.7	Example of sea Surface characterizations	17
2.8	Example of monthly average microplastic concentrations	18
3.1	Image of beach littered with plastic	20
3.2	Info-graphic of microplastic entering the food chain	22
3.3	Example of SAR	24
4.1	The spatial coverage of the CYGNSS satellite tracks	26
4.2	ERA5 processed wind data	27
4.3	Microplastic data collected from trawl data	28
4.4	the Maximenko model for microplastic distribution	29
4.5	the Lebreton model for microplastic distribution	30
4.6	the van Sebille model for microplastic distribution	31
5.1	Web-tool interaction diagram	34
5.2	Track demonstration tool user interface	37
5.3	Track demonstration presentation	38
5.4	Track demonstration plot	38
5.5	Data clipping tool user interface	39
5.6	GNSS-R sea surface products	41
5.7	Observation details	42
5.8	Observation details table	42
5.9	Observation representation panel	43
5.10	Fresnel coefficient power loss	44
5.11	Variation of Fresnel coefficient	45
5.12	Parameters affecting power loss	46
5.13	Simulation of NBRCS from MSS values	47
5.14	Track representation	50

6.1	Global peak density	53
6.2	Global peak prominence	54
6.3	Global peak widths	55
6.4	Global map of currents	55
6.5	Higher winds global peak density	56
6.6	Seasonal global peak density	57
6.7	Global peak density time series	58
6.8	North Pacific comparison	59
6.9	North Pacific peak density	60
6.10	South Pacific comparison	61
6.11	South Pacific peak density	62
6.12	Time series for the Pacific ocean	63
6.13	North Atlantic comparison	64
6.14	North Atlantic peak density	65
6.15	South Atlantic comparison	66
6.16	South Atlantic peak density	67
6.17	Time series for the Atlantic ocean	68
6.18	Indian ocean comparison	69
6.19	Indian ocean peak density	70
6.20	Mediterranean sea comparison	71
6.21	Mediterranean sea peak density	72
6.22	Time series for the Mediterranean sea and Indian ocean	73

List of Tables

5.1	Collected CYGNSS variables	47
-----	--------------------------------------	----

Acronyms

BRCS	Bi-static Radar Cross Section
CYGNSS	Cyclone Global Navigation Satellite System
dB	Decibel
DDMA	Delay Doppler Map Average
DDMI	Delay Doppler Mapping Instrument
DDM	Delay Doppler Map
DMC	Disaster Monitoring Constellation
ECMWF	European Centre for Medium-Range Weather Forecasts
ERA5	ECMWF Reanalysis v5
GFZ	German Research Centre for Geosciences
GLONASS	Globalnaya Navigazionnaya Sputnikovaya Sistema, or Global Navigation Satellite System
GNSS-R	GNSS Reflectometry
GNSS	Global Navigation Satellite System
GPS	Global Positioning System
IMERG	Integrated Multi-satellite Retrievals for Global Precipitation Measurement
IRNASS	Indian Regional Navigation Satellite System
JSON	JavaScript Object Notation
LEO	Low Earth Orbit
LES	Leading Edge Slope
LHCP	Left-Handed Circular polarization
MSS	Mean Square Slope
NASA	National Aeronautics and Space Administration
NBRCS	Normalized Bi-static Radar Cross Section
NetCDF	Network Common Data Form

NOAA	National Oceanic and Atmospheric Administration
OPeNDAP	Open-source Project for a Network Data Access Protocol
OSCAR	Ocean Surface Current Analyses Real-time
PDF	Probability Density Function
PODAAC	Physical Oceanography Data Active Archive Center
PRN	Pseudorandom Noise
QZSS	Quasi-Zenith Satellite System
RHCP	Right-Handed Circular polarization
SAR	Synthetic Aperture Radar
SMIGOL	Soil Moisture Interference-pattern GNSS Observations at L-band
SP	Specular Point
SSH	Sea Surface Height
SSR	Sea Surface Roughness

Chapter 1

Introduction

The first part of this thesis will introduce the background and motivations behind GNSS-Reflectometry for different remote sensing applications. Additionally, we will present the objectives and our general approach. Lastly, we will provide an outline for the succeeding chapters.

1.1 Background

Ever since the early days of space technology, satellites have been used for geodetic purposes. As a result, this technology became an excellent supplement and competitor to the existing classical means of measure. In addition, it paved the way for a wealth of resources in surveying and navigation services. Today there are several operational, fully global satellite constellations maintained by various authorities. Such systems are called Global Navigation Satellite Systems (GNSS) and provide positioning, navigation, and timing services globally or on a regional scale.

Today there exists four fully operational GNSS, the American GPS (Global Positioning System), the Russian GLONASS, the Chinese BeiDou, and the European Galileo. Additionally, there are two regional systems; the Japanese QZSS and the Indian IRNSS/-NavIC. GPS and GLONASS became fully operational during the 90s, while BeiDou and Galileo did not become fully operational until recent years. While these systems were mainly created with global navigation in mind, it quickly became apparent that signals originating from GPS and other GNSS can be used for more than just navigation. One such usage is Earth remote sensing; Using satellites to gather information about the Earth.

One such technique is GNSS-Reflectometry (GNSS-R). This technique collects and analyzes reflected GNSS signals from different surfaces on the Earth to retrieve geophysical properties of the reflecting surface. The processing of such signals can give information about oceanography, soil moisture, vegetation, snow depth, sea ice thickness, and more, as presented by Cardellach et al [8]. It was Hall & Cordey who initially discussed the feasibility of using signals reflected off the Earth's surface for scatterometry purposes in 1988 [22]. The idea of using the GPS reflected signals for mesoscale altimetry was proposed in 1993 by Martin-Neira [33]. A few years later, Garrison and Katzberg performed an aircraft experiment, demonstrating that reflected GNSS signals could be used for sensing ocean surface roughness and related winds [17].

The applications of GNSS-R regarding the retrieval of sea surface heights (altimetry) and the measurements of ocean surface wind velocity and mean square slope (scatterometry) are the applications that have gotten the most attention. A good reason for reflectometry to become a popular method for these applications is probably stems from the low cost and low power characteristics of the GNSS-R receivers. These features allow the production of many micro-satellites that can be synchronised into a satellite constellation to retrieve a high sampling rate of Earth observations at a relatively low cost.

Transmitted signals by GNSS satellites are forward scattered from the Earth surface in a bi-static specular direction. In Figure 1.1 an example of the bi-static remote sensing concept is presented. Here the GNSS satellite acts as a transmitter while either an airplane or a Low Earth Orbit (LEO) satellite acts as the receiving platform. A receiver can also be placed on the land in order to do ground-based measurements.

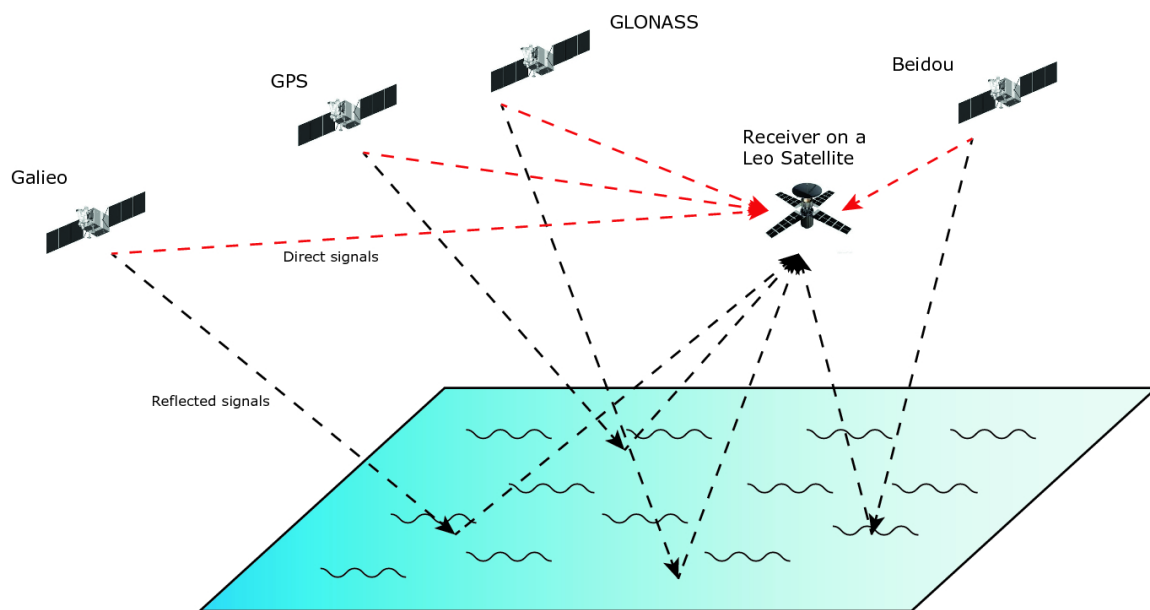


Figure 1.1: An illustration of the concept of GNSS-Reflectometry as a Bi-static remote sensing technique. The GNSS transmitters send a direct signal to the Low Earth Orbit (LEO) receiver shown in red lines, while the black lines represent the reflected signals bouncing off the ocean surface. Source: [2].

There are several advantages of GNSS-Reflectometry remote sensing. Firstly, GNSS-R receivers require low power and are relatively cheaper than their counterparts. Additionally, using the already widely available GNSS network means that only the production of receivers is necessary as the GNSS satellites themselves act as transmitters, and the high availability of GNSS provides a precise and continuous source of signals.

The propagation of the GNSS signals in space is in the L-band spectrum of radio frequencies. The result from this is that the weather does not affect the quality of the signal, and GNSS-R measurements are suitable for working in all weather conditions, both day and night time. Furthermore, since the GNSS spread-spectrum communication technology is involved, it also enables the retrieval of weak signals.

There have been several spaceborne missions with GNSS-R sensors as a one of the payloads. For example, in 2003, the international program Disaster Monitoring Constellation (DMC) launched the satellite UK-DMC-1G with the goal of experimentation on new technologies, GNSS Reflectometry being one of them. The objective of this experiment was to demonstrate the capability of GNSS-R measurements for sensing Earth surface geophysical parameters. The results from this mission gave valuable verification and opened up the opportunity of having space-based bi-static radar remote sensing [28].

In 2016 NASA launched the GNSS-Reflectometry system, Cyclone Global Navigation Satellite System (CYGNSS), as a part of the System Science Pathfinder Mission. This constellation of eight micro-satellites has the scientific objective of collecting frequent space-based measurements of wind speeds in the inner core of tropical cyclones. By analysing the data products from this mission, the relationship between various surface properties, thermodynamics, heat transfers and dynamics of an inner core of a tropical cyclone can be studied [38].

The CYGNSS satellites operate in a near-circular, non-synchronous orbit at approximately 510 kilometres above the earth surface, with an inclination of 35 degrees from the equator. These orbital parameters allow the satellites to obtain measurements of the ocean surface winds between the latitudes of 38° North and 38° South, which is the critical latitude band for the formation and movement of tropical cyclones [38].

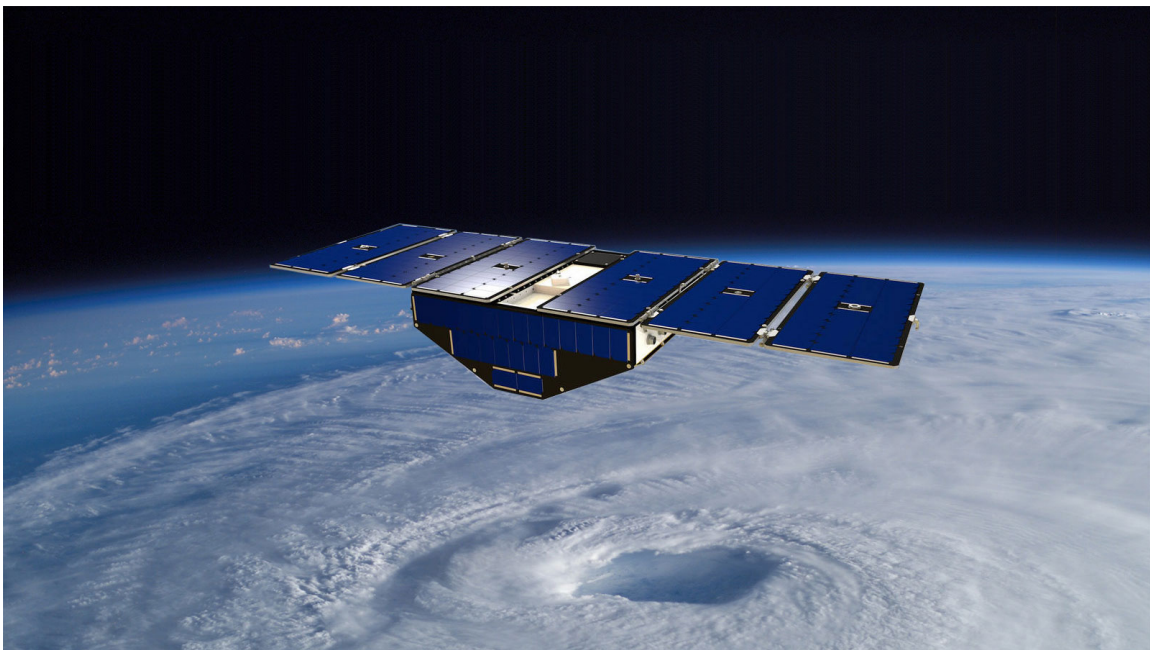


Figure 1.2: An image of a Cyclone Global Navigation Satellite Systems (CYGNSS) microsatellite in orbit above the Earth. Source: [38]

The information gathered in the CYGNSS dataset can, however, be used for many additional purposes. For example, research has proved that observations from the CYGNSS dataset show the potential to map inland surface water [18], imaging of flooding events [50], the measure of near-surface soil moisture [11] and even for detecting mesoscale oceanic features [23]. In this thesis, we will look into the possibility of mapping microplastic density in the ocean.

1.2 Main Objectives and Goals

The main objective of this thesis is to investigate the application of spaceborne GNSS-Reflectometry for the study of oceans, in particular monitoring the oceanic microplastics distribution. The spaceborne GNSS-R measurements provided by CYGNSS mission has a relatively short revisit time (~ 7 hours). This stimulates research topics for different applications including very novel application for ocean microplastics monitoring which is studied in this thesis. To get a brief overview of the scope for this thesis, we have condensed it into two primary objectives:

1. Create a web-based software toolbox for the collection, processing and presentation of GNSS-R data.
2. Use recent GNSS-R data in a study to explore the possibility of monitoring microplastics in the ocean.

For the first objective, several issues need to be dealt with. We need to decide on the technologies and frameworks used to create and facilitate the web application and decide on the methodologies and structures used for this project's scope. We also need to achieve good knowledge of the datasets available and decide how to handle the data.

As this will be a web-based service, there will also be a need to facilitate the system's user-friendliness to make it intuitive and efficient to utilize. Therefore, for this application, we want to create several tools that can be used to explore and interact with the dataset of interest. The tools we want to provide for the users are the following.

- A tool that allows the user to select a region, date and variables of interest that presents the relevant data on an interactive map.
- A data clipping tool allowing the user to trim down large portions of the dataset to only download necessary variables and parameters within specified regions and times.
- An example showcase for ground-based GNSS-R data products based on the collected data from a station located at Onsala, Sweden.

The second objective will take advantage of the tools created as a part of the toolbox and present a study on the feasibility of detecting microplastics in the ocean using GNSS-R data. For this task, we need to look into research on microplastics, and by using relevant datasets, try to find correlations between the parameters in the processed data and the concentration of microplastics on the ocean surface.

1.3 Outline

The remaining parts of this thesis are organized into the following chapters: *The Theoretical Background*, *The Issue of Microplastics In the Ocean*, *Data-set Description*, *Data handling & Methodology*, *Results & Discussion* ending with the *Conclusion*.

In **Chapter 2 - The Theoretical Background**, the prerequisite theoretical knowledge which this project is based upon is presented. The relevant theory regarding the collection and processing of the GNSS-R technique is presented. In the last section of the chapter, several GNSS-Reflectometry applications are presented and briefly explained.

In **Chapter 3 - The Issue of Microplastics In the Ocean**, we present the global issue of microplastics contaminating the ocean waters. We start by briefly discuss the origin and consequences of microplastics, then we present some methods of detecting microplastics using remote sensing.

In **Chapter 4 - Data-set Description**, we present the primary GNSS-R dataset, the NASA CYGNSS data product. After this, we present the ancillary ERA5 dataset from which the wind speeds are collected. Finally, we introduce The matchup dataset for verification, widely accepted models of global microplastics.

In **Chapter 5 - Data handling & Methodology**, we first present the web-based GNSS-R toolbox by explaining how the data is collected and elaborating on the proposed methods for each of the three tools developed. In the second part of the chapter, we introduce the motivations and methods used to detect microplastics using the GNSS-R dataset.

In **Chapter 6 - Results & Discussion**, we present the results from our effort to use GNSS-R data to detect microplastics. We start by showing the global results for several variables and other changes from external factors and finish the chapter by taking a closer look into the results at six major oceanic basins.

In **Chapter 7 - Conclusion**, we present our conclusions and introduce some ideas for future relevant work.

Chapter 2

The Theoretical Background

This chapter will give an overview of the theoretical foundation and various factors of the GNSS-Reflectometry technique utilised in the scope of this thesis. It will also present several examples of GNSS-R applications.

2.1 Basic Principles

The GNSS-Reflectometry technique aims to derive geophysical properties by analysing the reflections of GNSS signals originating from the Earth's reflective surfaces. This technique is a multiple bi-static radar, meaning that the transmitters and receivers are at a significant distance from each other. The technique is a passive remote sensing approach which takes advantage of the already available GNSS systems as the transmitters.

There has been many theories and experiments performed that has demonstrated the extraction of useful information using reflected GNSS signals. This information has been used for several applications such as altimetry, ocean scatterometry and wind measurements, examination of soil moisture and vegetation, monitoring of snow and sea ice density, and maybe even for detecting microplastics. More about these applications can be found in section 2.2.

One of the most prominent reflective surfaces of the Earth is the oceans, so naturally, much of the work done in the GNSS-R field focuses on retrieving oceanographic parameters. Much movement in the water creates more unevenness in the ocean surface which means that the signal spreads more, and it gets a scattered reflection. Figure 2.1 gives an example of reflection in water. Here, the water that has washed over the beach is still and creates a mirror-like effect, or coherent reflection, while where the waves occur roughens the surface leading to incoherent reflection.

As the signal propagation, orbital parameters, the transmitting power and antenna properties of both the receiver and transmitter are known, it is possible to create a theoretical model on how the ocean surface should reflect the GNSS signal given unknown parameters like wind speeds and wave heights. Then, by processing the signals, one can estimate the parameters best fitting with the actual recorded reflection data, which can infer the surface roughness or wind speeds over the ocean.



Figure 2.1: The image was taken at Cannon Beach, Oregon. Showing a good reflection of the stones in the background where the water on the beach is still. Source: [3].

2.1.1 Delay-Doppler Maps

A GNSS-reflectometry receiver measures the power of the GPS signal scattered by the ocean surface after the signal has been filtered by a time delay and a Doppler shift to create a Delay Doppler Map (DDM). An example of a DDM is presented in figure 2.2. The time delay is the difference between the arrival time of the direct signal (propagating directly from the GPS satellite transmitter to the GNSS-R receiver) and the signal scattered and reflected by the ocean surface. The Doppler shift is the difference in frequency between the received direct signal, and the received ocean-scattered signal [43].

There are variations of both the time and Doppler delay in the DDM across a range, including the nominal Specular Point (SP) on the surface. A shorter delay corresponds to locations above the surface with no significant scattered signal, while longer delays can be mapped to iso-delay contours on the surface surrounding the SP. In addition, variations of the Doppler of the scattered signals can also be mapped to iso-Doppler contours on the surface that intersect the delay contours to create the DDM. The DDM can be thus be seen as a map of the diffuse surface scattering in the vicinity of the nominal SP.

The transformation between spatial location on the sea surface and location in the DDM is one to one at the DDM specular location but can have ambiguities outside the specular region (i.e., multiple spatial locations mapped to the same DDM location).

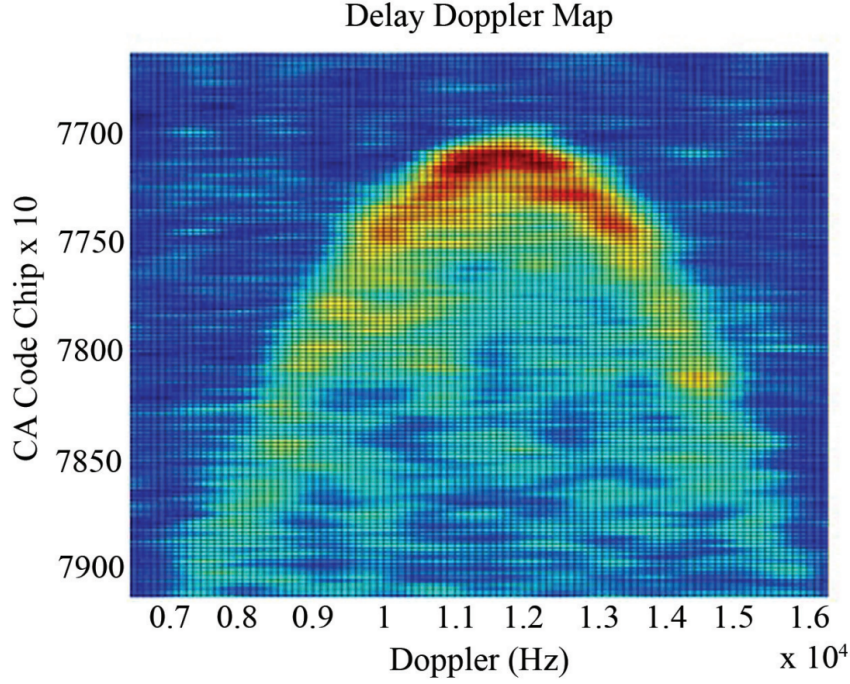


Figure 2.2: Example of a Delay Doppler Map (DDM). This image shows the spatial distribution of the ocean surface scattering (in time delay and Doppler frequency coordinates) measured by the UK-DMC-1 mission. Source: [43]

The Delay Doppler Mapping Instrument (DDMI) on the receiver measure raw uncalibrated units called "counts". The counts are linearly proportional to the energy collected in a bin, and by dividing this by time and calibrating for noise from the antenna and the Earth, the results are the average power. In other words, each bin in the raw count DDM is converted into the received signal power P_g in the unit of watts as shown in equation 2.1 [20].

$$P_g = \frac{(C - C_N)(P_B + P_r)}{C_B} \quad (2.1)$$

Here, P_g is the signal power, C is the DDM value in counts for each delay/Doppler bin, C_N is the noise measurement for each DDM bin, P_B is the blackbody target power measured by a temperature sensor, P_r is the calibrated receiver noise power, and C_B is the blackbody target measurement made within 30 seconds of the DDM measurement.

2.1.2 The GNSS-R Bi-static Radar Equation

Using knowledge of the orbit of both the CYGNSS spacecraft and the GPS spacecraft, the centre location of the mirror-like specular reflection can be estimated. This knowledge can be used along with the received power to calculate σ , the Bi-static Radar Cross Section (BRCS) for each DDM pixel in the unit square meter as shown in equation 2.2 [21].

$$\bar{\sigma}_{\hat{\tau}_i, \hat{f}_j} = \frac{P_{g, \hat{\tau}, \hat{f}} (4\pi)^3 L_{a1} L_{a2} I_{\hat{\tau}, \hat{f}}}{P^T \lambda^2 G_{SP}^T G_{SP}^R R_{SP}^{Total}} \quad (2.2)$$

In this equation, $P_{g,\hat{\tau},\hat{f}}$ is the signal power from equation 2.1 at specific delay ($\hat{\tau}$) and Doppler (\hat{f}) bin. L_{a1} & L_{a2} are estimated atmospheric loss correction from the transmitter to the surface and from the surface to the receiver, respectively. $I_{\hat{\tau},\hat{f}}$ is a term describing the correction for various losses introduced by the DDMI. P^T & G_{SP}^T are the GPS satellite transmit power and antenna gain at the specular point. G_{SP}^R is the receiver antenna gain at the specular point, and R_{SP}^{Total} is the overall range loss from the transmitter to the surface and from the specular point SP on the surface to the receiver.

A delay Doppler bin contains the scattered power across various regions on the ocean surface, and each bin will vary in both physical size and effective area. The GPS ambiguity function on both the delay and Doppler will increase the effective area of each delay Doppler bin, spreading the observed power to adjacent bins from outside the physical scattering area, affecting the level of overall processed power.

The effective area of surface scattering for each delay Doppler bin, $\bar{A}_{\hat{\tau}_i}$ is expressed as the ambiguity function weighted surface integration, shown in equation 2.3.

$$\bar{A}_{\hat{\tau}_i} = \iint_A \Lambda_{\hat{\tau};x,y}^2 S_{\hat{f};x,y}^2 dx dy \quad (2.3)$$

In this equation the delay spreading function, $\Lambda_{\hat{\tau};x,y}^2$ and the Doppler spreading function, $S_{\hat{f};x,y}^2$ are integrated over the surface corresponding to each individual delay/Doppler bin.

The DDM of the BRCS σ from equation 2.2 and the DDM from the effective scattering area $\bar{A}_{\hat{\tau}_i}$ from equation 2.3 can be combined to calculate the Normalized Bistatic Radar Cross Section (NBRCS) value, or σ_0 , over selected regions of the DDM measurements called the DDMA (Delay Doppler Map Average). This calculation is shown in equation 2.4.

$$\bar{\sigma}_0 = \frac{\bar{\sigma}_{total}}{\bar{A}_{total}} = \frac{\sum_{i=1}^N \sum_{j=1}^M \bar{\sigma}_{\hat{\tau}_i, \hat{f}_j}}{\sum_{i=1}^N \sum_{j=1}^M \bar{A}_{\hat{\tau}_i, \hat{f}_j}} \quad (2.4)$$

For this equation, N and M represent the delay and Doppler bin in the σ DDM, respectively. The normalized radar cross-section (NBRCS) σ_0 can then be further calibrated to estimate the ocean wind speed or the Mean Square Slope (MSS) measurement of sea surface roughness.

2.1.3 Mean Square Slope

The mean square slope (MSS) of the ocean surface is a critical parameter for understating the air-sea processes and interpreting altimetric and scatterometric measurements. The CYGNSS algorithm theoretical basis document does an excellent job of explaining the steps necessary to show the connection between the MSS and the NBRCS values [52].

In the geometric optics limit of the Kirchhoff approximation, the NB RCS can be described as shown in equation 2.5.

$$\sigma_0 = \pi |\mathfrak{R}|^2 \left(\frac{q}{q_z}\right)^4 P\left(\frac{-q_\perp}{q_z}\right) \quad (2.5)$$

Here \vec{q} is the scattering vector being the function of coordinate \vec{q} in the mean surface plane, \mathfrak{R} is the complex Fresnel coefficient, which is dependent on the signal polarization, the dielectric constant of the reflecting surface and the local incidence angle. The polarization state of the GNSS-R reflected signals is mostly left-hand circular polarization (LHCP) except for very high incidence angles.

The last factor $P(\vec{s})$ is called the probability density function (PDF) of the large-scale smoothed surface slopes. The linear surface gravity waves PDF, $P(\vec{s})$, can be approximated using the anisotropic bivariate Gaussian distribution given in the wind direction along the x or y axis. This function in combination with 2.5 will give us equation 2.6.

$$\sigma_0(\vec{q}) = \frac{|\mathfrak{R}|^2 (q/q_z)^4}{2\sqrt{mss_x mss_y (1 - b_{x,y}^2)}} \exp\left[-\frac{1}{2q_z^2 (1 - b_{x,y}^2)} \left(\frac{q_x^2}{mss_x} - \frac{2b_{x,y} q_x q_y}{\sqrt{mss_x mss_y}} + \frac{q_y^2}{mss_y}\right)\right] \quad (2.6)$$

For this function, mss_x and mss_y is the mean-square slope of the sea surface for the respected axis along, and across the wind direction, $b_{x,y}$ is the correlation coefficient between the slope components. This formula shows us an algebraic expression that connects the MSS components with the BRCS measurements.

The formula for the Mean Square Slope can be seen in equation 2.7.

$$mss_{x,y} = \iint_{\kappa < \kappa_*} \kappa_x \kappa_y \Psi(\vec{\kappa}) d^2 \kappa \quad (2.7)$$

This formula shows that the MSS components are determined by the wave-number integral from the ocean elevation spectrum $\Psi(\vec{\kappa}) \times \kappa_{x,y}^2$, also known as the slope spectral density.

By some assumptions, it is possible to simplify the equation 2.6. One can assume that $mss_y = mss_x = mss/2$ and $b_{x,y}^2 = 0$ and use $\sigma_0(\theta)$ in the specular direction where $\theta_1 = \theta_2 = \theta$ and $\phi = 0$, we then get equation 2.8.

$$\sigma_0(\theta) = \frac{|\mathfrak{R}(\theta)|^2}{mss} \quad (2.8)$$

This formula shows that the σ_0 values is inversely proportional to the mean square slope mss and is linearly influenced by the squared Fresnel reflection coefficient \mathfrak{R} .

2.2 Examples of GNSS-R Applications

This section briefly introduces some of the remote sensing applications of the GNSS-R technique.

2.2.1 Altimetry

One of the first suggested use cases for GNSS-Reflectometry was the determination of sea surface height and ocean altimetry. With this information, it would be possible to estimate the sea level variations, which could detect several mesoscale features in the oceans like tsunamis and eddies [40]. The results from an experiment using GNSS reflected signals for altimetry can be seen in figure 2.3.

This technique consists of using the delay measurements of signals to derive precise coordinates of the specular reflection on the geoid with a relative position to the receiver. By utilizing these measured vectors with accurate information about the orbit of the receiver, it is possible to calculate a rigid curved line as the receiver moves around its orbit, which in return can be converted to the height above the geoid or a given ellipsoid, given precise measurement of the receivers orbit [33].

When the path of the reflected signal has been estimated, the pseudorange ρ_R can be given in units of length, using equation 2.9 [40].

$$\rho_R(t) = \rho_{geo}(R(t), T(t - \frac{\rho_{geo}}{c}), S(R, T, h)) + \rho_{iono} + \rho_{trop} + \rho_{clock} + \rho_{inst} + \epsilon \quad (2.9)$$

The pseudorange has a geometric term, ρ_{geo} being the actual distance between the transmitter position T and the specular point S, and the distance between the specular point and the receiver position R. The location of the specular point S is a function using the receiver and transmitter position with the reflecting surface height from a known reference surface (being a geoid or Ellipsoid). There are also noise contributions to the pseudorange from both the ionosphere, troposphere, clock biases and instruments, and other extra noise caused by thermal and speckle.

The vertical component h is the unknown parameter desired by the altimetric application. The value for h is assumed based on the topography of the surface, giving the shortest reflection link between transmitter and receiver.

If the receiver is located at a low altitude and the Earth is locally flat, simplifications can be made, such as the range of the direct reflected signal can be calculated as in equation 2.10.

$$\Delta\rho = 2H \sin(E) \quad (2.10)$$

For this formula, H is the vertical distance between the surface and the receiver, and E is the elevation angle above the horizon.

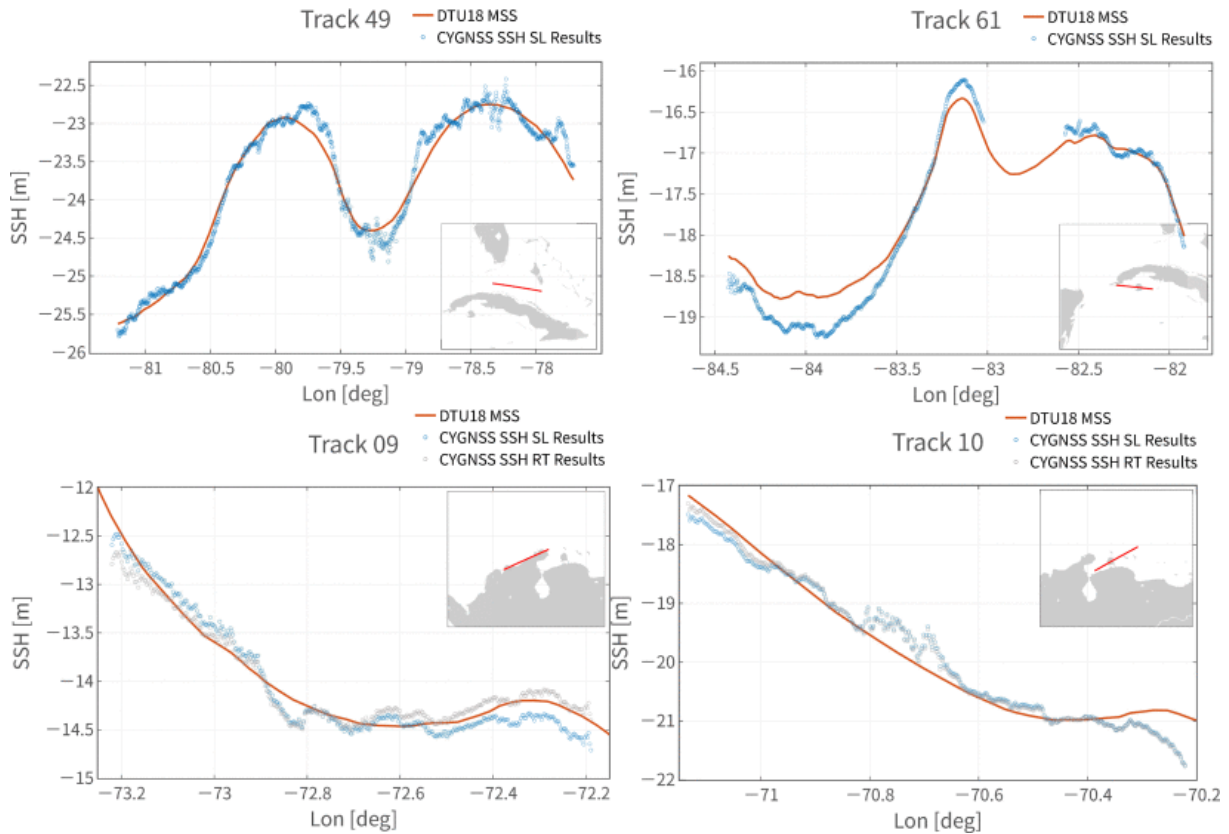


Figure 2.3: This figure shows 4 tracks of altimetric results using CYGNSS data shown as blue dots on the plots. The top plots shows two tracks using straight-line propagation corrections, while the bottom plots shows two tracks using straight-line propagation corrections together with bent propagation corrections. The left plots show data using GPS signals, while the right plots use data from Galileo signals. The retrievals, provided every 50 ms without any further smoothing or filtering, are compared to the DTU18 MSS height (orange line). Source: [7].

2.2.2 Wind Speed Estimations

Using GNSS-Reflectometry for scatterometry proposes was first proposed by Garrison, Katzberg and Hill in 1998 [17]. This technique takes advantage of the distortion effect on GNSS-R waveform originated from the roughness of a reflecting surface. By analysing this distortion effect, it is possible to estimate the ocean surface roughness, which can be modelled to estimate the sea surface winds.

The theory for the scatterometry application to estimate the ocean sea surface slope was explained in sections 2.1.1 to 2.1.3. However, the method for retrieving the wind speeds are a little more advanced. The CYGNSS handbook [43] summarises their basic steps for the wind speed retrieval algorithm as follows:

From DDMs of the BRCS and corresponding scattering areas, two DDM observables, the Delay Doppler map average (DDMA) and the Leading Edge Slope (LES), are derived. A population of the simulated samples are applied to a 13-day nature run of tropical cyclones and background wind fields, split into training and test subsets. An example of a simulated sample can be found in figure 2.4

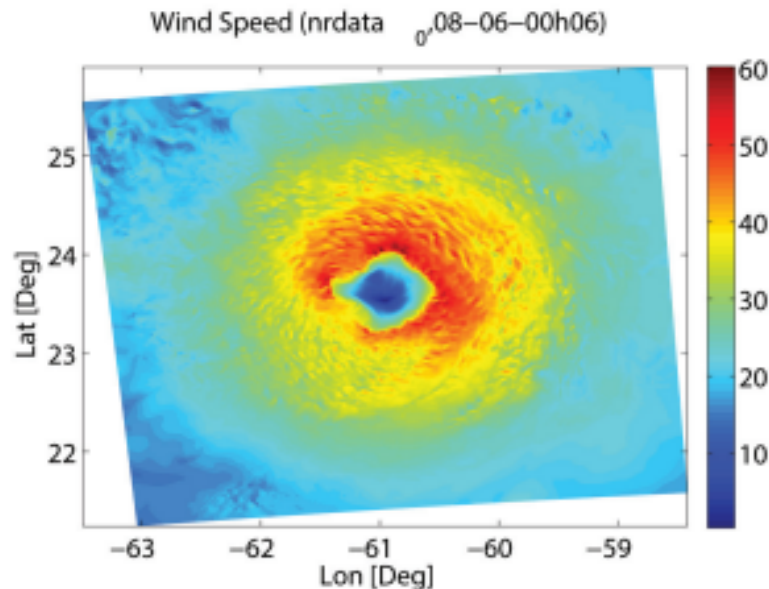


Figure 2.4: This image shows a snapshot of a simulated realistic tropical cyclone from the nature run model used to train the CYGNSS wind speed retrieval algorithm. Source: [43]

A statistical inversion algorithm is trained using the training data subset by constructing an empirical geophysical model function from measured and truth match-ups. Then debiasing is applied to wind retrievals produced by the DDMA and LES observable, and the test data subset is mapped to retrieve wind speeds using a minimum variance estimator.

Time averaging is applied to consecutive samples to produce a consistent 25 km spatial resolution data product, where appropriate, depending on the incidence angle of the sample. Samples with an effective field of view above the spatial resolution requirement are removed, and the performance of the algorithm is evaluated in terms of root mean square error between the true wind and the retrieved winds. An example of wind speed measurements under heavy precipitation are shown in figure 2.5.

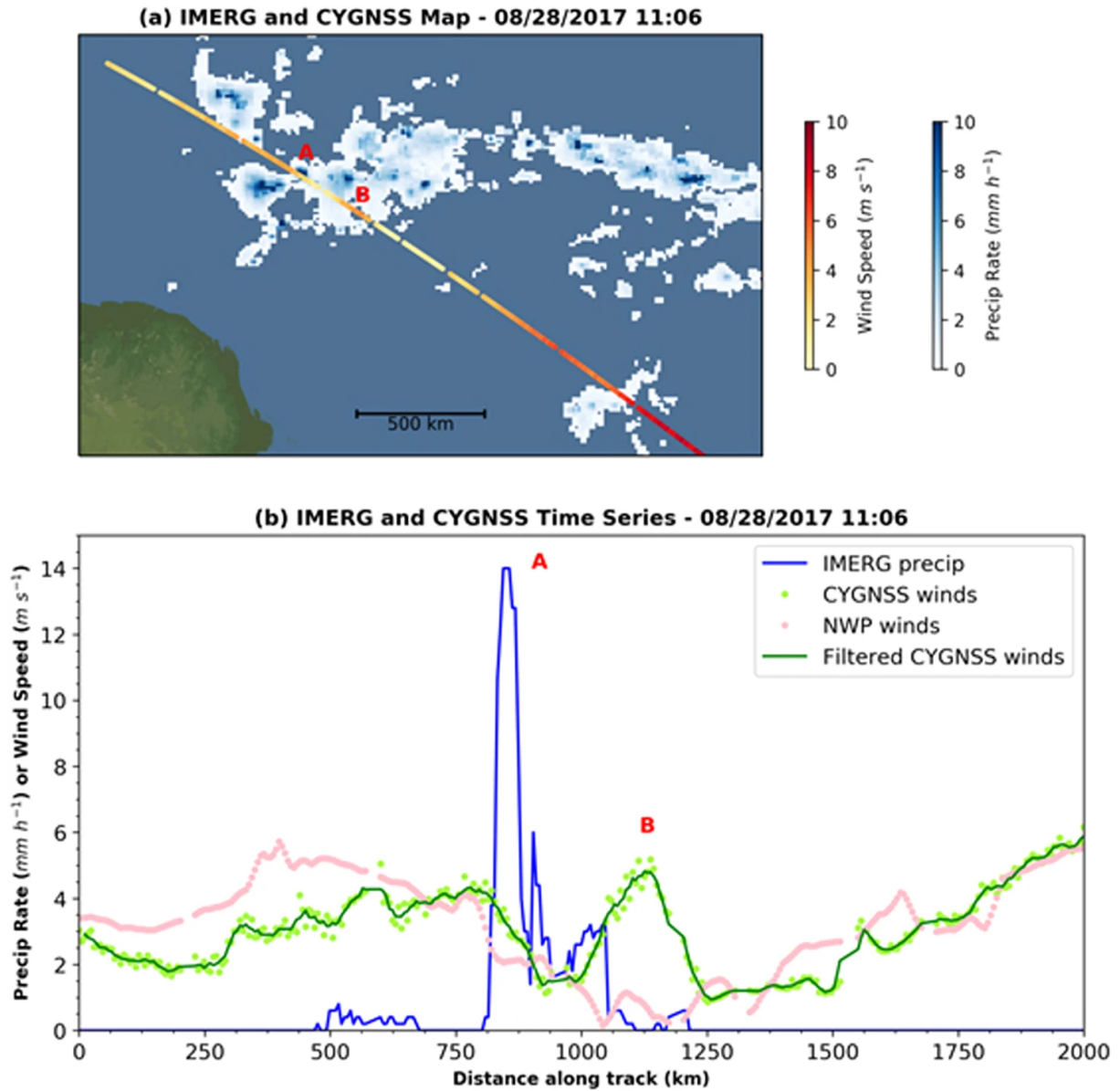


Figure 2.5: CYGNSS wind speed measurements across a strong convective storm on 28 August 2017. The Track is located off the northeast coast of Brazil. The top figure is a map view of CYGNSS along with Integrated Multi-satellite Retrievals for Global Precipitation Measurement (IMERG). Point A refers to a cell with heavy precipitation, while point B refers to an apparent gust front. The bottom figure shows a time series view, with A and B labels being the same as in figure (a). Source: [42]

2.2.3 Soil Moisture and Vegetation

The L-band frequencies of the GNSS systems are a few spectral bands where the atmosphere becomes transparent and vegetation becomes semitransparent, meaning that the microwave measurement will be heavily dependent on the soil moisture and roughness of the surface [40].

Some of the algorithms for retrieving soil moisture from GNSS-R data are based on the peak power or amplitude of the reflected waveform [27]. However, there have also been experiments trying to retrieve soil moisture by looking at power fluctuations of the signal generated by the interference of the direct signal from the GPS and the reflected signal over the soil surface [41]. A figure showing the results from this can be seen in 2.6.

Several experiments have shown that the reflected GPS signal is sensitive to soil moisture variations for areas up to 1000 m^2 horizontally and between 1 to 6 cm vertically, depending on the moisture. The GPS signal will penetrate deeper when the soil is dry compared to when it is wet [30]. It has also been proven that changes in vegetation affect the signal, but more future research on the topic is still needed [24].

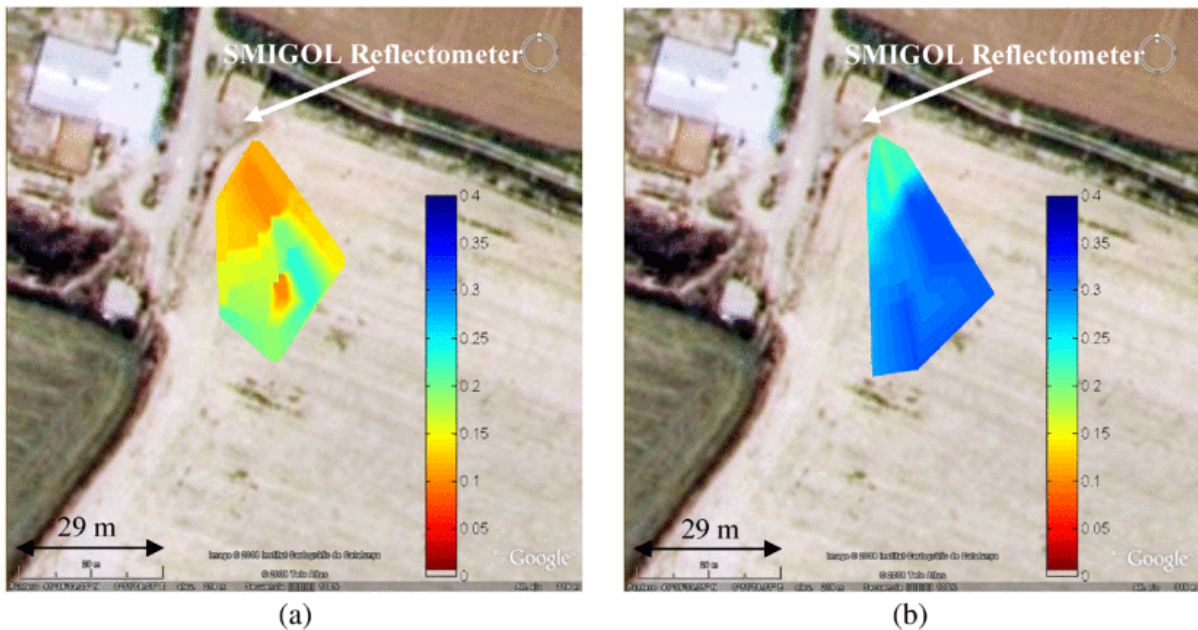


Figure 2.6: Soil moisture map for a bare soil scenario over a field in Spain. The map is modelled using the Soil Moisture Interference-pattern GNSS Observations at L-band Reflectometer (SMIGOL Reflectometer). The data was taken in (a) August and (b) September, after seasonal rains. Source: [41]

2.2.4 The Cryosphere

Cryosphere applications aim to derive information about areas of the Earth's surface where the water has frozen to a solid form. These applications include the detection and altimetric measurements of sea ice, glacial ice altimetry, and reflective surfaces' permittivity.

Monitoring the sea ice density is an essential observation for understanding the global climate changes and processes and practices for maritime operations like oil and gas extraction and optimising shipping routes.

GNSS-Reflectometry measurements show that observations over sea ice surface have a more limited spread in the DDM power distribution producing a strong peak. Sea ice produces a more coherent DDM than one from the open sea because of the scattering effect from the sea surface waves. This difference in distributions of scattering allows information on surface properties to be determined. Figure 2.7 shows the results from a sea ice detection experiment near both poles using GNSS-R data [10].

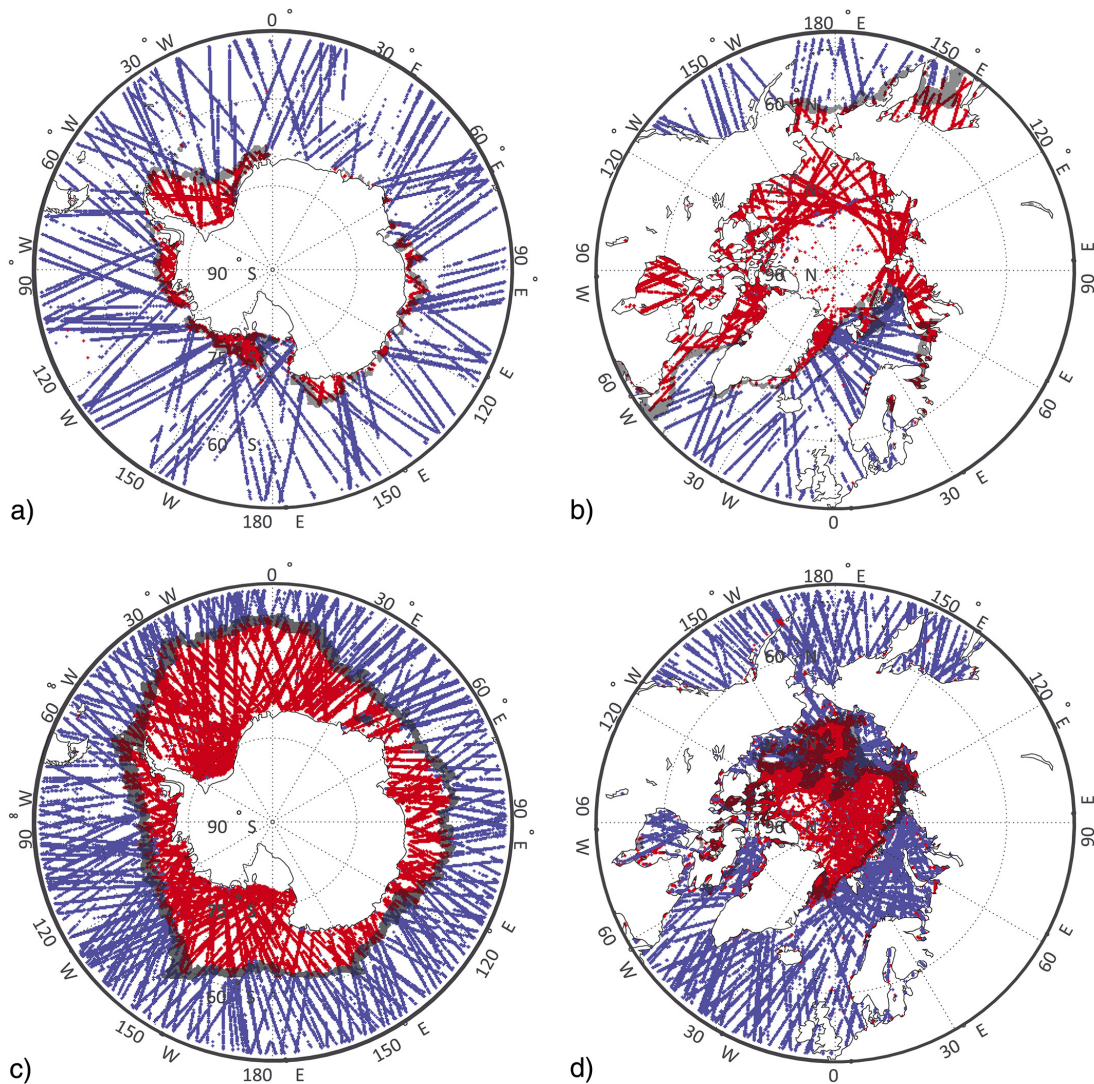


Figure 2.7: GNSS-R surface characterization over Antarctic (a and c) and the Arctic (b and d). The red colour indicates sea ice, and blue indicates open water. The images represent the maximum and minimum observations over a year. Source: [10]

2.2.5 The Detection of Microplastics

The idea of using GNSS-reflectometry to detect microplastics in the ocean is still a very new and unexplored field of research. However, a very recent paper by Evans and Ruf [16] present a method using spaceborne GNSS reflectometry radar measurements of the ocean surface roughness. The study relies on a reduction in responsiveness to wind-driven roughening assumed to be caused by surfactants acting like tracers for microplastics near the ocean surface.

Their algorithm focuses on comparing a modelled version of mean square slope (MSS) using estimated wind speed data to calculate an expected value of the MSS against the observed MSS from the CYGNSS dataset. By finding anomalies between the two sets of MSS values, they expect to find concentrations of ocean microplastics tracers. They assume there is a suppressing effect on the rough ocean surface due to the presence of surfactants. The surfactants are assumed to cause wave damping. An example of the results from this paper is shown in figure 2.8

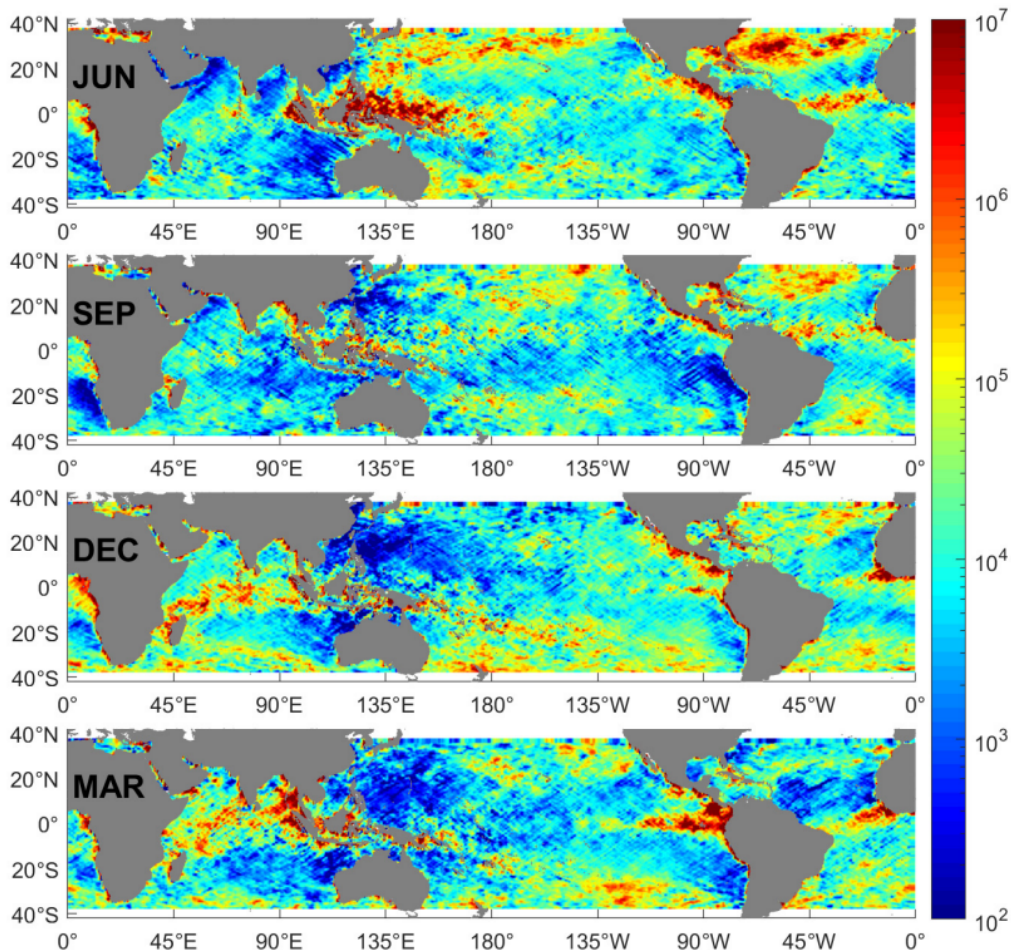


Figure 2.8: Monthly average microplastic number density concentration ($\#/km^2$, log10 scale) for June–September–December 2017 and March 2018. Source: [16]

The next chapter will discuss the issue of oceanic microplastics and reviews some of the available remote sensing data and methods as well as developed models for monitoring the distribution of microplastics.

Chapter 3

The Issue of Microplastics In the Ocean

This chapter will introduce one of today's major issues regarding ocean research, namely microplastics. The origins and consequences of microplastic pollution in the ocean will firstly be presented, followed by a brief overview of well known remote sensing applications for the detection of the marine debris.

The problem of plastic littering in the oceans has been an issue reported on since the early 1970s [9]. In the beginning, the scientific community showed very little interest in the topic, but eventually, as more data became available and the ecological impact of the debris became exceedingly apparent, it quickly gained traction. The majority of the research reports looked into the biological impact of plastics on animals, with focuses on themes such as entanglement [29] and ingestion [39].

In recent years, however, there have been many reports of an unusual occurrence of plastic debris in the North Pacific gyre, also known as the Great Pacific Garbage patch, stretching from Japan to the western coast of the USA. Plastic debris that ends up in the ocean will follow the oceanic currents and winds and eventually accumulate in various regions to form garbage patches [35]. This phenomenon has become a high-priority research area within the Marine Biology community.

However, it is not only the large, easily observable pieces of plastic floating around in the water that create problems. There are also small pieces of plastic that are invisible to the naked eye, namely microplastics. The general agreement for the definition of microplastics is smaller fragments of plastic having a length of fewer than five millimetres [36].

The plastic that ends up in the ocean stays there for so long due to its longevity in the marine environment. Plastic degrades very slowly, mainly as a result of exposure to UV radiation or mechanical abrasion over a long period of time. In addition to this, plastic also has high buoyancy allowing it to float long distances from its original starting point. [44]

3.1 The Origins of Microplastics

Over the last 50 years, the production of plastics has steadily increased and has since the year 2014 exceeded 300 million tonnes produced per year [19]. The significant increase in demand and production has overwhelmed the recycling solutions for plastic waste, and most of it ends up in landfills. However, much of it also ends up in the oceans.

The sources of microplastics can be separated into two categories; primary sources being particles manufactured at the small size designed for a particular application, while secondary sources result from larger pieces breaking down. In addition to this, they can be characterized by origination from either land-based or sea-based sources. Land-based sources, including beach litter, contributes to about 80 % of the plastic debris found in oceans [1].

Several sources are contributing to the degradation and fragmentation processes of plastics in the marine environment. These are Bio-degradation of plastics caused by living organisms, usually microbes, photo-degradation caused by the UV radiation from the sunlight, thermooxidative degradation by an oxidative breakdown at moderate temperatures, thermal degradation at high temperatures, and hydrolysis being reaction with water. After degrading enough, the plastic will eventually fragment into smaller pieces, often due to mechanical abrasion over more extended periods.

However, in many cases, plastic degradation will be retarded while in the seawater because of the lower temperatures and lower oxygen concentration, compared to plastic out of water in direct contact with air. This raises the possibility that a lot of the microplastics are likely generated on beaches and are dragged out to sea. Figure 3.1 depicts one of many examples of beaches where plastic washes ashore [1].



Figure 3.1: Image showing the state of Kamilo Beach in Hawaii. It is estimated that between 15-20 tons of plastics wash ashore on this beach annually. Source: [32]

When plastic is manufactured, an essential part of the process is the compounding and processing of resin pellets into valuable products. Even though plastic manufacturers have many rules and regulations on the observation and procedures regarding the loss of pellets, they have been found in freshwater, and marine habitats in locations close to polymer plants [26]. In addition, microplastics have also been found in waters after running through industrial wastewater plants [4].

Microplastics also come from other sectors than just production. In the agriculture section, plastics are used for irrigation and used as mulch, sitting on the field for many months in the sun. When they are finally disturbed or watered, they break down into microplastics and be transported via runoff to marine environments. Another land-based source is the potential discharge concerning construction in either the building, service or demolition phase of a structure. Plastic plays a significant part in modern construction, be it for packaging items or used as insulation.

Land transportation also indicates having an impact on microplastic pollution. The emission of rubber dust originating from car tire wear might be a significant source of microplastic pollution in the seas. The dust particles are either transported by air or washed from the roads to surface waters or drains [49]. The tourist industry can also play a part in microplastic pollution. Many popular tourist destinations are coastal, and a high tourist activity can be attributed to higher plastic usage. [37]

When it comes to Sea-based sources, a major microplastic pollutant is the fishing industry. Fishing gear can be lost at sea by accident, by sheer abandonment or by deliberate disposal. Around 18 % of the marine plastic debris found in the ocean environment is attributed to the fishing industry [1]. However, this plastic pollution from displacements also apply to the aquaculture industry.

Industries by themselves are, however, not the only source of microplastic pollution. The individual consummation of plastic products also has a huge impact. Around 40 % of the plastic production today is used for packaging [37], and a large number of this is used for packaging food and drink products. The convenience of storing food in plastics makes it a common source of litter, making its way to marine environments and being fragmented into microplastics.

Microplastics are also commonly found in cosmetic products, where it acts as abrasives agents and fillers in products such as facial scrubs, toothpaste and shower gels. These particles will be released into the wastewater systems or directly into aquatic environments [13]. Another significant potential source of microplastic pollution is the release of fibres from textiles when clothes are washed. Experiments have shown that a single piece of garment can produce up to 1900 fibres per wash, suggesting that a large number of microplastic fibres found in the marine environment might come from sewage from washing machines [6].

3.2 Consequences of Microplastics

The issue of microplastic pollution in marine environments is relatively a new phenomenon that still requires much research. The main concern of microplastics in the oceans today is their effects on the animals ingesting them. Studies have shown that over 220 different species have been found to ingest microplastic debris in nature [31].

Even though many will believe that microplastic ingestion is terrible, it might not be directly harmful. Fish and other large animals have frequently ingested materials that are indigestible and have evolved to adapt to this issue over millions of years. A more significant concern regarding microplastic ingestion is because it is not always just composed of plastic polymers but also additives like fibres, fillers, couple agents, colourants and more. These can make microplastics efficient in absorbing organic pollutants that can have a toxic effect, meaning that if swallowed, the microplastic brings along toxicants [25].

Another potential of ingestion microplastics is the issue of a physical blockage of the digestion system. This problem is more relevant for smaller creatures like plankton, which actively hunt for food and lead to starvation of certain plankton species. The consequence of this can be a massive shift in the Eco-system for more large creatures that rely on the plankton as a food source.

Microplastics will be eaten by both smaller creatures like plankton, as well as fish and become a part of the food chain, eventually leading up to humans as depicted in Figure 3.2. Traces of microplastics have been found in people from all over the world, and there are many indications that seafood is one of several significant sources of this [12]. The effect of microplastics on human health is, however still largely unknown and needs more research, but the potential for harm has been suggested [51].

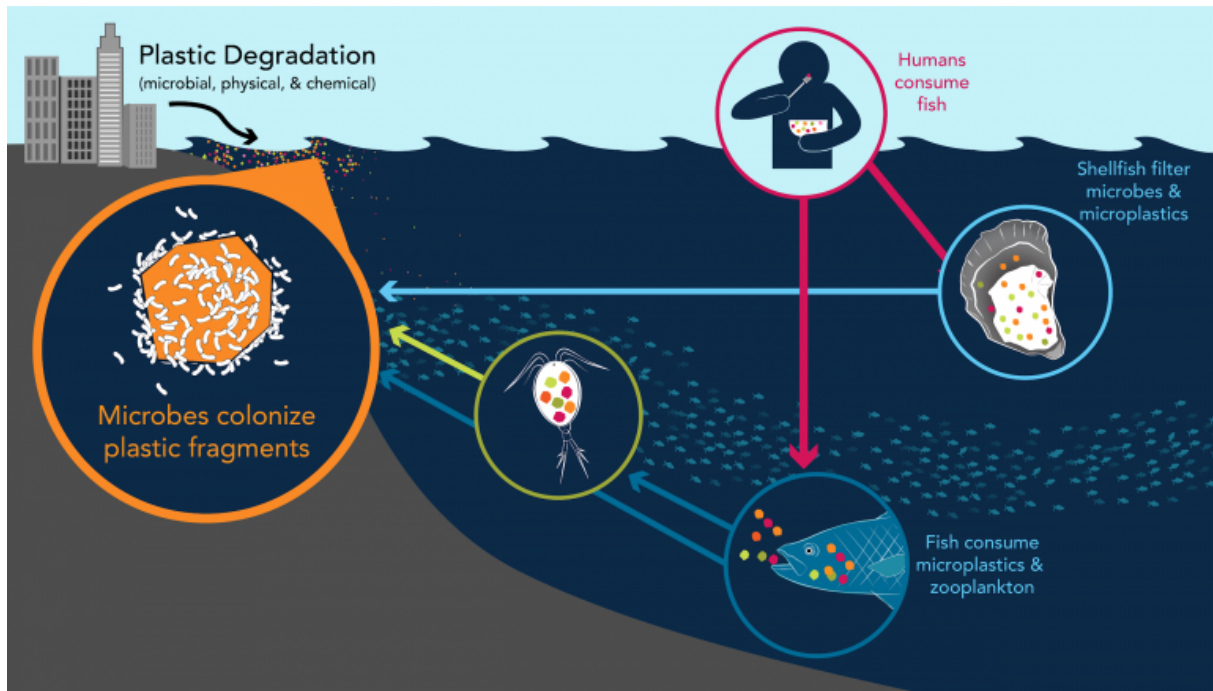


Figure 3.2: An info-graphic depicting how microplastics that end up in the oceans might end up as a part of the food chain. Source: [47].

3.3 Remote Sensing of Marine Debris

The application of marine debris detection, more specifically the detection of plastic pollution using remote sensing, is a new and emerging field of study and a significant technological challenge. Successful Remote sensing observations can act as a supplement for on-site observations and help to provide uniform coverage over larger areas and extended periods. In addition, quantifying the concentration and source of debris entering the marine environment over time can provide critical information on how to formulate and evaluate responses to reduce debris in the oceans.

Having a good knowledge of the marine debris global coverage is very important, as some pollutants like plastics can travel long distances and accumulate over time. By using remote sensing satellites, it is possible to survey areas where direct observations are difficult to gather, in addition to the possibility of providing high sample rates of observations. There are, however, considerable diversities in the chemistry and geometry of debris, and no sensors can directly observe all kinds of marine debris. Maximenko et al. [34] present several methods of remote sensing that has proven to detect marine debris.

High spatial resolution imaging has been used to monitor marine debris washed ashore, floating on the ocean surface and slightly submerged. This method uses high-resolution cameras to capture authentic colour RGB composite images on the visual spectrum (400-700 nm). These images provide complementary information about the marine debris's colour and shape used to separate manufactured objects from marine organisms. However, the RGB images do not provide information about the geometric or chemical composition of the debris.

This technique is not only good for detecting flotsam but can also be used to identify the particular type of debris or object. The analysis of visible images requires advanced interpretation techniques to eliminate environmental disturbances from the ocean like breaking waves, white caps, seafoam, and reflected glint in addition to clouds and cloud shadows.

The optical spectro-radiometric technique aims to detect and characterise plastics and other types of marine debris by analysing the spectral absorption features of plastics and other debris from ultraviolet to far-infrared spectrum. These absorption features are shown to be insensitive to the object's size and colour, or for plastics, the type of polymer, suggesting that these features can potentially apply to remote detection of ocean plastics.

The infrared spectrum has identified a higher reflectance signal from the spectral signature of plastics than the dark, nearly flat reflectance of oceans, enabling the possibility of detecting the reflectance of floating ocean plastics. This will, however, depend on the sensor's capability to detect the plastics as even slightly submerged objects can be masked by the waters ability to absorb the light.

Then we have the technique that uses radars, which are active sensors transmitting an electromagnetic pulse that measures scattered signals caused by hitting certain surfaces, such as the ocean surface. Radar sensors are often used to measure essential oceanic variables such as sea-surface topography, wind speed and direction, waves, whitecaps, and sea ice coverage. For the detection of marine debris, one up-and-coming radar technology is the synthetic aperture radar (SAR), exploiting the forward movement of the platform to synthesise a large aperture to increase the spatial resolution, possibly to a sub-meter resolution depending on the scene and sensor. Figure 3.3 shows an example of a high-resolution SAR image showing several oceanic features.

By various techniques and capabilities, it is possible to exploit interferometry, frequency and polarisation diversity to measure not only the reflected signal from marine debris but also to profile above the ocean surface to determine the wake generated by its interaction with the waves and the velocity of the drift relative to the surrounding area.

Other types of radars presently used in satellite missions, like altimeters and scatterometers, provide data that can be used for the derivation of mesoscale surface currents playing a vital role in the transport of marine debris or other types of pollution like oil spills, as well as biological rafting and climate systems.

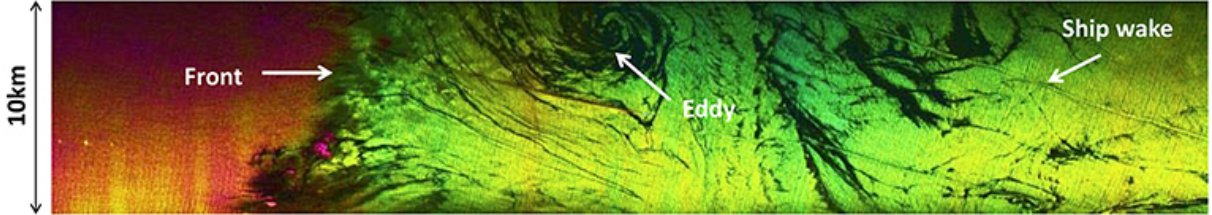


Figure 3.3: Example of a High-resolution sea surface map off Santa Barbara, California, derived from suborbital C-band SAR. Source: [34]

Chapter 4

Data-set Description

This chapter will present the datasets used in this thesis for the study of ocean microplastics. The main dataset is the data product from the NASA CYGNSS mission which is primarily aimed at improving hurricane forecasting. The ancillary dataset is from an hourly estimation of atmospheric variables provided by the European Centre for Medium-Range Weather Forecasts (ECMWF), namely ERA5. The machup dataset for verification is widely accepted models of global microplastics which provide the count and concentration mass of the ocean debris.

4.1 Cyclone Global Navigation Satellite System

NASA launched the Cyclone Global Navigation Satellite System (CYGNSS) in 2016 as a part of the pathfinder mission. This satellite constellation consists of eight micro-satellites, each outfitted with a GNSS-Reflectometry Doppler Delay Mapping Instrument (DDMI) capable of tracking four simultaneous reflections [38].

The main scientific objective of the CYGNSS mission is to collect space-based measurements over the wind speeds on the ocean surface at the inner core of tropical cyclones. The data from this mission is used to study the relationship between surface properties, atmospheric moisture thermodynamics, heat transfers, and the dynamics at the inner core of a tropical cyclone to get better knowledge on how tropical cyclones form and strengthen over time [38].

The CYGNSS satellites operate in a near-circular, non-synchronous orbit at approximately 510 kilometres above the earth, at an inclination of 35° from the equator, making it possible for the satellites to provide measurements over the ocean surface at the critical latitude band for the formation and movement of tropical cyclones between 38° North and 38° South. Figure 4.1 shows the coverage of the CYGNSS satellites, showing that we have almost full coverage within the latitude band over 24 hours [43].

The product of the CYGNSS mission are four levels of data products, produced in the form of NetCDF (Network Common Data Form) files made publicly available through the NASA Physical Oceanography Data Active Archive Center (PO.DAAC).

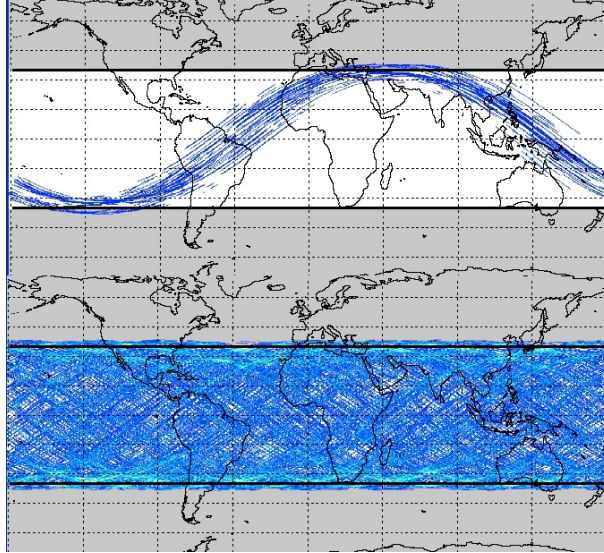


Figure 4.1: The spatial coverage of the CYGNSS satellite tracks after 90 minutes (top) and 24 hours (bottom). Source: [5]

The NetCDF is an interface for array-oriented data access to create, access, and share scientific data. This very scale-able format supports a good variety of popular programming languages and is very efficient for accessing specific parts of the dataset [48].

The level 1 data includes the Delay Doppler Maps (DDMs) of the bistatic radar cross-section (BRCS). Two calibrations are producing the level 1 data. Firstly the level 1A calibration aims to convert the individual raw bins of level 0 DDMs from processed counts into DDMs of received power P_g in units of watts, like presented in equation 2.1. Secondly, the level 1A DDMs are converted into level 1B DDMs of BRCS by unwrapping the forward scattering model, which generates two data products; a DDM of unnormalized BRCS values σ and a DDM of effective scattering area, both being in the unit m^2 . By dividing the unnormalized BRCS values by the effective scattering area, the normalized bistatic radar cross-section (NBRCS) is produced. A NetCDF file is produced per CYGNSS satellite per date.

The level 2 data provides both the mean square slope (MSS) and surface wind speed of the ocean surface. The MSS is crucial for understanding the air-sea processes and interpreting altimetry and scatterometer radar back-scatter measurements. There is also a direct connection between the BRCS measurements and the MSS, making both variables important for examining features on the ocean surface.

The primary mission for the CYGNSS project is the determination of ocean surface winds by fitting calibrated DDM peak power data to empirical or modelled geophysical functions. These winds are obtained from two observables; the DDM average (DDMA) and the leading edge slope (LES) as presented in section 2.2.2. The level 2 CYGNSS dataset is presented in a single NetCDF file for all the eight satellites per day.

The level 3 data is the gridded surface wind speeds, averages in space and time on a 0.2° latitude, longitude grid. Each level 3 wind file covers a one-hour period of the CYGNSS constellation and is presented in a single netCDF file per date. The level 4 data is a data assimilation product showing the surface wind vector analysis field on a basin-wide domain of a 9 km grid. This level of data is not currently available on the PO.DAAC website.

4.2 ECMWF Reanalysis v5 (ERA5)

The main factor that affects the roughness of the sea surface is wind speed. Therefore, it is important to consider the role of the wind speed in the analysis.

To do this, we use the ERA5 dataset to find the wind speed at any reflection point given location and time. This is the fifth generation of datasets provided by the European Centre for Medium-Range Weather Forecasts (ECMWF) [15]. This dataset provides an hourly estimate of many atmospheric, ocean-wave and land-surface variables; all provided on a Latitude-Longitude grid of 0.25 degrees.

The dataset used a method called data assimilation, inspired by numerical weather prediction centres, where every 12 hours, a previous forecast is combined with newly gathered observations to provide the best possible estimates for the state of the atmosphere, which they call analysis. Reanalysis works similarly but has a reduced resolution that allows for provisioning of the data spanning several decades. Not having the constraint of providing timely forecasts, it can span back long treks of time and improve on the original observations, benefiting the quality of the reanalysis product.

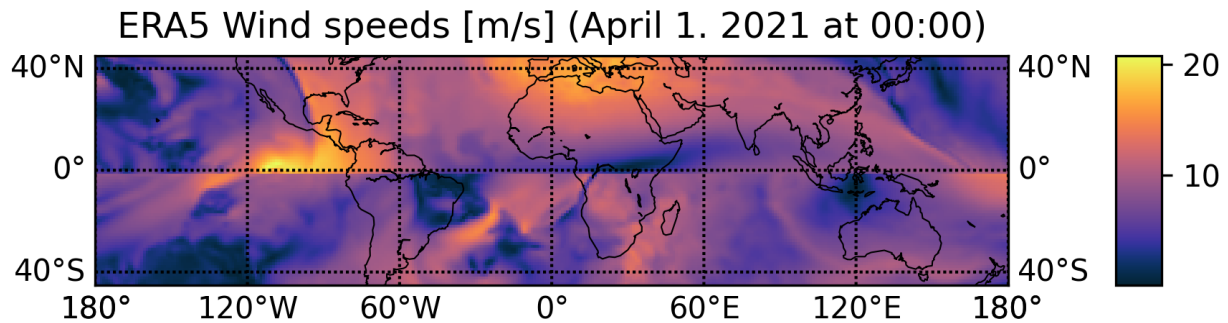


Figure 4.2: Example of the ERA5 processed wind data showing (near) global coverage of wind speeds [m/s] at a specified time and date.

The variables of interest collected for this project is the "10m v-component of wind" and "10m u-component of wind" provided in meters per second. These variables will together provide an estimation of the wind speeds, 10 meters above the sea surface. We can use this data to give a rough estimation of the wind speed above each peak detected. Figure 4.2 shows an example of wind speeds at midnight, first of April 2021.

When downloading the dataset, we separated it by one file per month, in the NetCDF format. After selecting the aforementioned two variables, we selected the corresponding year and all available days and time slots for the given month. Since the CYGNSS only operates over tropical regions and mid-latitudes, we selected the region with the latitude between 45° and -45° and longitude between -180° West to 180° East. Each monthly file has roughly the size of 1.5 GB.

4.3 Global Estimation Models of Microplastics

This study aims to monitor the distribution of microplastics in the ocean using GNSS-Reflectometry. For the verification purpose, we need some known and acknowledged estimations of the concentrations of microplastics that we can compare with our results. For this purpose, we looked at three global distribution models of microplastics concentration described by van Sebille et al. in [45].

The focus of the latter study was to assess the amount and distribution of small plastic debris on the ocean surface. In order to do that, they collected every available dataset on small floating plastic debris collected using surface-trawling plankton nets, ending up with over 11000 observations over a multi-decadal period. Plankton surface-trawl datasets are generated by special nets outfitted on boats, with a mesh ranging from 0.1 to 0.5 mm, capturing particles bigger than the size of the net aperture.

After collecting datasets, the data was standardized by removing variability associated with factors that could affect the concentration or representation of the sample like sample year, wind speed, geographic location and tow distance. The location and standardized version of the collected data can be seen in figure 4.3.

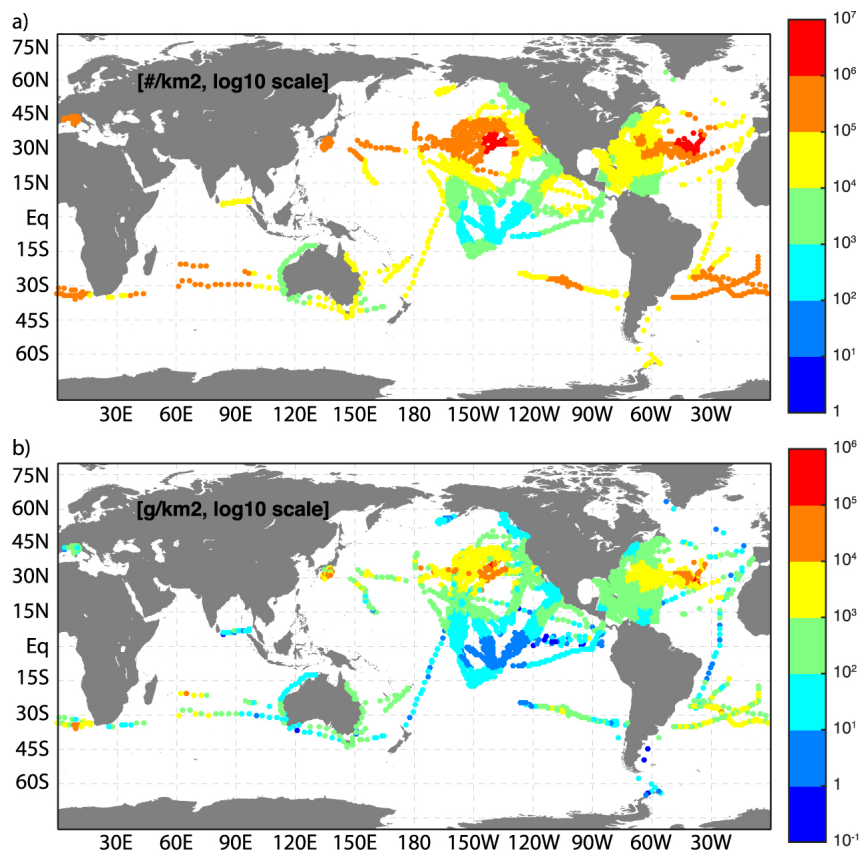


Figure 4.3: Plots showing the location and standardization of top plot a) the microplastic count and bottom plot b) the microplastic mass from all the collected surface trawl data, presented in the log 10 scale. Source: [45]

The non-uniformly distributed, standardized plastic concentrations are then spatially interpolated to estimate a global view of the microplastic distribution, being essential to indicate the microplastics concentration for areas with low coverage.

In order to get a more realistic prediction of the microplastic concentration, three independent ocean circulation models, Maximenko, Lebreton and van Sebille, are synthesized with the observations. Virtual microplastic was released within the ocean circulation models to obtain a map of likely distributions from ocean surface current transport. The regression predicted from the model's distribution depends on the assumptions of the ocean circulation models, like how currents are derived, how plastics are released or removed from the ocean.

The Maximenko model assumes that the plastic source is uniformly distributed throughout the global ocean. The model uses a transition matrix approach based on the probability of particle travel calculated from the trajectories of known satellite-tracked buoys from the NOAA Global Drifter Program. Unique to this model is using a plastic sink, meaning that the model also assumes that plastic can be washed ashore and enter the shoreline, meaning that they exit the system. The data was generated over a 10-year model run. The Maximenko models for microplastic distribution can be seen in figure 4.4.

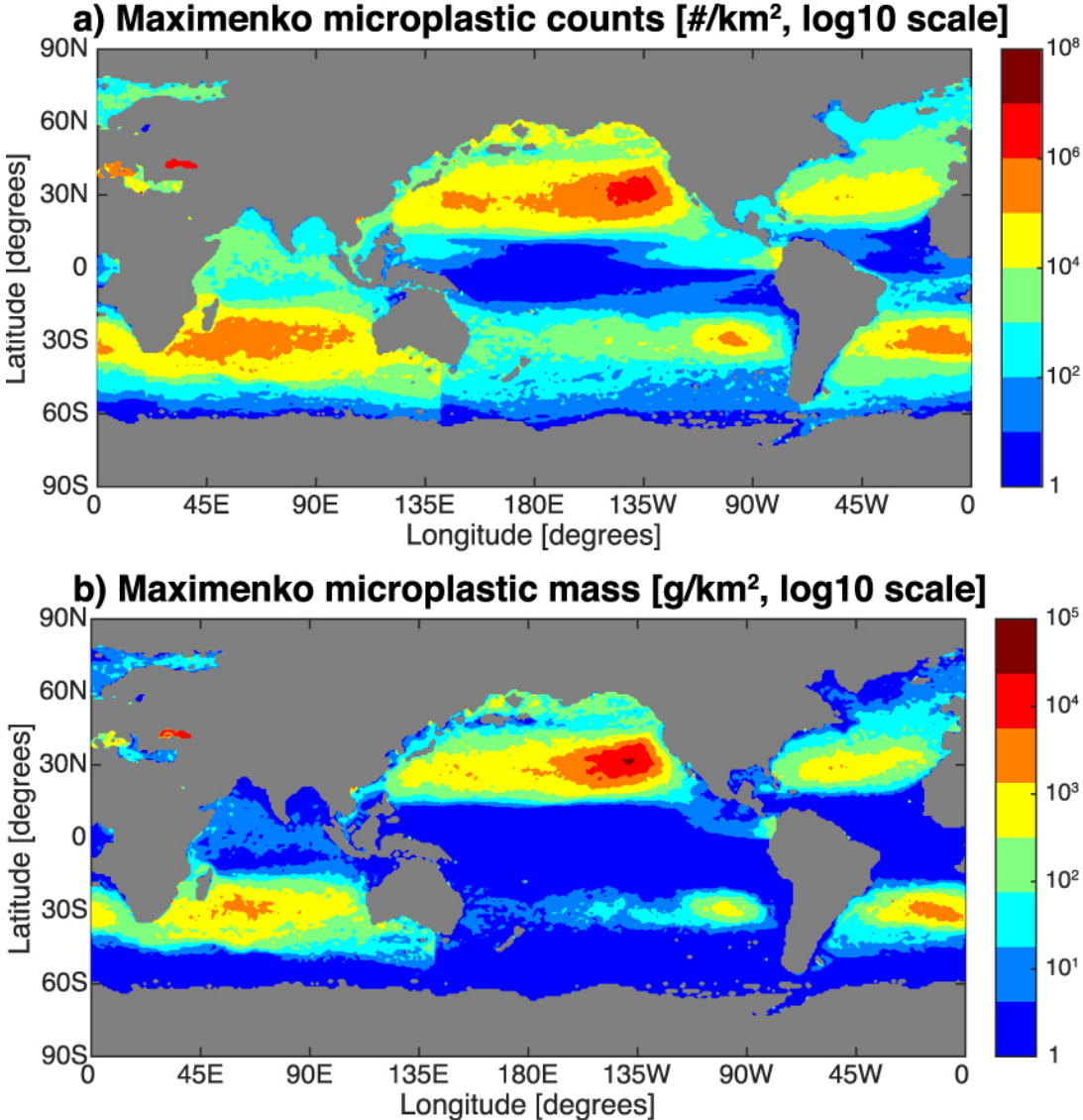


Figure 4.4: Maps depicting the Maximenko model for distribution of microplastics counts (top) and mass (bottom). Source [45]

The Lebreton model uses ocean velocity fields and assumes that plastics originate from major river mouths as a function of urban development, coastlines as a function of the coastal population, and major shipping routes as a function of shipping traffic. Microplastics are also assumed to be released continuously in increasing amounts based on global plastic production data. Therefore, this model does not use any plastic sinks. The data was generated over a 30-year model run. The Lebreton models for microplastic distribution can be seen in figure 4.5.

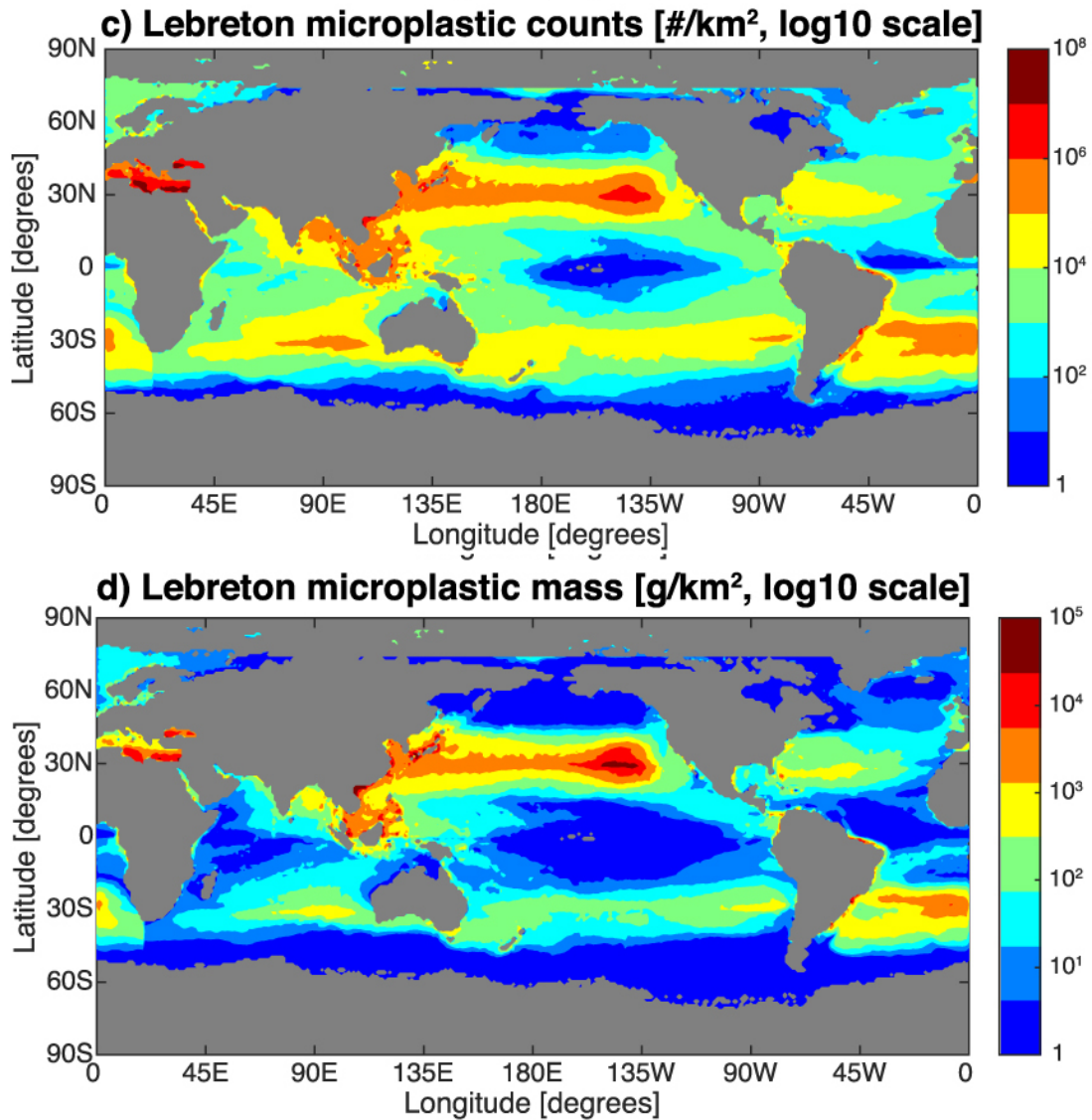


Figure 4.5: Maps depicting the Lebreton model for distribution of microplastics counts (top) and mass (bottom). Source [45]

The van Sebille model also assumes the distribution of plastics travel based on the trajectories of the drifting buoys, similar to the Maximenko model. In addition, this model assumes that the microplastic concentration is proportional to the human population within 200 km of the coast, scaled by plastic waste available to enter the country in 2010. This model does not use plastic sinks, and the data was generated over a 50-year model run. The van Sebille models for microplastic distribution can be seen in figure 4.6.

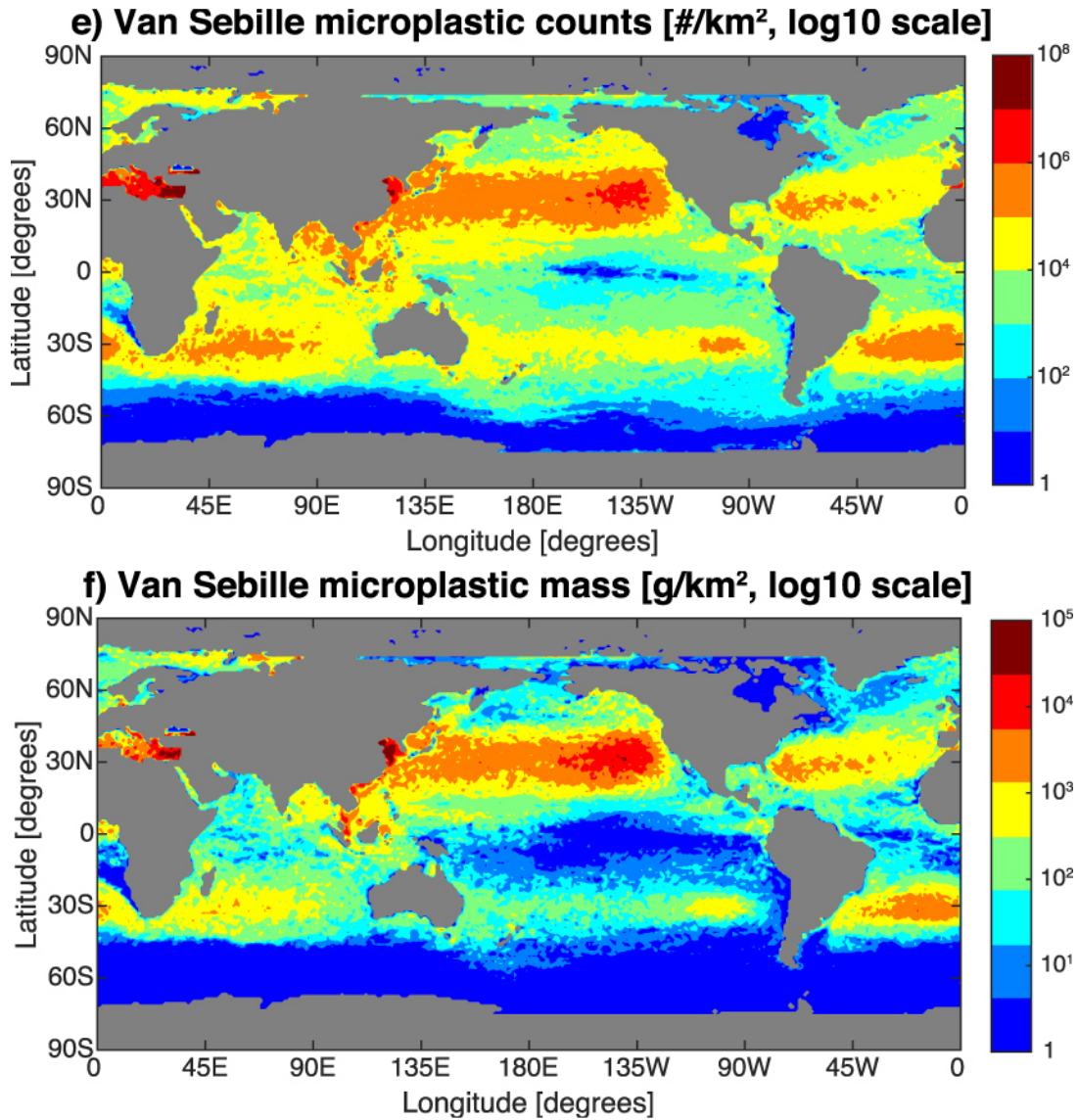


Figure 4.6: Maps depicting the van Sebille model for distribution of microplastics counts (top) and mass (bottom). Source [45]

The results from these models are global distributions of microplastic concentrations on a 1°x 1° spatial resolution. We will use these models as a benchmark to determine the quality of our results from detecting microplastics using the CYGNSS dataset. In the next chapter, we will present our implementation of the GNSS-R toolbox and the methods used to detect microplastics.

Chapter 5

Data handling & Methodology

This chapter will introduce the prototype GNSS-R Toolbox created to collect and process GNSS-Reflectometry data. Firstly, we present the web-based GNSS-R toolbox, how the CYGNSS data is collected and present the functionality and methods for the implemented tools. Then, we present our motivations and methods for the detection of microplastics in the ocean using spaceborne GNSS-R data.

5.1 A Web-based GNSS-Reflectometry Toolbox

This part of the project aims to deliver a basic toolbox where users can explore and interact with the CYGNSS dataset. These tools consist of: 1) a track demonstration tool where the user can select an area of interest, time and variables, which will be presented directly on the web page. 2) A data clipping tool for collecting specific variables within an area of interest. 3) An demonstration of ground-based GNSS-R data. Figure 5.1 shows a simple diagram of processes regarding the tools.

This project is developed using the Python programming language, more specifically **Python 3.8.6**. This programming language was chosen because it is relatively easy to work with and has a wide variety of modules known as packages that can easily be implemented and used.

A goal for the toolbox is to make the selection and processing of relevant GNSS-R data both efficient and straightforward. In order to make the project widely available while also having much flexibility in the design of the project and user interface, it was decided to make the toolbox into a web application. For this purpose, the Python web framework **Django** was selected because it is a framework that allows for the rapid development of secure and highly maintainable web applications.

To maintain good practices for developing the code for the project, the code hosting platform GitHub will be used. This platform allows for easy sharing and storage of the code and functions as a version control system, meaning that all the previous versions of the project can be accessed if necessary.

In order to give the user a good experience using the tools, several JavaScript packages have been imported and used for the implementation. For all the spatial data presented on maps, the JavaScript library **Leaflet** has been used. This library allows us to give the user an interactive experience whilst providing intuitive and efficient maps. The other data is plotted using the JavaScript library **Chart.js** allowing for the creation of efficient, flexible and interactive charts.

The following section will present how we collect the data from the CYGNSS dataset, followed by an introduction to the functionality and implementation of the tools.

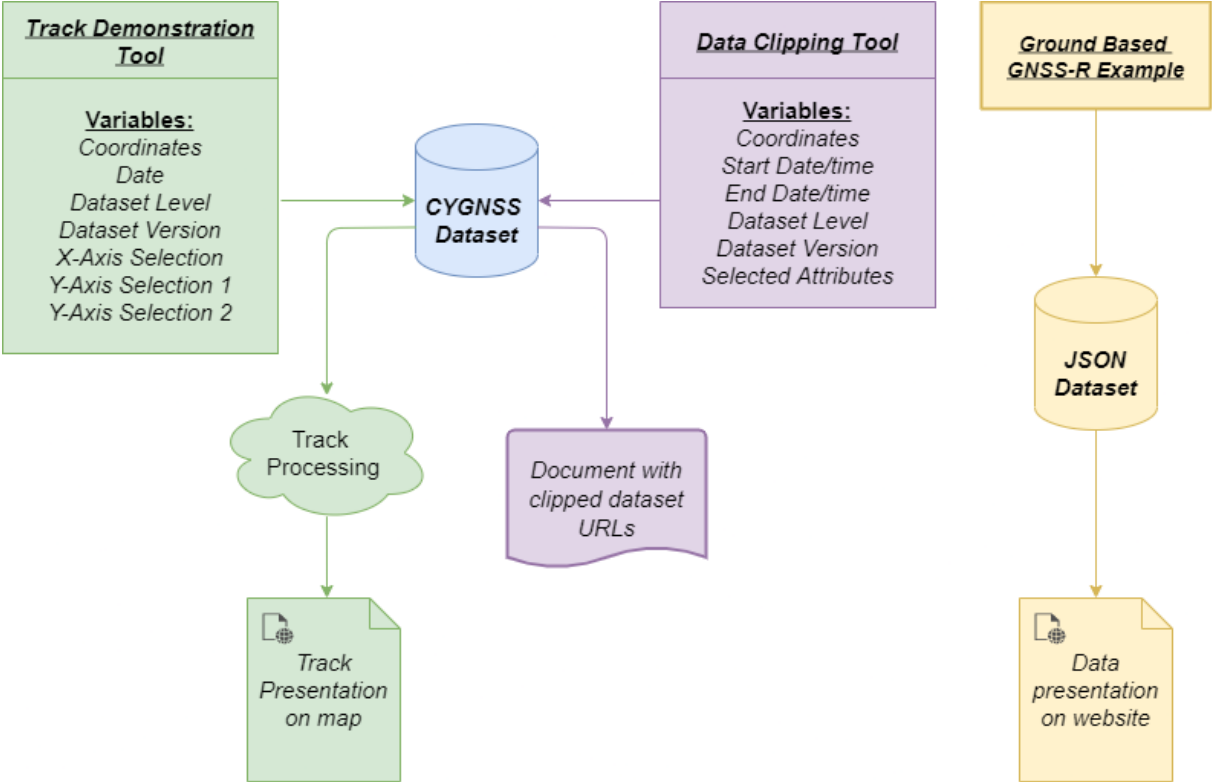


Figure 5.1: This figure shows a diagram explaining how the web tools interact with the datasets and users. For the Track Demonstration and Data Clipping tool, the user defines the variables, which then are sent to the CYGNSS dataset for filtering. The ground-based GNSS-R example takes its data directly from a JSON dataset and presents it to the user.

5.1.1 Data Collection

The CYGNSS dataset, as described in section 4.1 is a massive dataset that is continuously being updated. For this project, we are primarily interested in data from the level 1 CYGNSS calibrations. The level 1 data have a separate file for each satellite totalling up to eight datasets per date, each with 124 unique variables mostly being presented as an array of data taken every second or half-second or presented as a gridded dataset based on the Delay Doppler Mapping Instrument (DDM-I) that captured the data.

This means that even a single file from CYGNSS will consume both much time downloading and a lot of storage space if one were to directly download the files onto a local computer or server. Luckily for us, the CYGNSS data is made publicly available and is uploaded on a server making use of the data access framework OPeNDAP (Open-source Project for Network Data Access Protocol). This framework allows for an easy and quick way to obtain only specified data from a remote server.

In order to do this for our project, we used the Python library **Pydap**. This library allows one to remotely access a server dataset by providing a URL to the desired file. A pseudo-code snippet for our function to collect the level 1 tracklist data can be found in Code 5.1.

This function has the date, dataset level and dataset version (2.1 or 3.0) as its inputs. These are used to generate the specific URL for the dataset (line 6). In the case of level 1 datasets, we get eight URLs per date meaning we need to repeat the collection code for each of the eight satellite datasets. Each satellite also has four DDM instruments, each capturing its measurements, meaning that we also run the code for each DDM captured.

In line 9, we use the generated URL as input for the Pydap function `open_url(url)`, creating a variable called 'dataset', which will act as a pointer to the OPeNDAP dataset on the remote server. The data from the server is not accessed or collected until it is being called on. For example, the variable in line 12, `track_id` will download only the necessary data from the track identifiers for the current DDM within the dataset.

The `track_id` variable is used to separate the tracks (line 15) by checking the indices where the identifier of the track change. After that, we load all the other variables of interest from the dataset, like the coordinates, NBRCS values, timestamps, quality flags and others being specified should they needed.

Then for each unique track id, we add the variables to a single array appended on the overarching tracklist, meaning that we end up with a list of tracks on the format [Latitudes, Longitudes, NBRCS, Timestamp, Quality Flags, etc.]. The tracklist containing all the separated tracks is then returned from this function and can be used for processing.

Note that we do not download the data to the local computer by doing it this way. Instead, everything is collected directly from the remote server and is stored after being processed if warranted.

Code 5.1: Pseudo-code for the collection of level 1 CYGNSS tracks.

```
1 def collect_tracks(date, level, version):
2     # This function collects all CYGNSS tracks for given date, level and version.
3     track_list = []
4
5     # generate url to dataset from metadata
6     url = generate_url(date, level, version)
7
8     for satellite in range(8):
9         dataset = open_url(url[satellite])
10
11        for ddm in range(4):
12            track_id = dataset.track_id[:, ddm]
13
14            # Separates the track indices by the variable track_id
15            track_indices = where(np.diff(track_id) > 0), len(track_id))
16
17            sp_lat = dataset.sp_lat[:, ddm]
18            sp_lon = dataset.sp_lon[:, ddm]
19            nbrcs = dataset.ddm_nbrcs[:, ddm]
20            ddm_timestamp_utc = dataset['ddm_timestamp_utc'][:, ddm]
21            quality_flags = dataset['quality_flags'][:, ddm]
22
23            # Separate tracks using track_indices.
24            for track in range(len(track_indices)-1):
25                start = track_indices[track]+1
26                end = track_indices[track+1]
27
28                lats = sp_lat[start: end]
29                lons = sp_lon[start: end]
30                track_nbrcs = nbrcs[start: end]
31                track_ddm_timestamp_utc = ddm_timestamp_utc[start: end]
32                track_quality_flags = quality_flags[start: end]
33
34                track_list.append([lats, lons, track_nbrcs, ...
35                                track_ddm_timestamp_utc, track_quality_flags])
36
37    return track_list
```

5.1.2 Track Demonstration Tool

The Track demonstration tool aims to allow the user to explore the dataset without having to do any programming or download the dataset. This tool will present the user with a simple form to fill out the inputs for their query. An example of a filled-out form can be seen in figure 5.2.

In this form, the user selects the region of interest by using the square tool on the map and draw their bounding box or manually filling out the coordinates beneath the map. The user also selects the date for the observation, the level and version of the scientific data, what unit should be presented in the X-Axis, and two variables for the Y-axis.

After filling out the information in the form, all fields being valid, the user clicks on the submit button, and the application will run the data collection function. Depending on the region's size, this will take a couple of minutes, and after the processing is complete, the user will be presented with the data. An example of the presented map is shown in figure 5.3.

Selection Area:

Enter coordinates by using the square tool on the map or write them in the box: [lat,lon]

Top Left 22.89067,-153.27724 **Bottom Right** 18.11773,-161.36300

Database parameters:

Date: 01/04/2021

Dataset Level: L1

Dataset Version: v3.0

X-Axis Selection: Step

First Y-Axis selection: Normalized BRCS

Second Y-Axis selection: Leading edge slope

Submit

Figure 5.2: The user interface for the Track Demonstration Tool. In this window, the user selects an area of interest, as well as the date, dataset level and version. For the plotting of data, the user can also select the unit for the X-Axis and up to two Y-Axis variables.

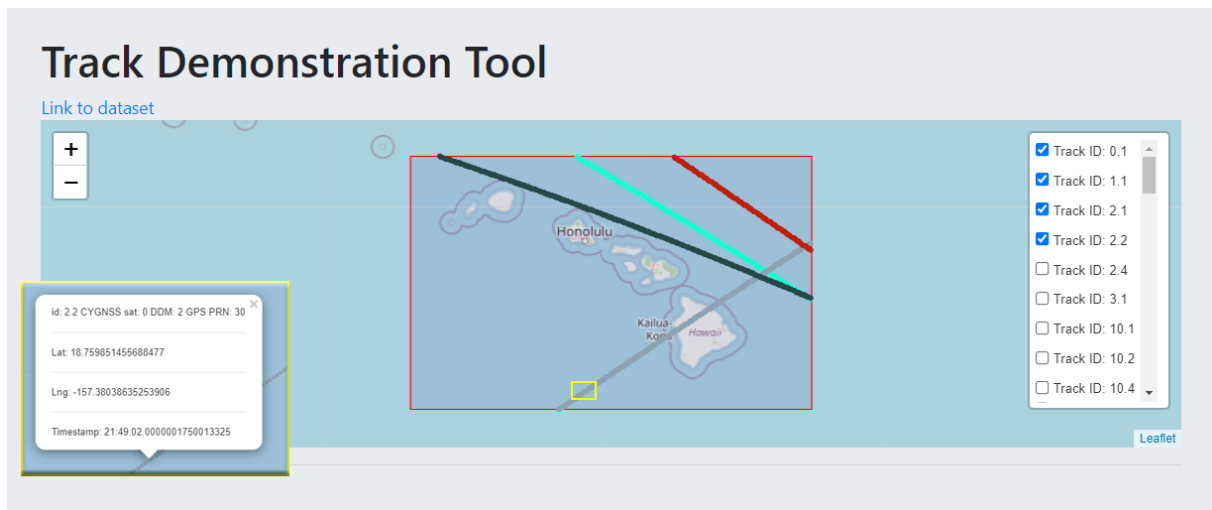


Figure 5.3: The track demonstration tool presentation of the tracks for the selected region and date of observation.

The processed data is presented to the user on an interactive web page. On the top of the page, there will be an interactive map with a red box indicating the selected region of interest. The user can zoom in and out on this map and use the mouse to navigate around. On the right side of the map, a menu with checkboxes will appear where a list containing track ID's is presented. This track ID consists of two numbers, the first number being the satellite number *10+ ddm, and the second number indicates a unique track within the same satellite and ddm. By clicking the checkbox for a track, it will appear on the map.

Above the map, there is also a link to the dataset should there be a need for the user to inspect the dataset further. For example, an information box will appear if a user clicks on a track point on the map, as shown within the yellow box on the figure. This information box will contain the metadata for the selected point, showing the track identifier, CYGNSS satellite number, DDM number and GPS PRN number in addition to the coordinates and timestamp.

Underneath the map, there will be a drop-down menu for each of the track identifiers. The associated plot with the variables selected for the X-, and Y-axis will be shown by selecting a track on this menu. An example of this is shown in figure 5.4. Here you can see the variables *ddm_nbrcs* and *ddm_les* for the selected track.

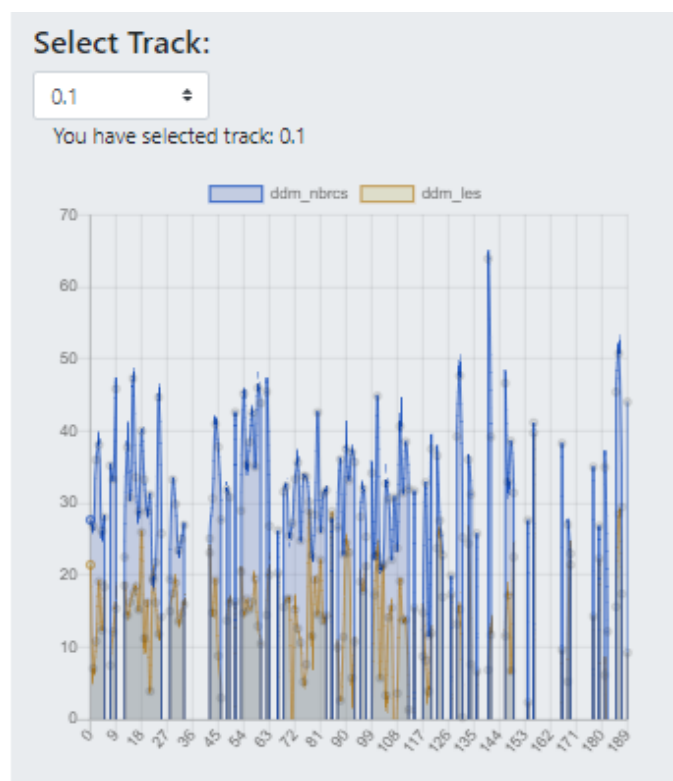


Figure 5.4: The selected variables from the user interface can be inspected for each track.

5.1.3 Data Clipping Tool

The Data Clipping tool aims to present the user with an interface for collecting only specific variables from the dataset within a selected region, enabling the data retrieval for users who do not have the capabilities to work directly with the extensive CYGNSS dataset or for users who are only interested in collecting data over specific regions. Like with the Track Demonstration tool, the user is presented with a form to fill out the required inputs. An example of a filled-out form can be seen in figure 5.5.

Data Clipping Tool

The second item in the applications' drop-down menu is used for Data Clipping and Filtering. In this item user can select multiple polygonal regions over the oceans or land and retrieve all the available data over the selected regions during the period of interest. Our web-based toolbox facilitates the data retrieval for those who don't have processing/downloading facilities to work with the CYGNSS's big dataset.

Selection Area:

Enter coordinates by using the square tool on the map or write them in the box:

Top Left: 30.726097,62.090395 Bottom Right: 21.875093,46.826793

Start date and time: 04/01/2021 00:00 **End date and time:** 04/03/2021 23:59

Dataset Level: L3 **Dataset Version:** v3.0

Select attributes:

- wind_speed
- wind_speed_uncertainty
- num_wind_speed_samples
- yslf_wind_speed
- yslf_wind_speed_uncertainty
- num_yslf_wind_speed_samples
- mean_square_slope
- mean_square_slope_uncertainty
- num_mss_samples

Submit

Figure 5.5: The user interface for the Data Clipping Tool. Here the user selects a boundary region, a period consisting of a start date-time and end date-time, the desired dataset level and version as well as the wanted attributes depending on the selected level.

In this form, the user selects the boundary region using the box tool on the map or manually filling in the coordinates. The user also selected the time frame for processing by filling out the start and end date and time. The level and version of the dataset are then selected. Depending on the dataset level selected, several attributes related to that dataset is displayed. Finally, the user checks all the attributes they want to collect and hits the submit button.

This tool does not download any data; it just generates the links for the datasets meaning that the processing should be reasonably quick. The user will then be presented with a file containing all the relevant URLs for the selected region and time frame. This file can then be used along with a provided python script in order to download and save the files to a local computer.

5.1.4 Ground-based GNSS-R

This part of the toolbox aims to present data from a ground-based GNSS-R station located at the Onsala Space Observatory in Sweden, operated by the German Research Center for Geo-sciences (GFZ). When the user loads the page for this tool, a JSON (JavaScript Object Notation) request is sent to a server that provides near real-time sea-level measurements calculated based on the ground-based GNSS-R experiment data. The JSON format is an open standard file format used to load data from a remote server. This format is much liked because of its simple syntax, efficiency, and flexibility to work with all programming languages, allowing for the option of collecting near real-time data by having the GNSS-R station update the JSON files as soon as the measurements are recorded.

The data presented for this application is divided into three parts; the GNSS-R sea surface products, the observations details and track inspection. The first part presents the sea surface level in the unit meters and sea surface roughness in the unit centimetres, with the X-axis representing the timestamp of the data capture. An example of this can be seen in figure 5.6. It is possible to hover above a point on the graph and get the specific data record on these plots. The span of the shown profile for both the sea surface roughness and sea level covers the last 24 hours.

GNSS-R Sea Surface Products

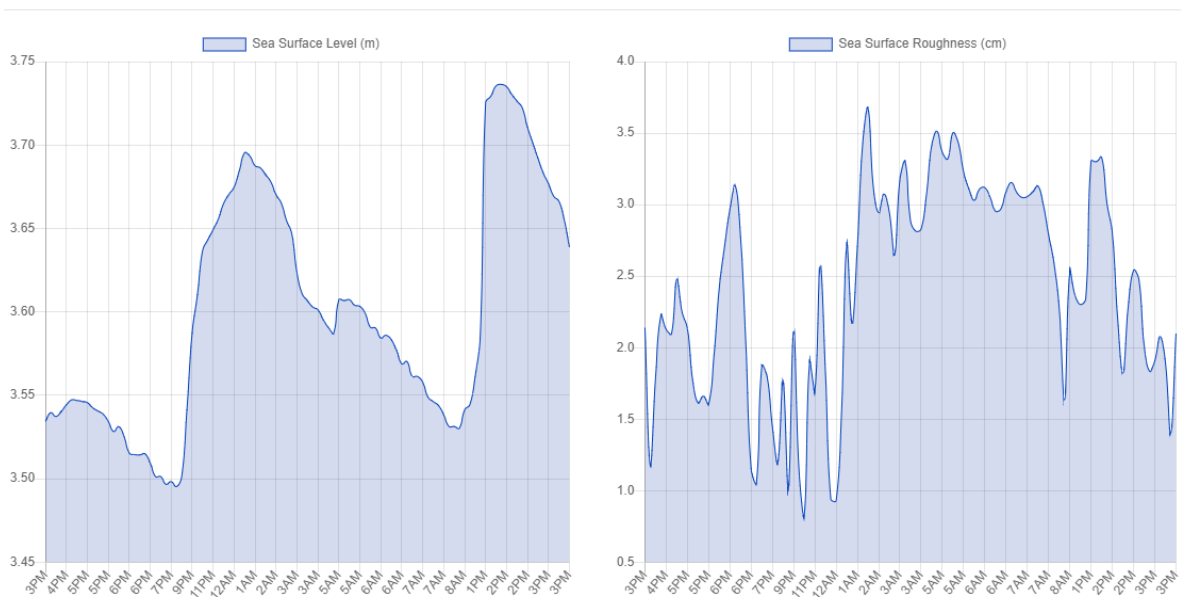


Figure 5.6: The sea surface product from observations at Onsala ground-based GNSS-R station. The left plot shows the sea surface level in meters, while the right plot shows the sea surface roughness in centimeters.

In the second part, the user can see the information about the satellite orbit and corresponding reflection points on the sea surface. These include a sky-plot and the coordinates shown on a map as depicted in figure 5.7, and a table of information about the elevation and azimuth angle range as shown in figure 5.8.

Observation Details

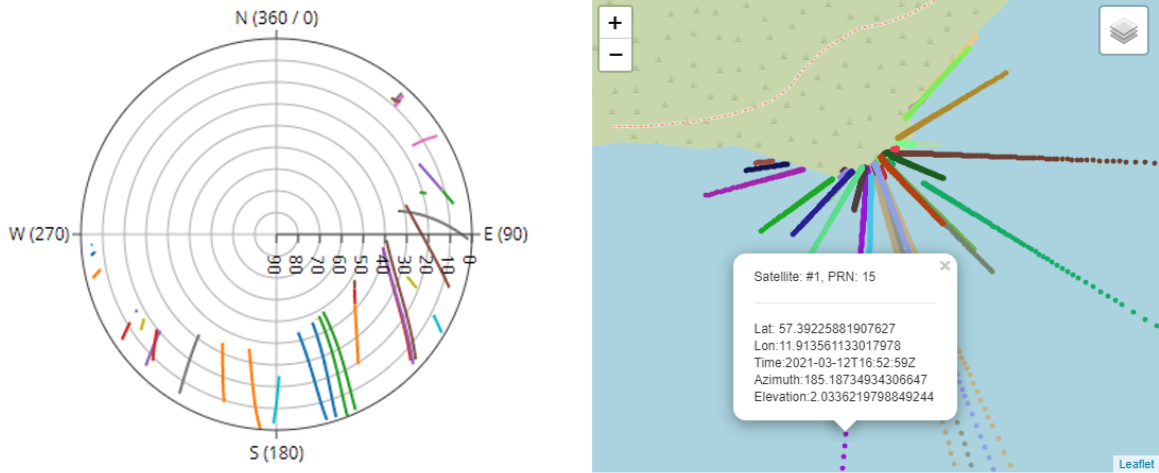


Figure 5.7: The observation details from the ground-based GNSS-R station data. The left plot shows a sky-plot for all the tracks while The right plot shows the track coordinates plotted on a map.

The sky-plot is made using a scatter-polar plot with the elevation angle as the radius and azimuth angle as the theta angle, with the top of the circle being the 0° angle pointing to the north. Each track is assigned a random colour, and by hovering over a point on a track, the point data for the radius, angle theta, GPS PRN number and id will be shown.

The coordinates for the tracks are presented in an interactive map. On the right side of the map, there is a menu with check-boxes for each track to show or hide them from the map. The map as presented has all the available tracks turned on, displayed as a scatter-plot with randomly assigned colours. It is possible to zoom in or out on the map, and by clicking on a point, metadata for the point is displayed in an appearing box. This box contains the satellite number and GPS PRN number of the tracks and the coordinates and angles of the point. Underneath the map and sky-box on the web page, a table containing the elevation angle range and azimuth angle range for all tracks are presented.

PRN	Elevation angle range		Azimuth angle range	
7	3.1°	24.8°	178.9°	180.9°
13	26.1°	46.2°	157.8°	159.5°
5	9.2°	34.3°	197.3°	206.5°
7	18.4°	21.2°	73.8°	74.7°
20	8.6°	19.8°	224.4°	231.6°
17	3.2°	40.6°	97.1°	133.5°
1	6.6°	8.1°	40.1°	43.2°

Figure 5.8: Table presenting the elevation angle range and azimuth angle range for the available tracks from the ground-based GNSS-R station.

The last set of data presented in the ground-based GNSS-R example takes a deeper look into the signals recorded by the receiver from each track. The user selects a track from the drop-down menu, and the observations are presented in two panels: the raw observations (top) and the interferometric fringe (bottom), as shown in figure 5.9. The Onsala station has three antennas with different polarization designs and orientations. The antennas include one up-looking antenna with RHCP and two sea-looking antennas with RHCP and LHCP designs. The data for each of the antennas are presented in separate columns.

Select Track:

#1, PRN: 15

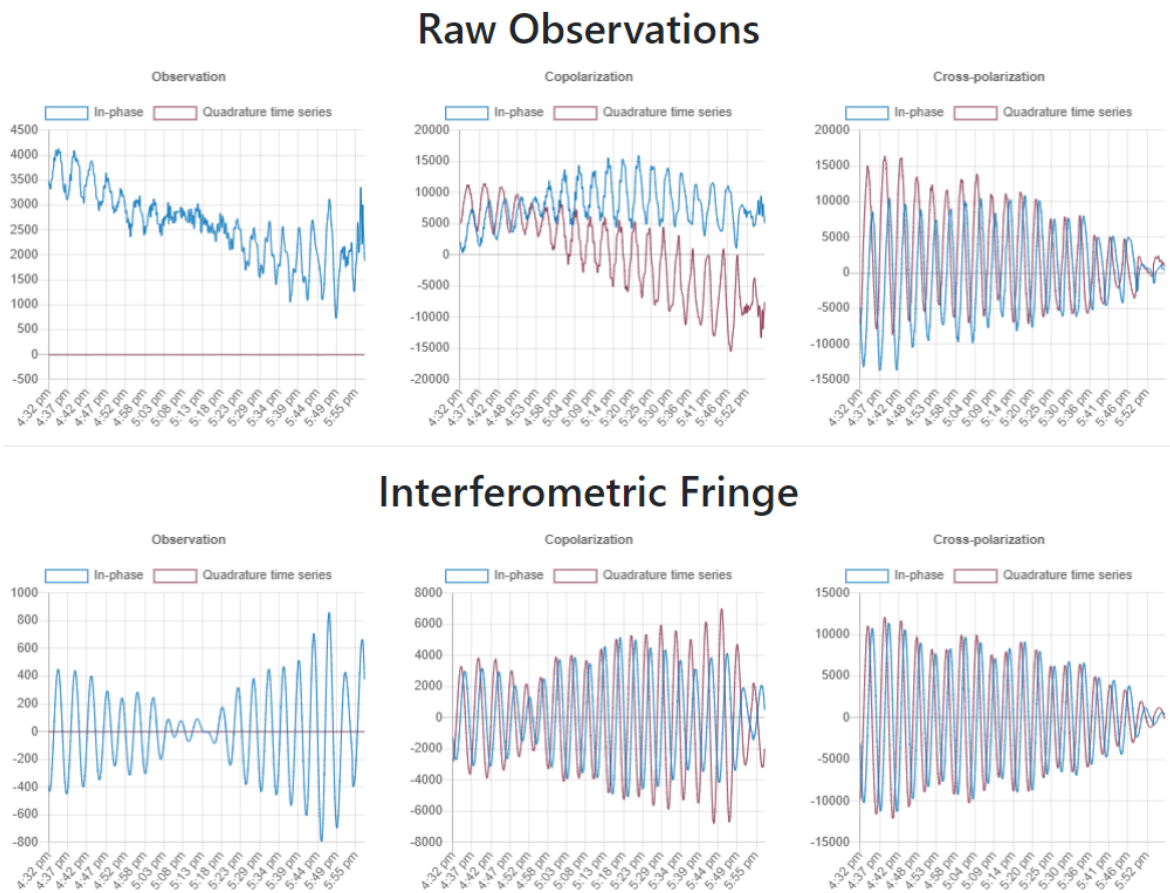


Figure 5.9: The observation representation panel for the ground-based GNSS-Reflectometry module. Each track has six corresponding plots. The top row plots show the original raw data from the receiver output. The bottom row plots are the retrieved interferometric patterns from the raw observations. Each column is associated with one antenna. The columns from left to right are respectively based on the data from one up-looking antenna (RHCP), and two sea-looking antennas with RHCP and LHCP designs.

5.2 Detection of Microplastics

This part of the thesis aims to develop a module for a specific use-case application of GNSS-Reflectometry using the CYGNSS dataset. The module is used for the detection of microplastics over the oceans. In the following, we first describe the methodology of data analysis based on the introduced theory in chapter 2. The description is followed by detailed information about the implementation of the method.

Recalling formula 2.8, we can see that the Mean Square Slope mss , is mainly governed by two variables; the Fresnel coefficient \mathfrak{R} and the normalized bistatic radar cross section σ_0 . The Fresnel coefficient over the ocean depends on the signal polarization state, the complex dielectric constant of the water, the frequency, and the incidence angle. However, since the distance between two consecutive CYGNSS measurements is relatively close to each other, the changes in the Fresnel coefficient can be considered insignificant compared to the impact of ocean surface roughness. Figure 5.10 is plotted using an average salinity of 35 PSU and a temperature of 20 degrees Celsius and shows the impact of incidence angle on the reflectivity of surface in Left-Handed Circular Polarization. As can be seen from the figure, the Fresnel coefficient power loss is almost constant and minimal for the incidence angles below 70 degrees. Therefore, this range of incidence angles, i.e. 0 to 70 degrees, can be an appropriate span for detecting anomalies in NBRCS profiles. The impacts of temperature and salinity are not strong to make prominent changes in the NBRCS profiles. These impacts are shown in Figure 5.11 where the power loss due to the Fresnel reflection coefficient as a function of surface salinity, temperature against different incidence angles are depicted.

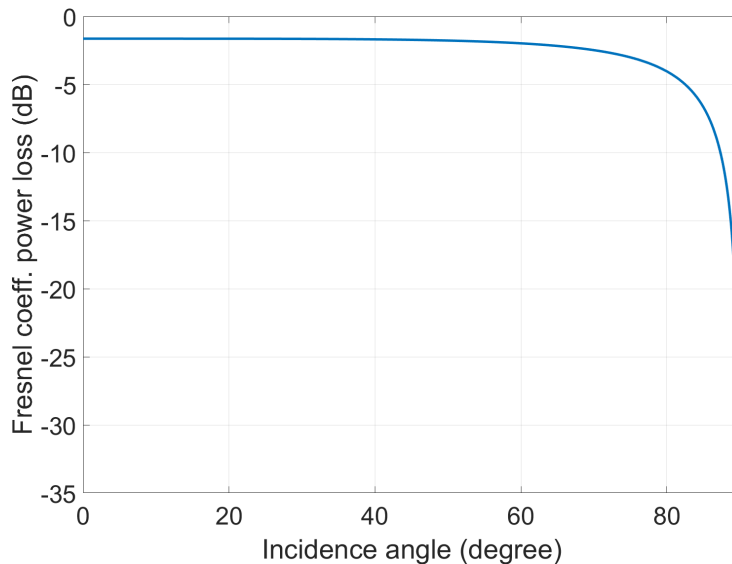


Figure 5.10: The power loss due to Fresnel reflection coefficient or the reflectivity of ocean surface at the salinity of 35 psu and temperature of 20 degrees Celsius against different incidence angles.

The effect of all the three parameters influencing the Fresnel reflection coefficient, or surface reflectivity, are summarized in Figure 5.12. The figure highlights that the highest power loss due to the reflectivity happens at a higher incidence angle. However, even including the effect of higher incidence angles, the overall change hardly reaches 1.7 deci-

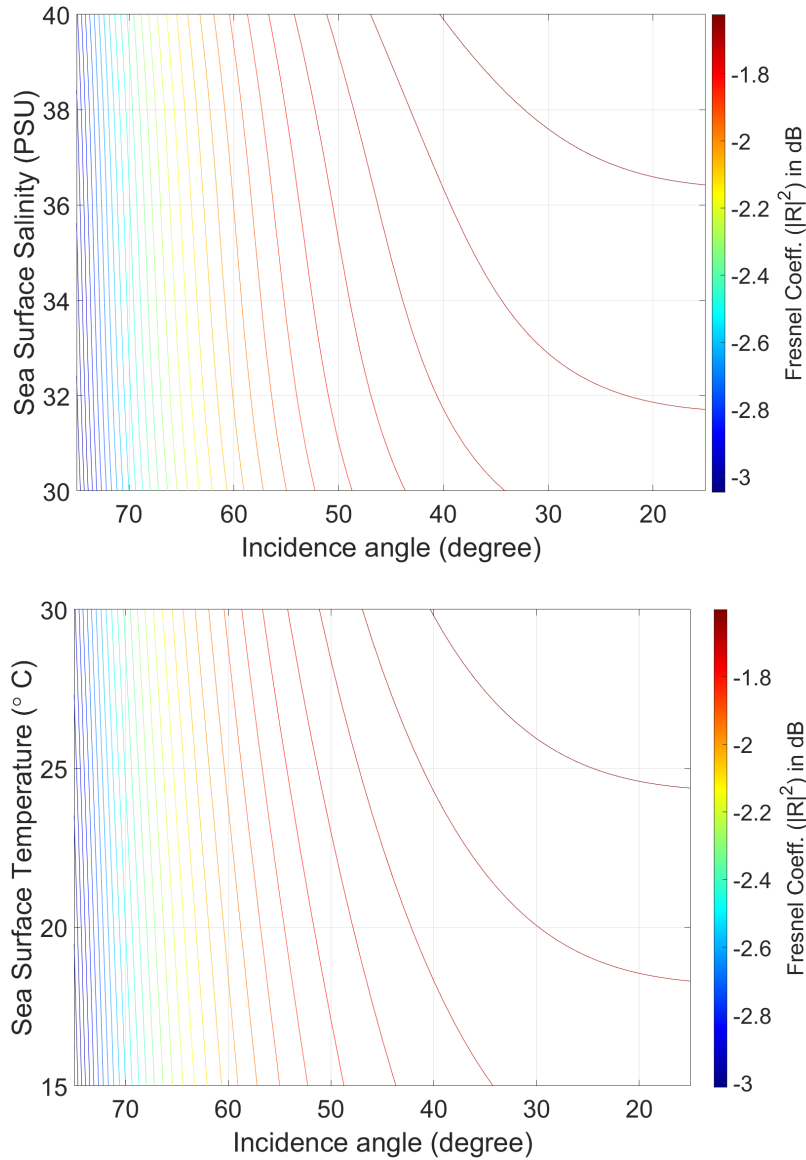


Figure 5.11: The variation of squared Fresnel reflection coefficient as a function of (top) sea surface salinity and incidence angle, (bottom) sea surface temperature and incidence angle.

bels (dB), meaning that the most important geophysical factor governing the fluctuation of NBRCS is the surface roughness. The main geophysical parameter responsible for the ocean surface roughness is wind.

There are, however, also other factors that affect the roughness of the ocean water. For example, the interaction of the ocean currents and the wind speed at the ocean surface can increase or alleviate surface stress, leading to a rougher or smoother ocean surface.

A simulation is conducted to demonstrate the effect of surface roughness on the NBRCS values. To this end, an artificial profile of mean square slope (MSS) is created (Figure 5.13 - top) over the ocean surface with 35 PSU salinity and 20 degrees Celsius temperature. The incidence angle of the track is considered to be from 15 to 75 degrees. Based on this setting, the corresponding NBRCS profile is generated using the equation 2.8 and

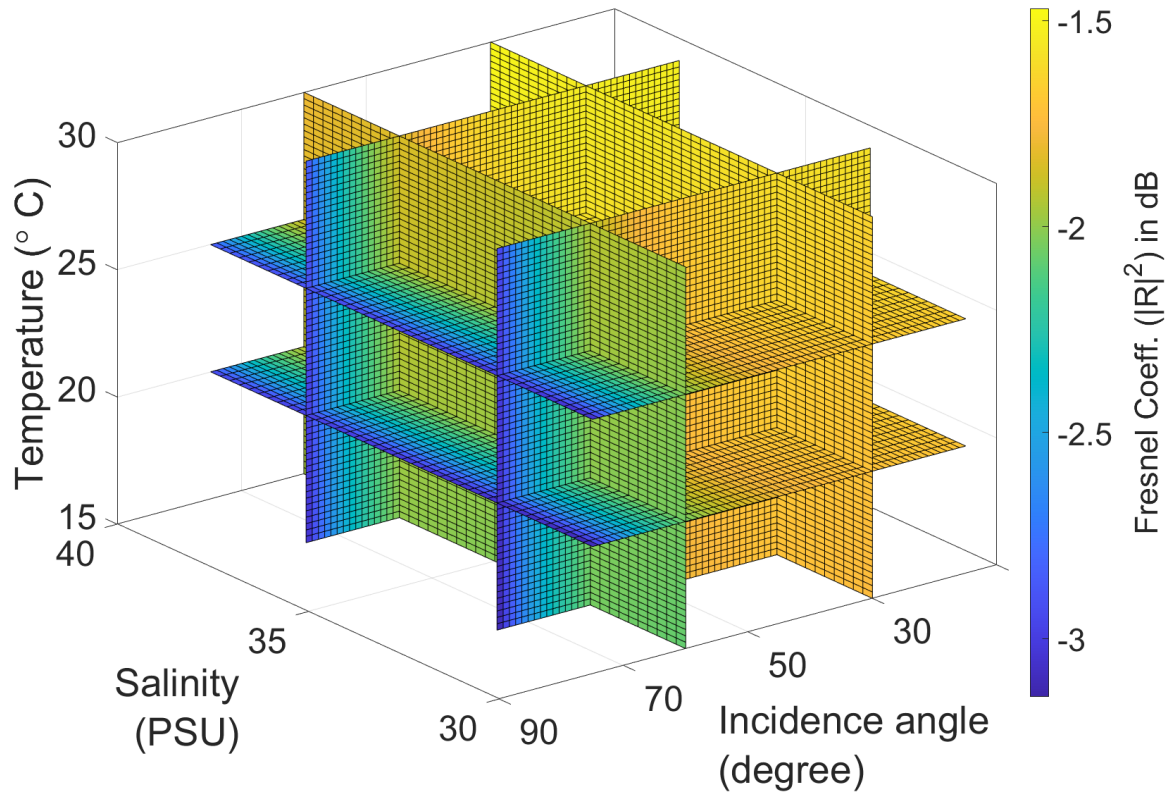


Figure 5.12: A representation of the effect of different parameters affecting the power loss due to the reflectivity of the surface. For better understanding two slices have been shown for each of the affecting parameters, i.e. incidence angle, salinity, and temperature.

is shown in the bottom panel of Figure 5.13. The NBRCS inversely responds to all the variations of MSS except for the incidence angles close to and above 70 degrees, where a slight decreasing behaviour is observed.

The simulation shows that a sudden increase of MSS by about 0.013 from 15 to 34 degrees incidence angle has led to 3 dB loss in NBRCS. Adversely, an abrupt decrease of about 0.009 in MSS between 49 to 57 degrees incidence angle has stimulated a sharp incline in NBRCS with a prominence of about 4.5 dB.

From all of this information, we gather the rationale for this project. By removing observations with poor quality, we avoid degradation of the analysis results. Wind speed is one of the most critical factors influencing ocean surface roughness. High wind speeds can create a turbulent effect on the ocean surface, which prevents the microplastic concentration on the ocean surface. To reduce this effect, we remove data with high wind speeds.

After filtering out the parameters we know affects the data, we examine the NBRCS data for unwarranted spikes. If the NBRCS data depicts a sudden change, there is some unknown external factor affecting the measurement. We want to see if there is a connection between these spikes and microplastic concentrations in the ocean. For this, we take the data for the spikes and compare it to known estimates over the microplastic concentration.

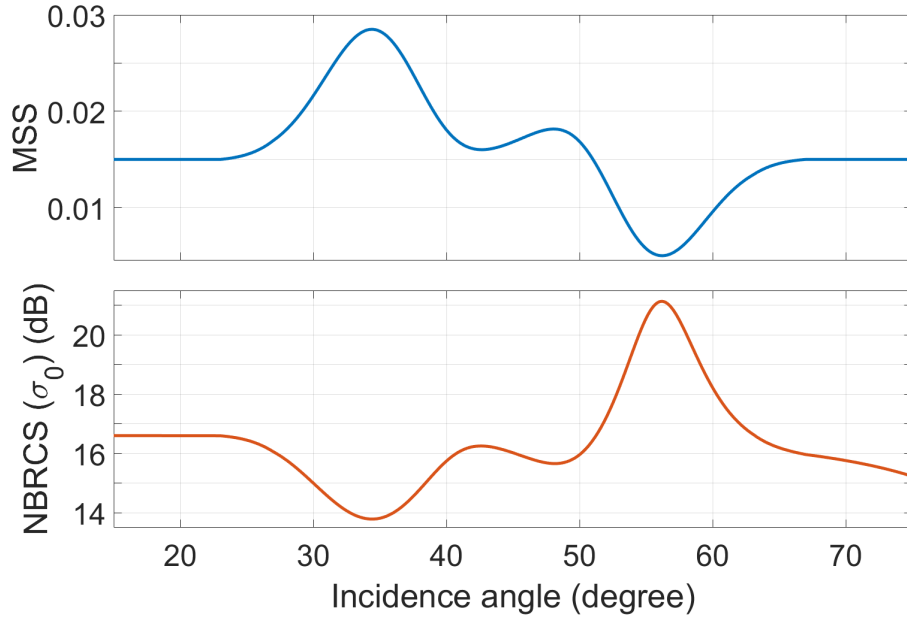


Figure 5.13: A simulated NBRCS profile based on artificial MSS values. The temperature and salinity of the ocean for this simulation has considered to be constant respectively at 35 PSU and 20 degrees Celsius.

The first step for this process is to collect the required data from the CYGNSS dataset. This is done by using the `collect_tracks` function 5.1 as presented in section 5.1.1 for all the available dates in the dataset. The date range for the data collected in this project is from March 18, 2017 to May 31, 2021 a time-span of 1535 days. For each data collection date, a new file with the track information is created and stored locally. The variables of interest collected for the processing of this project is presented and further explained in table 5.1.

Variable	Long name	Explanation	Usage
<i>sp_lat</i>	Specular point latitude	Specular point latitude, in degrees North, at <code>ddm_timestamp_utc</code>	Determine position
<i>sp_lon</i>	Specular point longitude	Specular point longitude, in degrees East, at <code>ddm_timestamp_utc</code>	Determine position
<i>track_id</i>	DDM Track ID	A track is a temporally contiguous series of DDMs that have the same <code>prn_code</code> .	Splitting dataset into tracks
<i>ddm_nbrcs</i>	Normalized BRCS	Normalized BRCS of a 3 delay x 5 Doppler bin box that includes the specular point bin.	Examine the state of the sea surface
<i>ddm_timestamp_utc</i>	DDM sample timestamp - UTC	DDM sample time. The number of seconds since <code>time.coverage_start</code> with nanosecond resolution	Determining time of measurement
<i>quality_flags</i>	Per-DDM quality flags	First group of the Per-DDM quality flags.	Find and filter out bad quality data

Table 5.1: The variables collected from the Level 1 CYGNSS dataset and used in the processing of data. This table shows each variable and its name, a brief explanation, and its use for this project. Source: podaac-opendap.jpl.nasa.gov/

After the CYGNSS tracks have been collected, it is time to start the processing of the data. The product from this processing is a list of peaks in the NBRCS variable over every available track. By examining the properties of these peaks at conditions where external factors should have minimal effect on the value, we expect to see a correlation between the peaks and the concentration of microplastics. The pseudo-code for the processing of a tracklist can be seen in code snippet 5.2.

Code 5.2: Pseudo-code for finding all applicable peaks in the given list of tracks.

```
1 def find_all_peaks(track_list)
2     peak_list = []
3
4     for track in track_list:
5         track = remove_bad_quality(remove_null_data(track))
6         track = check_distance_between_points(track)
7
8         if length(track) > 50:
9             peak_list = find_track_peaks(track)
10            peak_list = remove_peaks_on_land(peak_list)
11            find_nearest_peak_wind(peak_list, date, wind_data)
12            peak_list = remove_high_wind_peaks(peak_list, 5)
13
14     return peak_list
```

The function *find_all_peaks(track_list)* takes a list containing tracks as its input. It will then create an empty peak list (line 2) which eventually will be filled with valid peaks found in the dataset. The code will iterate over each track in the tracklist (line 4), firstly removing all the entries in the track with either a bad quality flag indicated by an odd number in the quality flag variable or having an invalid reading of the NBRCS being the value -9999 (line 5).

After this data has been removed, we check each track for significant distances between two adjacent points and split tracks if the distance between two points is larger than 100 kilometres. Then we check if the track has more than 50 data points. If it does not, we regard it as too short to be giving us a good reading of the NBRCS profile and the track is disregarded.

For the tracks with more than 50 points after being pruned, we run a separate code that examines the track and collects all the valid peaks (line 9). The code for this function *find_track_peaks(track)* is shown in code snippet 5.3.

In this function, we start by creating an empty variable *peak_list*, and we instantiate the variables for the longitudes and latitudes. Then we calculate the distance between each point using geodesic calculations to get a variable *x_axis* which will represent the distance on the track for each point (line 12-15).

Code 5.3: Pseudo-code for finding the peaks of a given track.

```
1 # Tracks are presented as a list of arrays on format:
2 # [latitudes, longitudes, NBRCS, timestamp, Quality Flag]
3
4 # This function checks the NBRCS values over a given track to find peaks in the dataset.
5 def find_track_peaks(track):
6
7     peak_list = []
8
9     lats = track[0]
10    lons = track[1]
11
12    for index in length(lat):
13        # The X-Axis will be the along-track distance given in meters.
14        x_axis = find_distance_between_points(
15            lats[index], lons[index], lats[index + 1], lons[index + 1])
16
17        # The Y-Axis will be the track NBRCS readings on the decibel scale.
18        y_axis = 10 * log(track[2])
19
20        # Apply filter to the data giving a continuous curve representation of the NBRCS
21        smooth_y = uniform_filter1d(y, size=10)
22
23        # determine the peaks of the smoothed NBRCS data
24        peak_indices, peak_properties = signal.find_peaks(smooth_y, prominence=1, width=5)
25
26        prominences = properties['prominences']
27        widths = properties['widths']
28
29        for peak in peak_indices:
30            peak_list.append([Lat[peak], Lon[peak], NBRCS[peak],
31                Time[peak], Prominence[peak], Width[peak]])
32
33    return peak_list
```

The y-axis representation will be variables from the NBRCS measurements of the track. These are converted to the log10 scale and then smoothed to get a continuous curve representation of the data (line 21). the function to smooth the data *uniform_filter1d(data, size)* is provided by the **Scipy.ndimage** package and takes the array of data and the length of the uniform filter as its input. The way this functions works is that it takes the arithmetic average of each point and its neighbours. The size represents the size of the sub-array for the calculation of the arithmetic average.

After the NBRCS variables has been smoothed, we use the function `find_peaks(data, prominence, width)` from the **Scipy.signal** package (line 24). This function takes the threshold for the prominence and width of a detected peak in the given data array. For this project, a prominence of 1 and a width of 5 was selected. Figure 5.14 shows the plot of four arbitrarily chosen tracks. In this figure, the purple dots represent the raw NBRCS value, the yellow line represents the smoothed NBRCS curve, and the red cross represents a peak detected in the dataset. This function returns a list of indices for detected peaks and metadata for the associated peak.

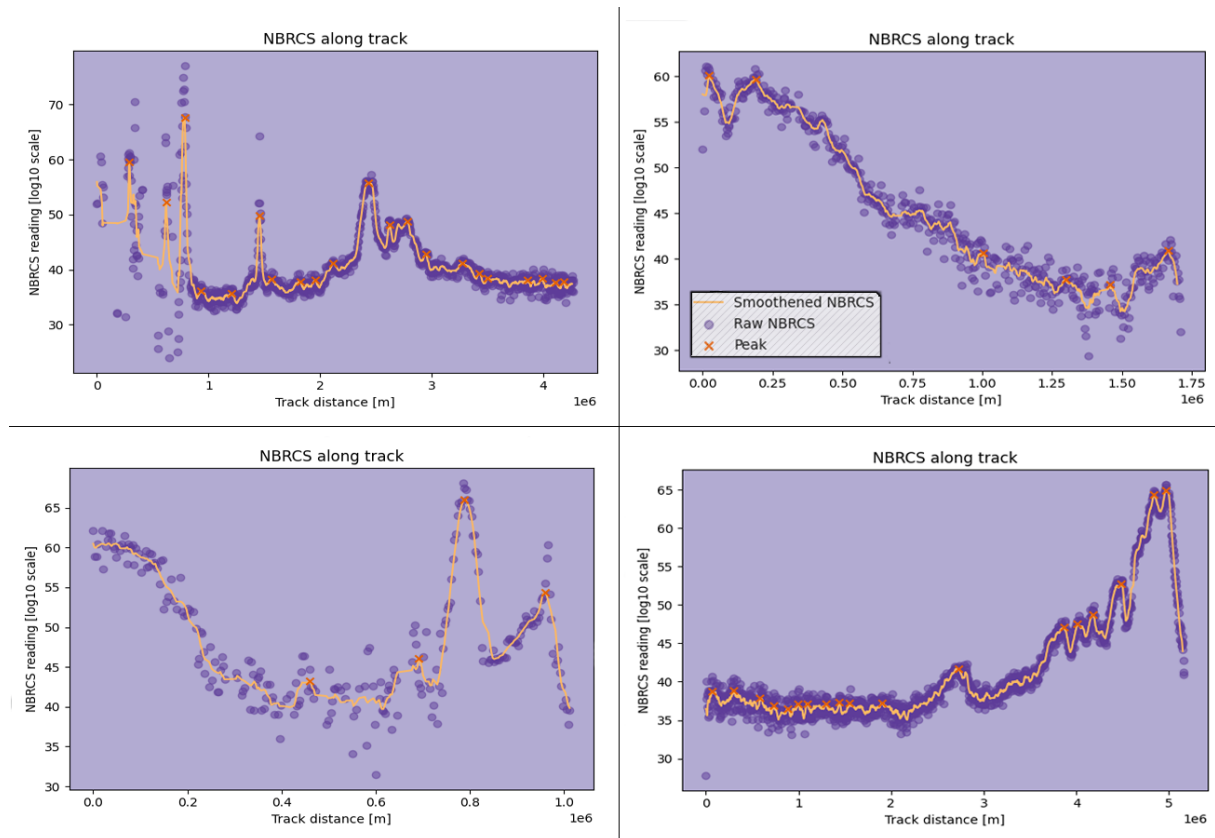


Figure 5.14: This image shows the representation of four separate tracks. The purple points show the raw data collected from CYGNSS, the yellow line shows the smoothed data while the red crosses indicates a detected peak in the data. The x-axis represent es the distance of the track in meters, while the y-axis represent the NBRCS values in log 10 scale.

Finally, we iterate over each detected peak from the list of indices and add the peak to the `peak_list` variable. Each peak appended to this list is an array containing the variables latitude, longitude, NBRCS measurement, timestamp, prominence and width. This list is then returned in the previously mention code snippet 5.3 (line 9) as the variable `peak_list`.

For each peak in the provided peak list, we check and remove points above land to make sure that we only look at the peaks located above the ocean surface (line 10). To examine the peaks where we expect low changes in the NBRCS variable, we need to have a measure of the wind velocity over the sea surface for each of the peak measurements. This is done using the `find_nearest_peak_wind(peak_list, date, wind_data)` function (line 11). The code for this function are found in code snippet 5.4.

Code 5.4: Pseudo-code for the extraction of wind velocity above each peak.

```
1 wind_data = ERA5_wind_file(date.month)
2
3 def find_nearest_peak_wind(peak_list, date, wind_data)
4     for peak in peak_list:
5         time = peak[3]
6         hour_of_day = time.get(hour) + 24 * (date.day-1)
7
8         peak_lat = peak[0]
9         peak_lon = peak[1]
10
11         # Find the nearest positions on the grid
12         lat_index = round((peak_lat - 45) / -0.25)
13         lon_index = round((peak_lon + 180) / 0.25)
14
15         wind_speed = hypotenuse(wind_data['u10'][hour_of_day][lat_index][lon_index],
16                                 wind_data['v10'][hour_of_day][lat_index][lon_index])
17         peak.append(wind_speed)
18
19     return peak_list
```

Firstly the downloaded wind data for the given month of measurement is loaded. This data is downloaded from the ERA5 Reanalysis dataset presented in section 4.2. The wind data is presented as a gridded dataset with a step-size of 0.25 degrees in both directions for every hour of a month, meaning that in order to find the wind speed above the ocean surface for a peak measurement, we need to find the nearest hour of the month for the measurement and we need to round the latitude and longitude to find the closest point on the grid.

Since the dataset gives us the U and V components of the wind speed, we can calculate the velocity by the hypotenuse of the two vectors, giving us a reasonable estimation of the wind velocity above the peak at the measurement time. This wind speed is added to the peak array and returned to the code snippet (line 11) 5.3.

Before saving the list of peaks to a file, the last thing we do is to remove all the peaks with a wind velocity greater than 5 meters per second, ensuring that the peaks we have collected will not have significant changes in the sea surface roughness due to the wind. The list of peaks can then be plotted or further processed to examine the correlations between the peaks in the NBRCS and the concentration of microplastics.

Chapter 6

Results & Discussion

This chapter will present the processed GNSS-R data presented in the detection of microplastics section 5.2. Firstly, we present the result produced using the complete dataset over the period of ~ 4 years on a global scale and compare the results to the microplastics concentration models presented in section 4.3. Finally, we will take a closer look into the processed data from five major basins of the ocean and the Mediterranean sea over a one-year period and examine the average data time series.

6.1 A Global Picture

This section presents and discusses the processed data on a global scale over the collection period from March 18. 2017 to May 31. 2021, a period consisting of 1536 days with a total number of 10,565,718 peaks detected.

The first plot, figure 6.1, presents the global peak density. The density is calculated by counting the number of detected peaks falling into 1° by 1° grid. This parameter provides a good indication of the areas that have a higher concentration of discrepancies in the NBRCS data, being the areas with a higher concentration of microplastics.

From the figure, one can observe that the highest concentration of peaks is on the western coast of the USA. There are also high concentrations between the islands near Indonesia and the Philippines and other bigger islands like Madagascar, Japan and populated areas like Hawaii and around the peninsula of Florida.

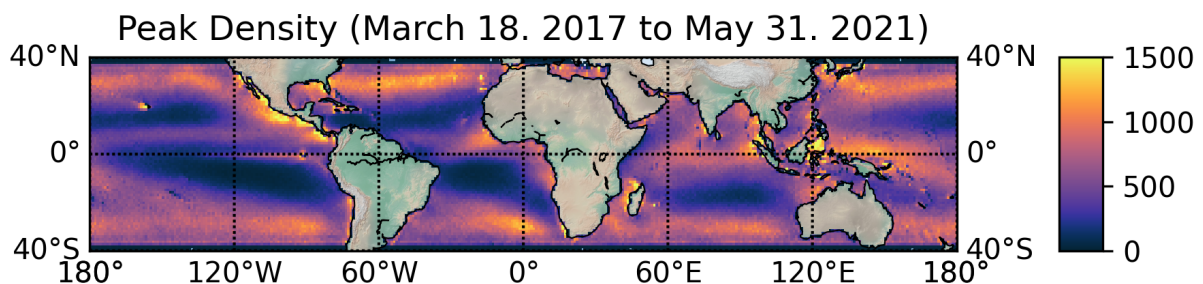


Figure 6.1: The global peak density on a $1^\circ \times 1^\circ$ grid spanning from March 18. 2017 to May 31. 2021.

This high concentration can be a result of several factors. The first thing to consider is that the areas with the highest concentration of peaks detected are near highly populated areas that can act as a source of marine pollution. This might, however, also be caused by higher activity in the coastal region which can be a source of noise on the reflection measurements.

We can also observe a higher concentration of peaks in the northern hemisphere between 30°North and 40°North and the same between 30°South, and 40°South. These areas of higher concentration corresponds nicely with the oceanic currents, which are known to accumulate plastics into big garbage patches in the oceans, especially apparent for the high concentration area in the northern Atlantic ocean and the northern Pacific ocean.

If we compare this figure with the models for microplastic counts as presented in section 4.3, we can see that we have many similarities with the dataset. As for our data, the higher concentrations are located near areas with oceanic currents. The main difference being that the models presented to estimate the largest concentration of microplastics on the northern Pacific ocean, in the Mediterranean sea and on the eastern coast of China. This deviation from our results might result from the limited data used by the microplastic models to estimate the concentration.

Examining metadata about the detected peaks might also lead to interesting conclusions. For example, figure 6.2 shows the prominence of the peaks averaged over 1° by 1° grid. The prominence is a measure of the significance of the spike in the data resulting in the peak. In this figure, we can see a higher prominence along the coastlines and near islands. This corresponds to areas with a higher concentration of peak density from the global peak density figure. The prominence also seems to be somewhat consistent over the oceans save for the areas corresponding to those with a lower concentration of peak density.

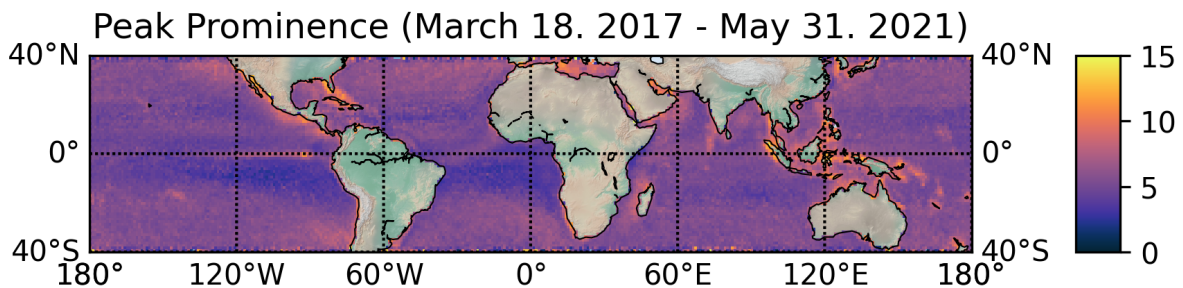


Figure 6.2: The global peak prominence averaged over 1°x 1°grid, spanning from March 18. 2017 to May 31. 2021.

These spikes in peak prominence suggests that areas near highly populated coasts and island has a higher significance on the observations. This effect could be a result of a higher concentration of marine pollution or noise due to human activity. There could also be other external factors affecting prominence like wind speeds, ocean currents or the factors from the nearby land.

The final global variable presented, figure 6.3, shows the widths of the peaks. The width of a peak is a measure of the physical length of the peak presented in an averaged 1° by 1° grid.

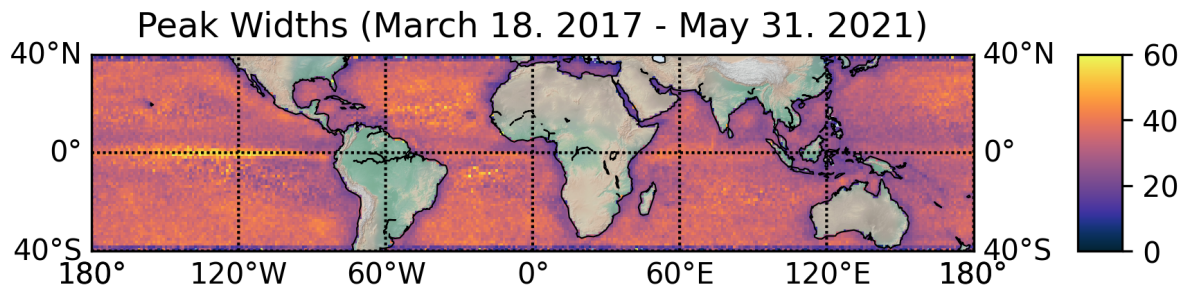


Figure 6.3: The global peak width on a 1°x 1° grid spanning from March 18. 2017 to May 31. 2021.

The data from this figure seem to be pretty consistent, except for a large concentration of higher widths near the equator in the Pacific ocean. This area of high concentration is very interesting as it is an area with a relatively small density of peaks. We can also see that areas near land have a lower measurement of peak width.

6.1.1 The Effect of Ocean Currents

Another factor to consider when evaluating the concentration of peak densities is the sea surface roughness caused by strong currents. A map of the average global ocean currents can be seen in figure 6.4.

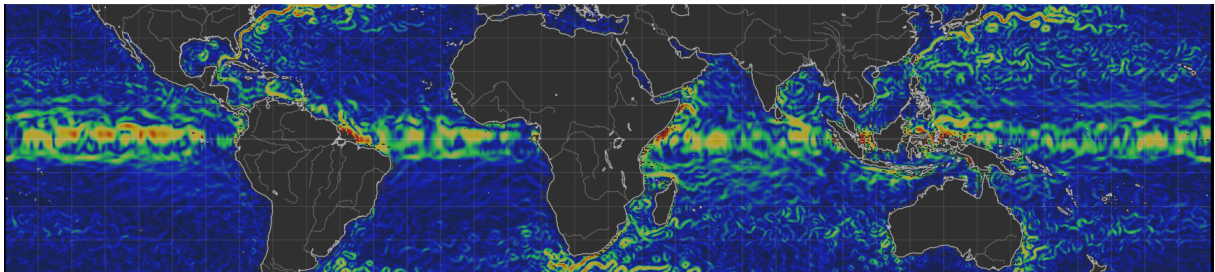


Figure 6.4: A global map for the average oceanic currents generated using the OSCAR dataset. Source: [14]

Unfortunately, we have not collected data for the surface currents in this thesis. However, we can make certain adjustments to the collection of wind speeds to dampen the impact of sea surface currents to get an indication of how it affects our data. The ocean surface wind stress (τ), can be described by equation 6.1 [46]:

$$\tau = \rho_a C_D (W - U) |W - U| \quad (6.1)$$

Where ρ_a is the air density, C_D is the drag coefficient, and W and U are the 10-m wind speed and surface current speed, respectively. From this formula, we can conclude that the impact of surface currents can be more noticeable for lower wind speeds. By filtering out density peaks for points with wind speeds below 3 meters per second, we can see some changes in the areas with higher speed of surface current. The plot shown in figure 6.5 illustrates the changes.

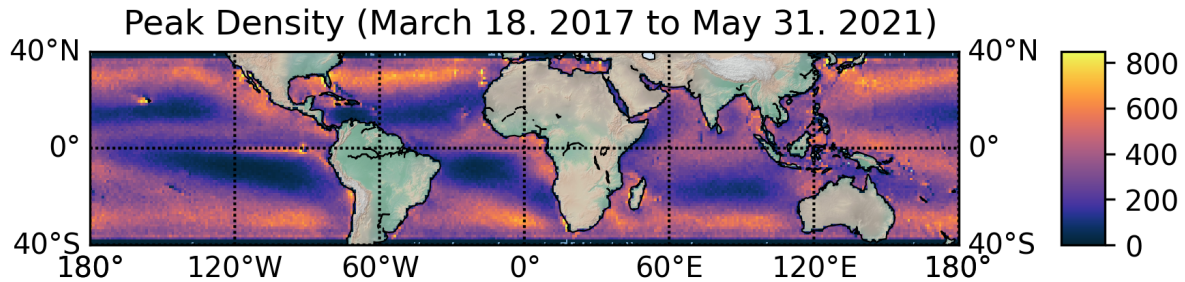


Figure 6.5: The global peak density on a 1°x 1°grid spanning from March 18. 2017 to May 31. 2021 for wind speeds between 3 and 5 meters per second.

If we compare this figure with the global peak density figure 6.1, we can see that there is a lower density on the west coast of the USA as well as around the islands between Indonesia and the Philippines, both areas with powerful currents. However, the rest of the areas on the map seem to be reasonably consistent with the previous results, i.e. before filtering out the peaks with wind speeds below 3 m/s.

The conclusion from this inspection is that the ocean surfaces currents impacts our way of estimating the roughness of the ocean surface. The interactions between the surface currents and peaks in the NBRCS should be further examined in the future, especially for estimations over the areas with lower wind speeds.

6.1.2 Seasonal Changes in Data

To investigate for any seasonal variation in the collected peaks, the results has been grouped into four seasons of three months per year. This will give an indication on the seasonal distribution of microplastics. The plots from figure 6.6 highlights the seasonal variations.

Figure 6.6 shows a difference for the seasonal concentrations of peaks. Between April and September there is a higher concentration of peaks in the northern hemisphere. Between October and March there is a higher concentration of peaks in the southern hemisphere. This seasonal change in concentration could be due to seasonal changes in atmospheric and oceanic circulation patterns.

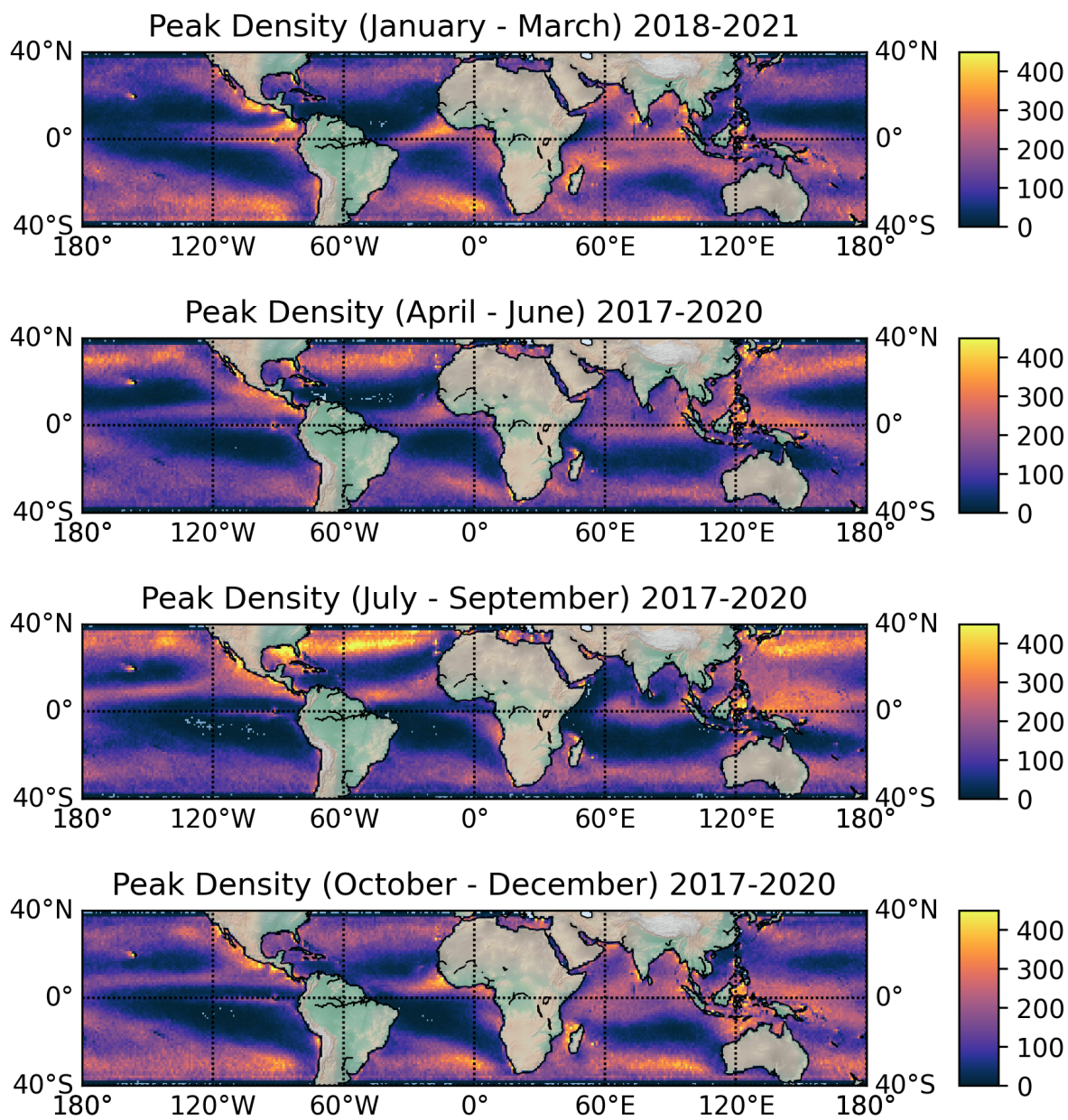


Figure 6.6: Seasonal representation of the global peak density on a 1°x 1°grid over a total period of 4 years.

6.1.3 Average Global Peak Density

To get a better overview of the changes in the global concentration of peak densities, a monthly time series is presented, as seen in figure 6.7.

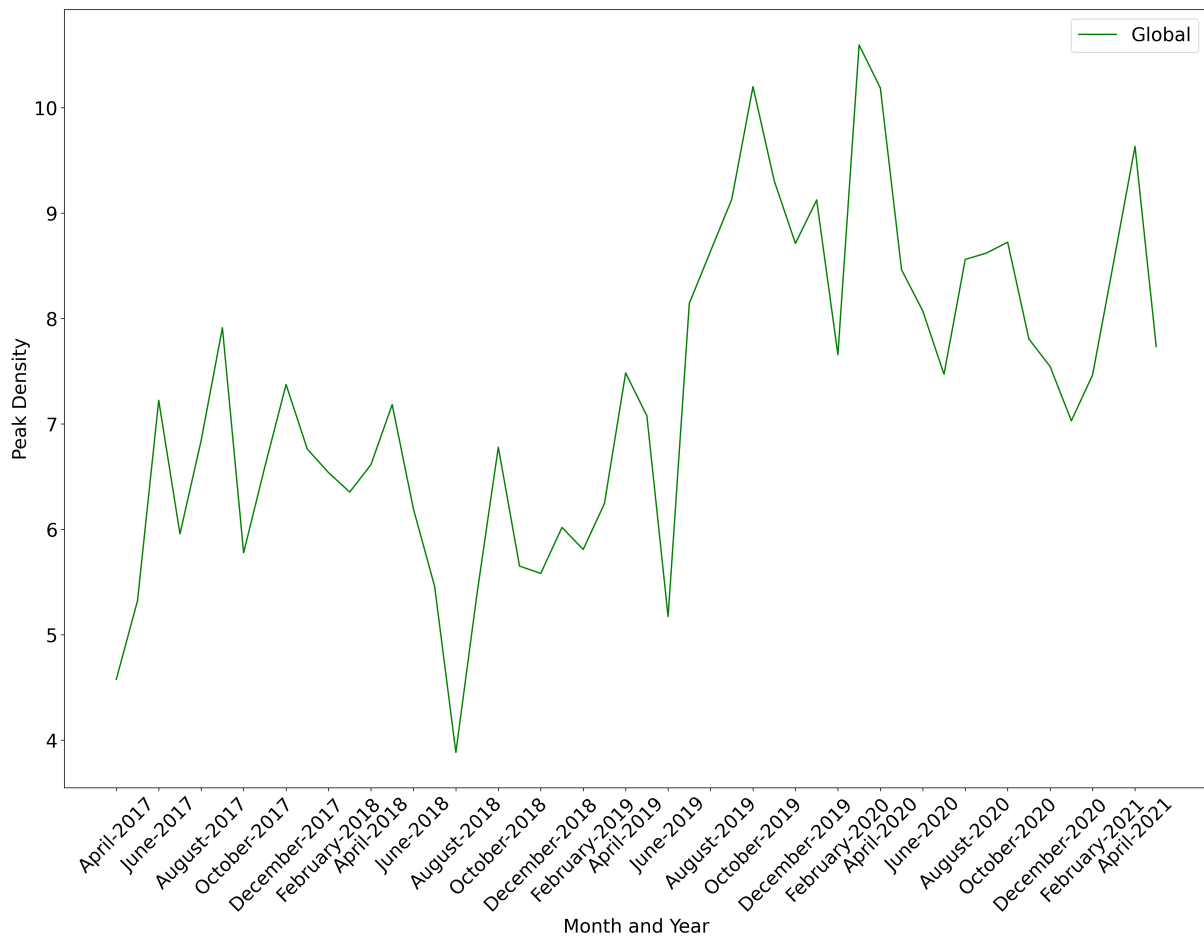


Figure 6.7: A time series of worldwide average of the peak densities on a monthly temporal resolution.

The first notable change in figure 6.7 is the jump in average density from July 2019. This change makes sense as from this month, the sample rate for collecting data doubled (from 1 Hz to 2 Hz). This means that there are more points in the dataset, and more peaks will be detected. Other than that, the spikes in the time series show no apparent trends in the pattern over time.

In the next section, the five major basins of the ocean and the Mediterranean sea are investigated for further detailed information about regional distribution of microplastics and corresponding temporal variations.

6.2 Inspection of Basins

This section will take a closer look into the peak densities of the five major oceanic basins; the north and south Pacific ocean, the north and south Atlantic ocean and the Indian ocean as well as the Mediterranean sea.

We will examine the difference in peak density over 12 months, spanning from October 2019 to September 2020 for each basin. We will also examine the time series for the average grid peak density for each of the basins.

6.2.1 The North Pacific Ocean

For the North Pacific basin, the region is selected within the boundaries latitudes 0° to 40° North and longitudes 125° East to 135° West.

The comparison between the microplastic count models and our global peak density is shown in figure 6.8. The North Pacific region is one of the areas with the highest concentration of microplastics for all models. Comparing the models to our global peak densities show a remarkable similarity with all models. There is a high consistency of peaks from 20° North and northwards over the entire boundary region. The main difference comparing the models with the global peak density is the high peak densities at the western coast of the USA and around the island of Hawaii.

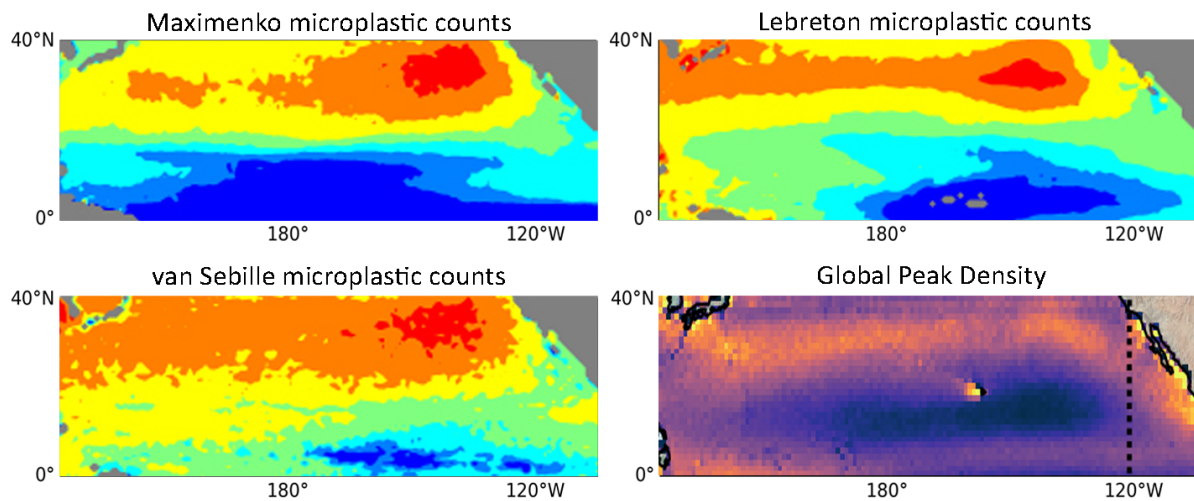


Figure 6.8: Cropped image of the North Pacific region for the three models for microplastic counts and the global peak density retrieved from the analysis of CYGNSS observations.

The peak density plots for the North Pacific ocean is presented in figure 6.9. These plots show a higher peak density at October 2019 and between April to September 2020. The highest densities of peaks appear in June, August and September. This pattern coincides with the seasonal observations from section 6.1.2, having a higher concentration of peaks in the warmer months.

The high-density areas do not seem constant but tend to lie near the northern and western parts of the plots. Comparing the density with known currents on the north pacific gyre, the high-density areas seem to lie along with the movements of currents. The area surrounding the centre of the currents seems to have a lower density for all the months. We can also observe a higher density of peaks around the island of Hawaii, near the western coast of the USA and around the Japanese island every month.

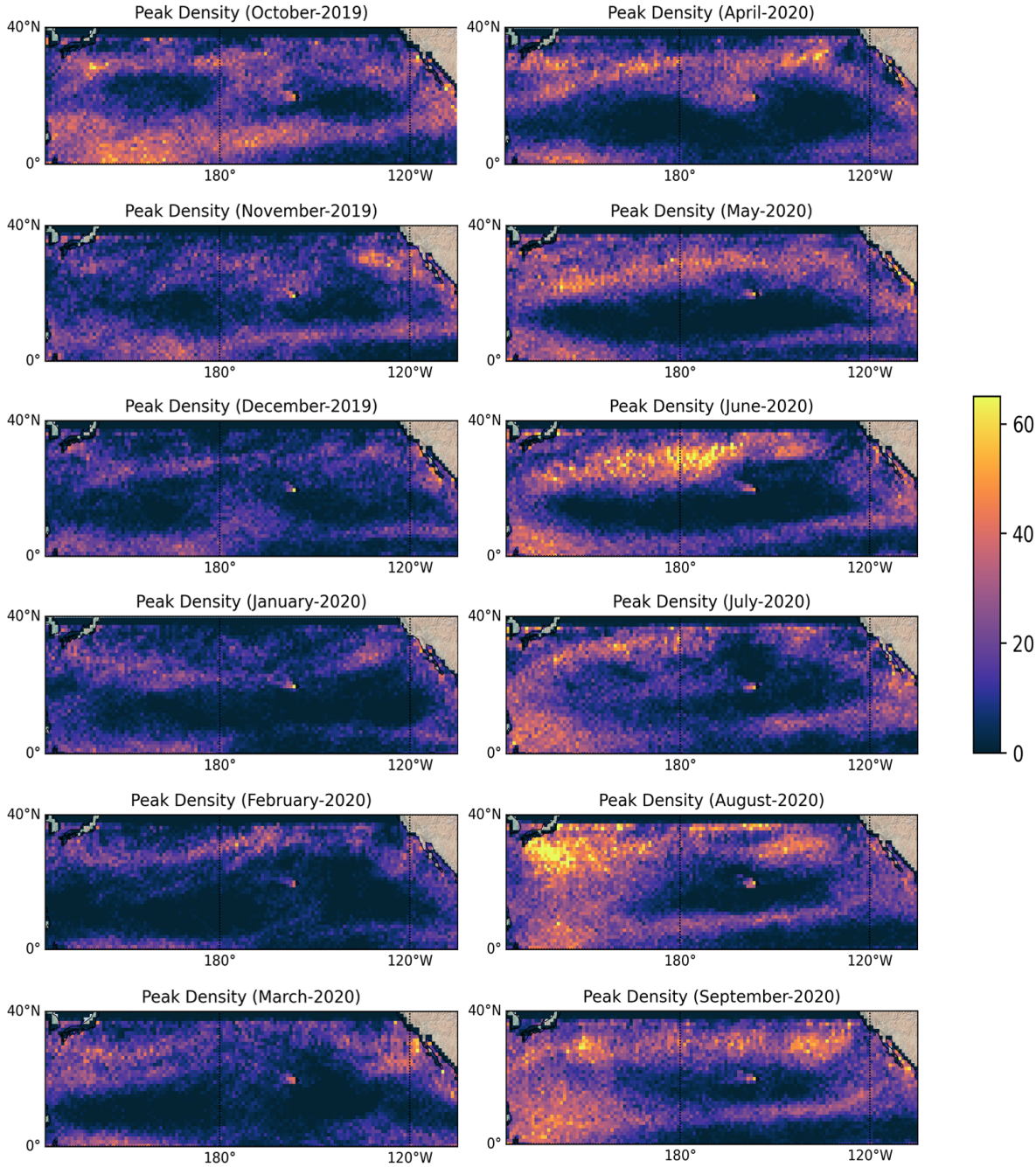


Figure 6.9: The monthly peak density over the North Pacific ocean region, on a 1°x 1°grid from October 2019 to September 2020.

6.2.2 The South Pacific Ocean

The next area of interest is the South Pacific within the boundaries from latitudes 0° to 40° South and longitudes 125° East to 65° West.

Figure 6.10 shows the comparison between the microplastic count models and our global peak density plot. The microplastic models over the south Pacific ocean depict a maximum concentration of counts near 85° west. For the rest of the basin, the models show a moderate amount of counts. The global peak density plot shows a similar pattern. The maximum values seem to be in a similar region near longitude 85° west. A difference between the models and the global peak density plot is the higher concentration of peaks at the western coast of South America, at the equator near the Galapagos islands and on the northwestern part of the plot near Papua New Guinea and the Solomon Islands.

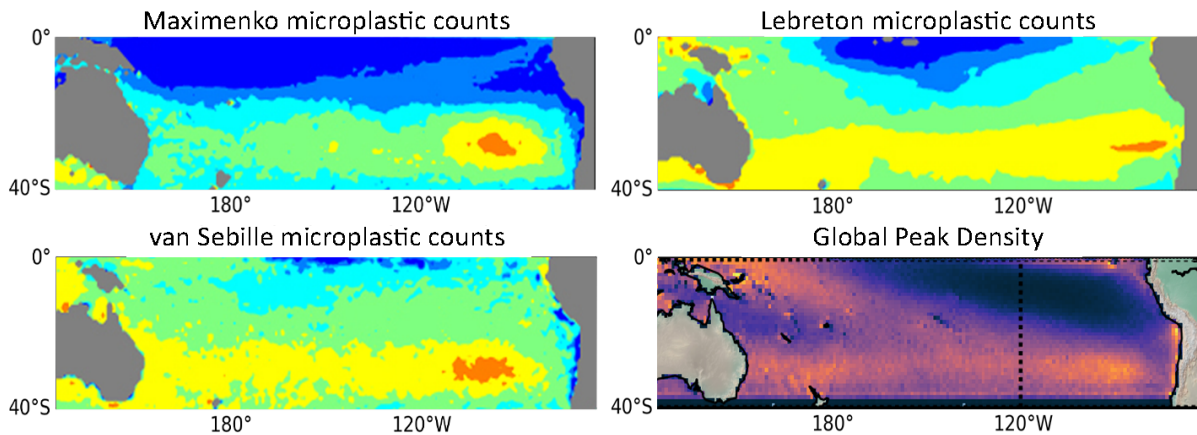


Figure 6.10: Cropped image in the South Pacific region for the three models for microplastic counts and global peak density retrieved from the analysis of CYGNSS observations.

The monthly peak density plots over the South Pacific ocean is presented in figure 6.11. In these plots one can see an opposite concentration in the peak densities compared to the North Pacific. These plots show a higher concentration of densities between October 2019 to April 2020 and relatively lower densities between May 2020 and September 2020.

In these plots, we can notice the highest peaks slightly east of Australia and west of southern America, but only during the southern hemisphere's summer months between October and March/April. During the other months, the peaks are consistently low. If we compare this data with the known currents of the South Pacific gyre, we can see that most of the high peak densities are on the southern part of the plot corresponding to the currents moving from Australia towards Peru. We can also see a consistent patch of low densities west of Peru for all the months, seemingly at the centre of the currents in the South Pacific gyre.

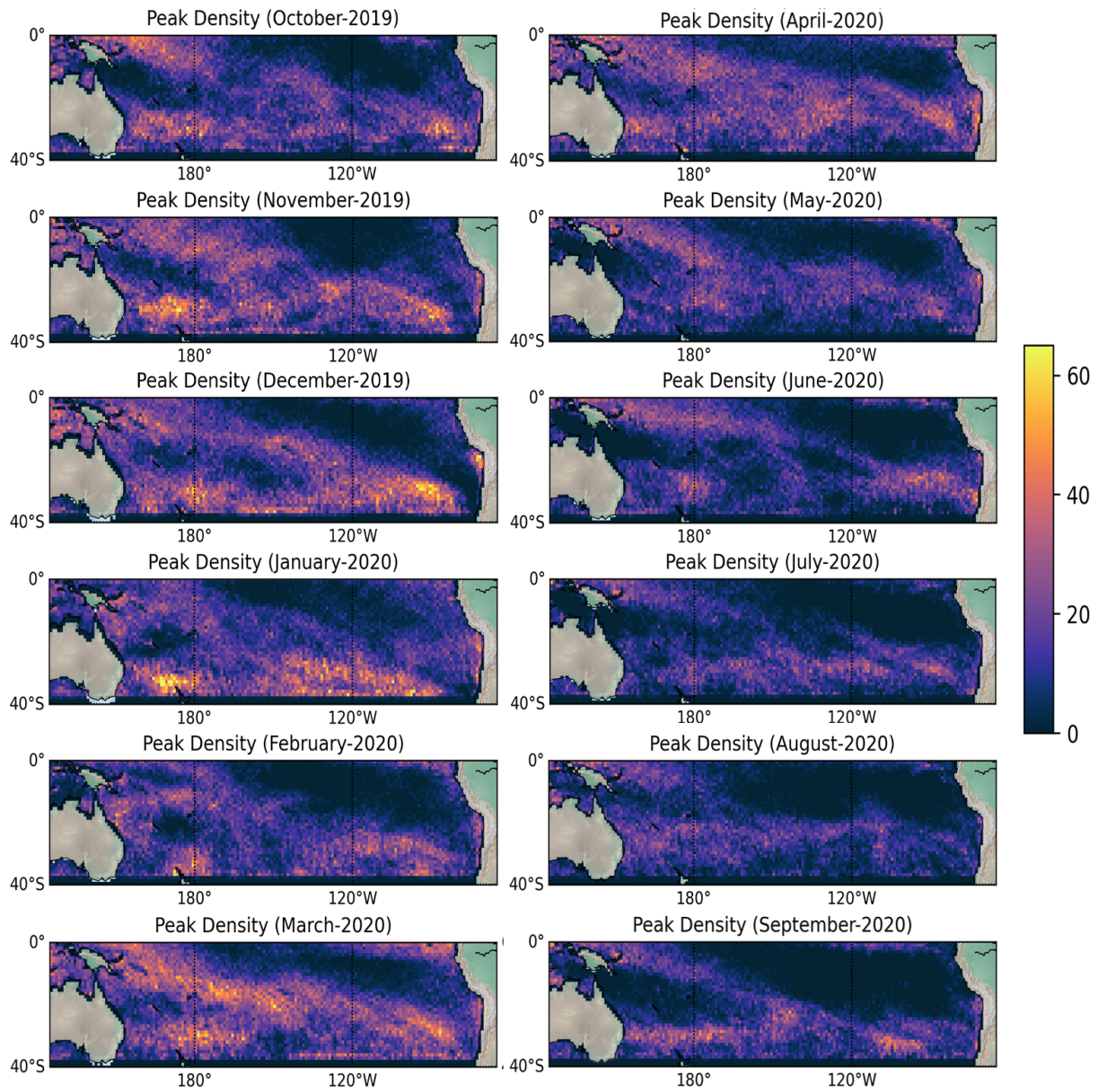


Figure 6.11: The monthly peak density over the South Pacific ocean region, on a $1^\circ \times 1^\circ$ grid from October 2019 to September 2020.

The time series for the average grid peak density for the North and South Pacific is shown in figure 6.12. In this figure, the time series for the North Pacific basin is represented as a blue line, while the South Pacific is represented as an orange line.

In the data for the North Pacific there is a clear difference in density for the summer months between April and September and the winter months between October and March. In the warmer months of the year, the average peak density in North Pacific is much higher than the winter months.

For the South Pacific, an opposite trend compared to the North Pacific is noticed. This line shows a higher peak density in between October and April, and lower densities between May and September.

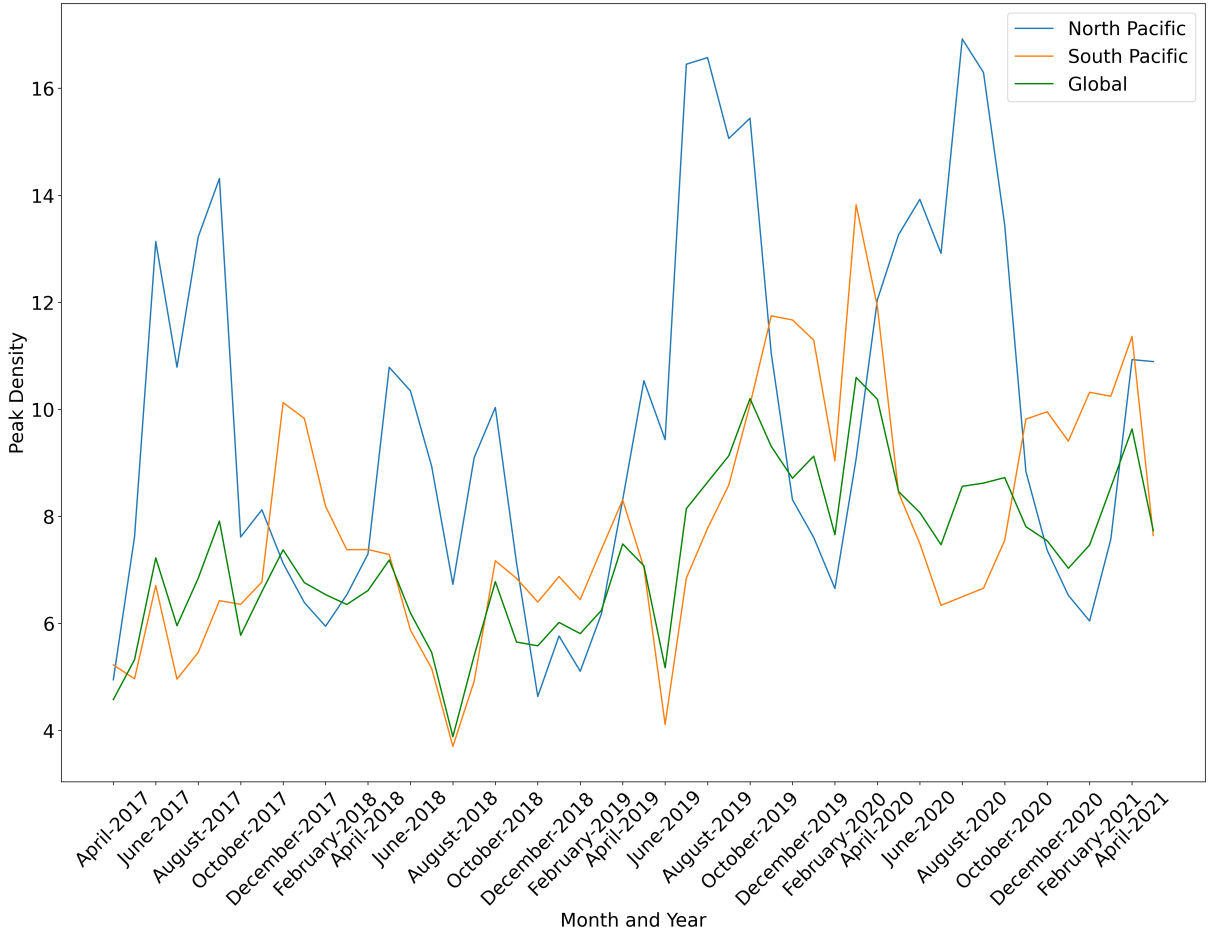


Figure 6.12: A time series showing the average grid peak density over the North- and South Pacific ocean.

6.2.3 The North Atlantic Ocean

The boundaries for the North Atlantic ocean is between latitudes 0° to 40° North and longitudes 75° West to 0°.

Figure 6.13 compares the microplastic count models and the global peak density. The models show the highest concentration in the northern part of the region from around 20° North and upwards. The van Sebille model of microplastic counts shows a higher concentration compared to the other two. The global peak density shows a similar concentration of peaks from latitude 20° North and northwards. A difference between the global peak density and the models is the high peak density in some parts of the western coasts of Africa.

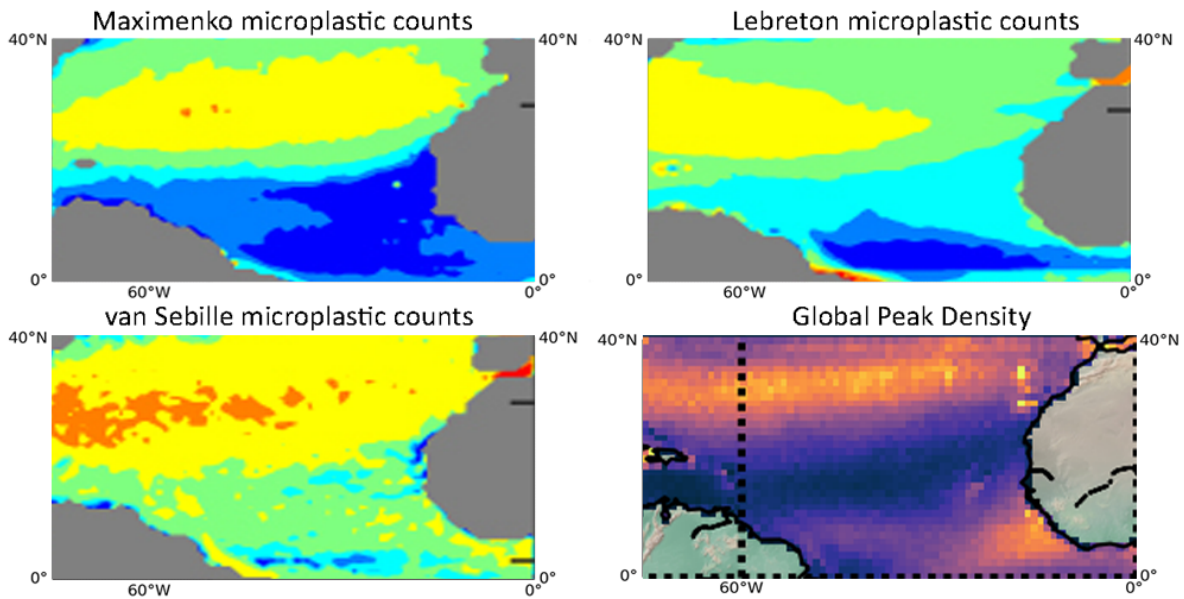


Figure 6.13: Cropped image in the North Atlantic region for the three models for microplastic counts and global peak density retrieved from the analysis of CYGNSS observations.

The peak density plots for the North Atlantic ocean is shown in figure 6.14. The data in these plots show a higher concentration of peaks for the warmer months and October. There seems to be a higher concentration of peaks in general over the entire period compared to the previous basins. The plots also show an area of low concentration at the centre of the plots.

The high concentration of peaks seems to be between the northeastern part of South America and the southwestern part of Africa. These areas are near the equatorial current and along the gulf stream. The lowest peak concentration seems to lie between the two currents.

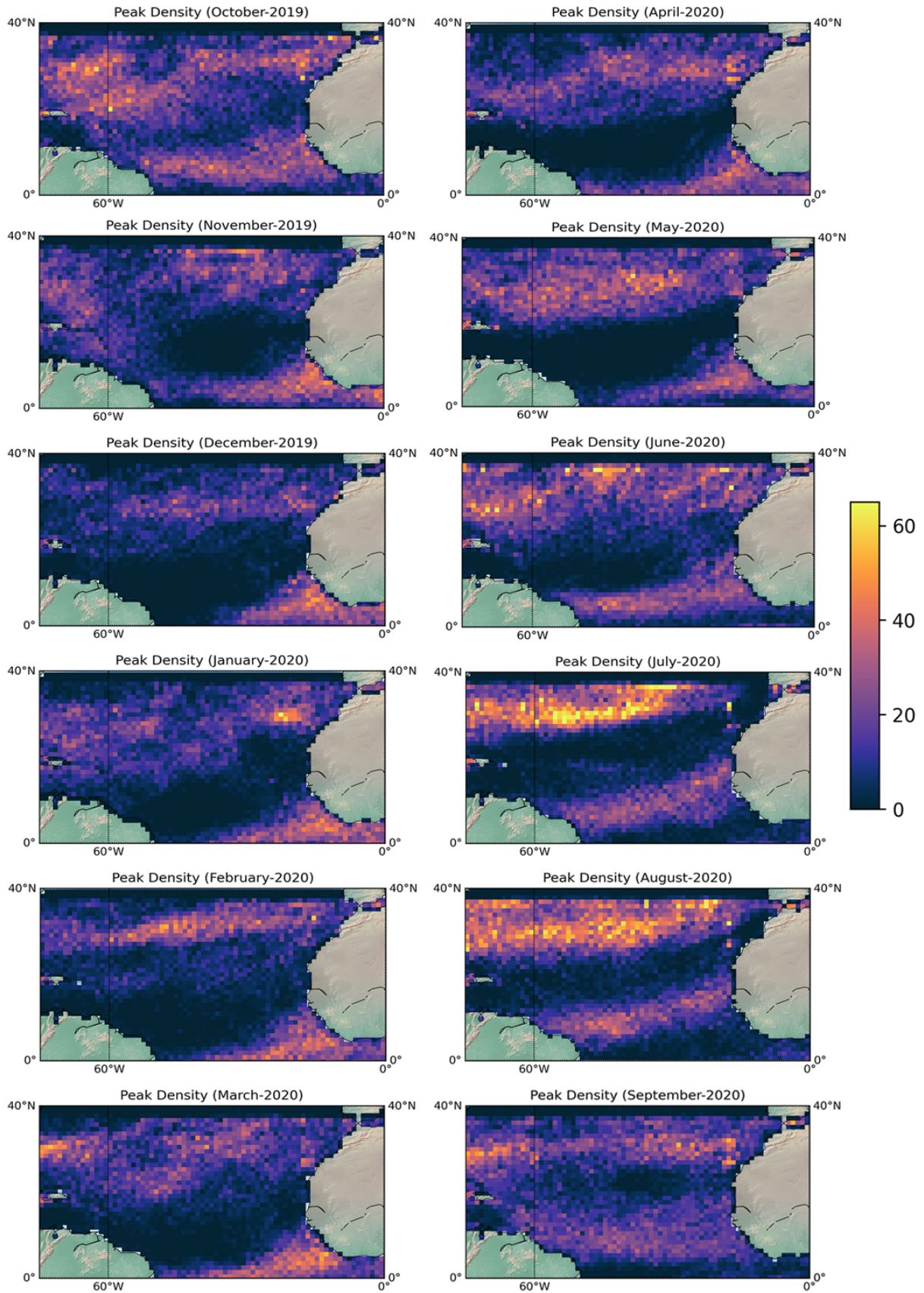


Figure 6.14: The monthly peak density over the North Atlantic ocean region, on a 1°x 1° grid from October 2019 to September 2020.

6.2.4 The South Atlantic Ocean

The boundary region for the south Atlantic ocean is between latitudes 0°South to 40°South and longitudes 60°West to 25°East.

A comparison between the microplastic models and the global peak density for the South Atlantic basin can be made from Figure 6.15. The microplastic models similarly predict high concentration from 20°South and down. The Lebreton model is slightly different, depicting high counts of microplastic on the eastern shore of South America. The global peak density also detect a high concentration of peaks from around 20°South and southwards. Similar to the Lebreton model, the global peak density has high values on the southern part of the eastern coast of South America. The peak density plot also shows a higher concentration of peaks on the coastal waters of southwestern Africa.

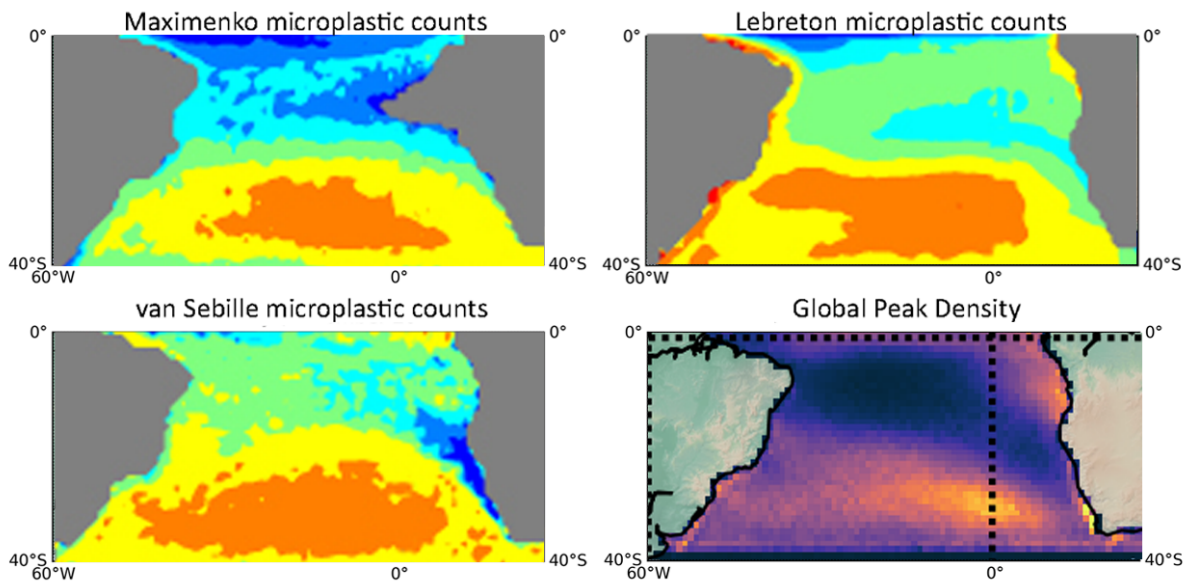


Figure 6.15: Cropped image in the South Atlantic region for the three models for microplastic counts and global peak density retrieved from the analysis of CYGNSS observations.

The South Atlantic ocean peak density plots can be seen in figure 6.16. These plots indicate a higher concentration of peaks between October 2019 and April 2020, the southern hemisphere's summer months. The areas with the highest overall concentration seem to be slightly west of the southern part of Africa, an area known for having strong ocean currents, stretching out towards central-southern America. Conversely, there seems to be an overall low concentration of peaks in the middle of the plots, an area with low ocean currents.

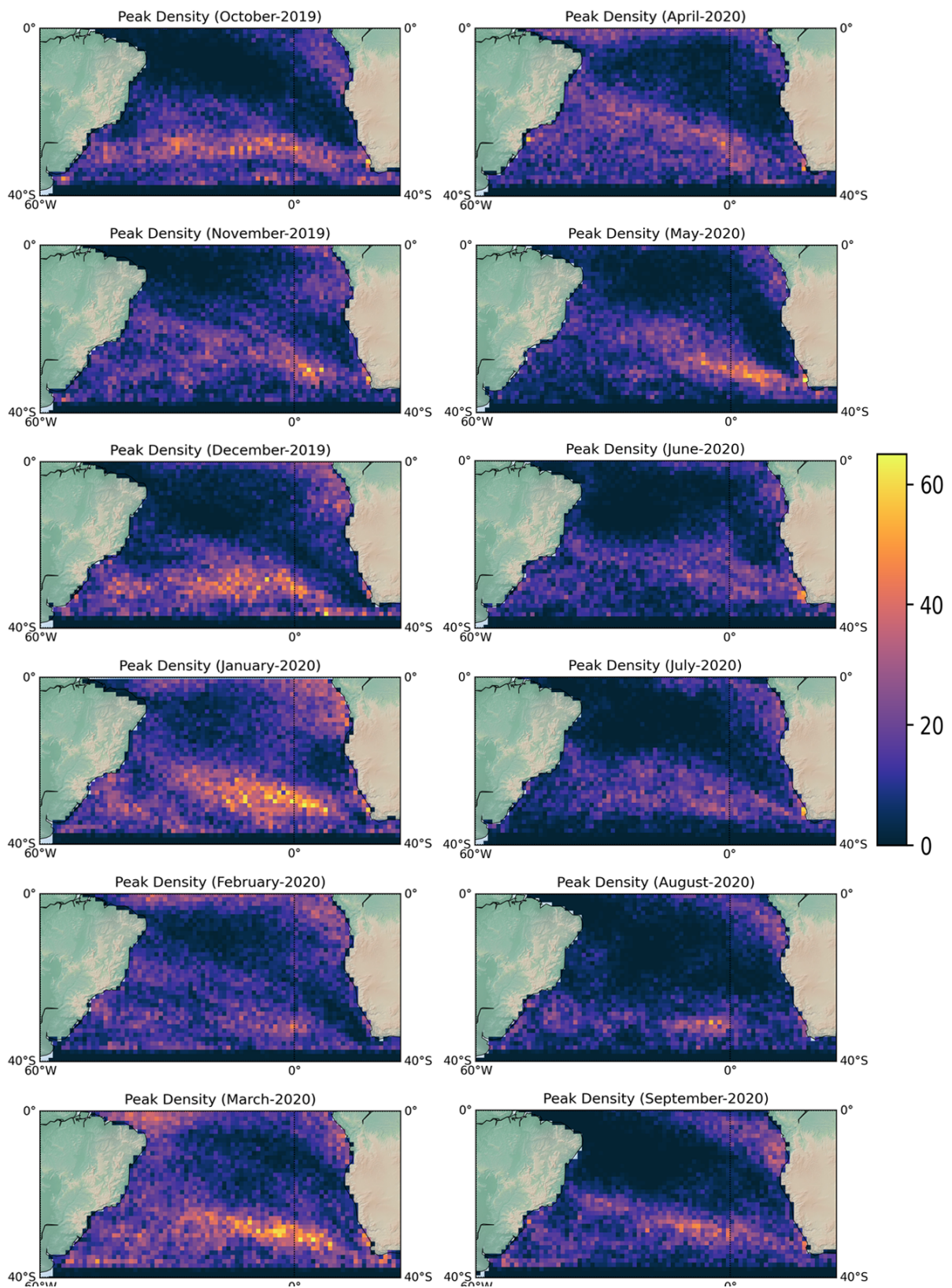


Figure 6.16: The monthly peak density over the South Atlantic ocean region, on a $1^\circ \times 1^\circ$ grid from October 2019 to September 2020.

In figure 6.17, the time series for the average grid peak density for the North and South Atlantic ocean is presented. In this plot, the data for the North Atlantic basin depicts a higher average peak density between April and October. This is similar to the results for the North Pacific ocean.

For the South Atlantic average peak density we see a higher average between September and May. This indicates that there are seasonal changes in the average grid peak density for the Atlantic ocean.

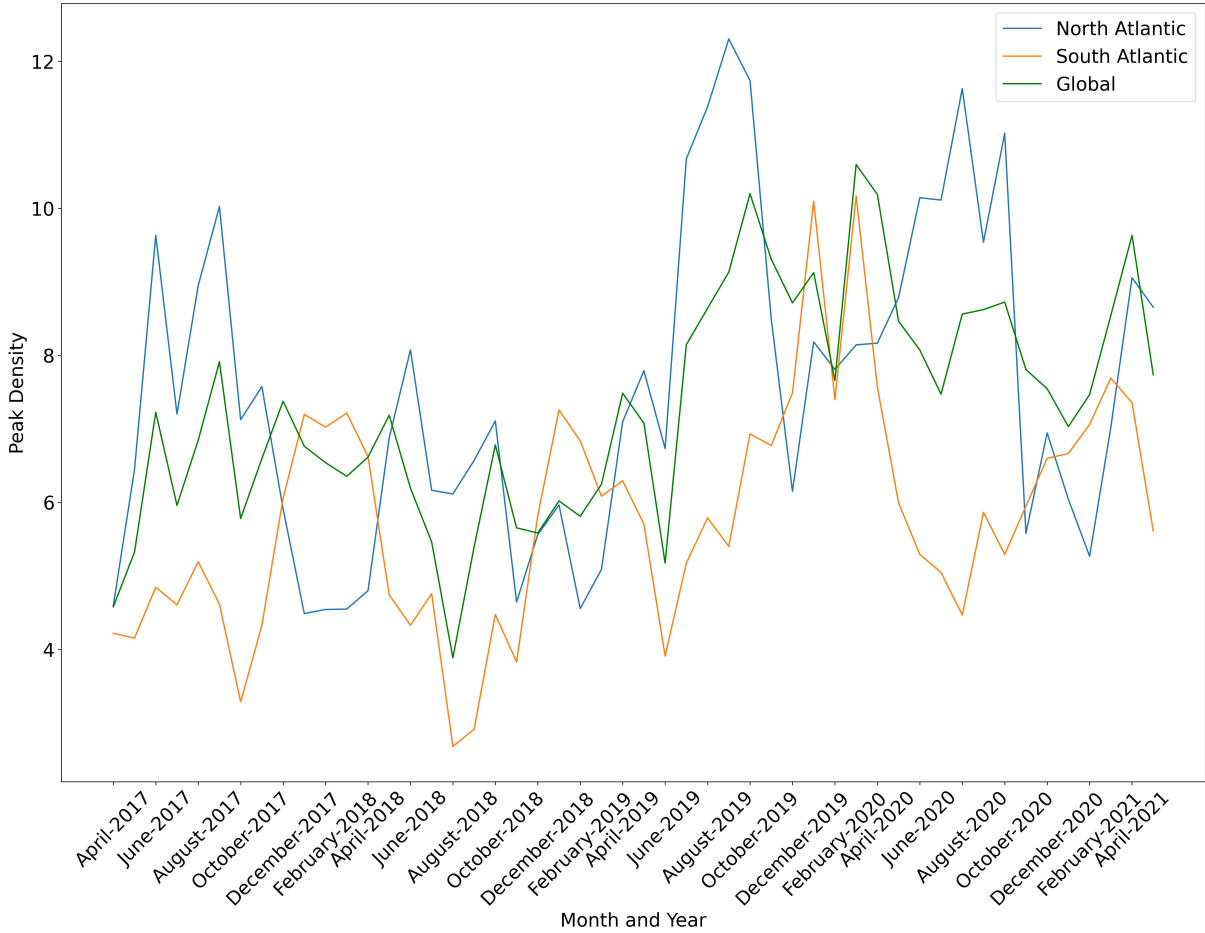


Figure 6.17: A time series showing the average grid peak density over the North- and South Atlantic ocean.

6.2.5 The Indian Ocean

For the Indian ocean basin, the boundary region is set between the latitudes 40°South to 30 °North and longitudes 30°East to 120 °East.

The figure for the comparison between the microplastic models and the global peak density is shown in figure 6.18. Here, a high concentration can be seen for the models from around 30°South and downwards. The Lebreton and van Sebille models also depict a high concentration of microplastic counts from the Bay of Bengal eastwards into the China sea. The global peak density from the CYGNSS observations shows a similar concentration of peaks around 30°South. There is also a high concentration of peaks near the island of Madagascar east of Africa and on the northeastern side of the plot, close to surrounding lands and islands. A difference observed between the models and the peak density plot is the concentration of points seen near the equator and on the southwestern tip of India. Another big difference is the area with a lower concentration of peaks near the centre of the plot.

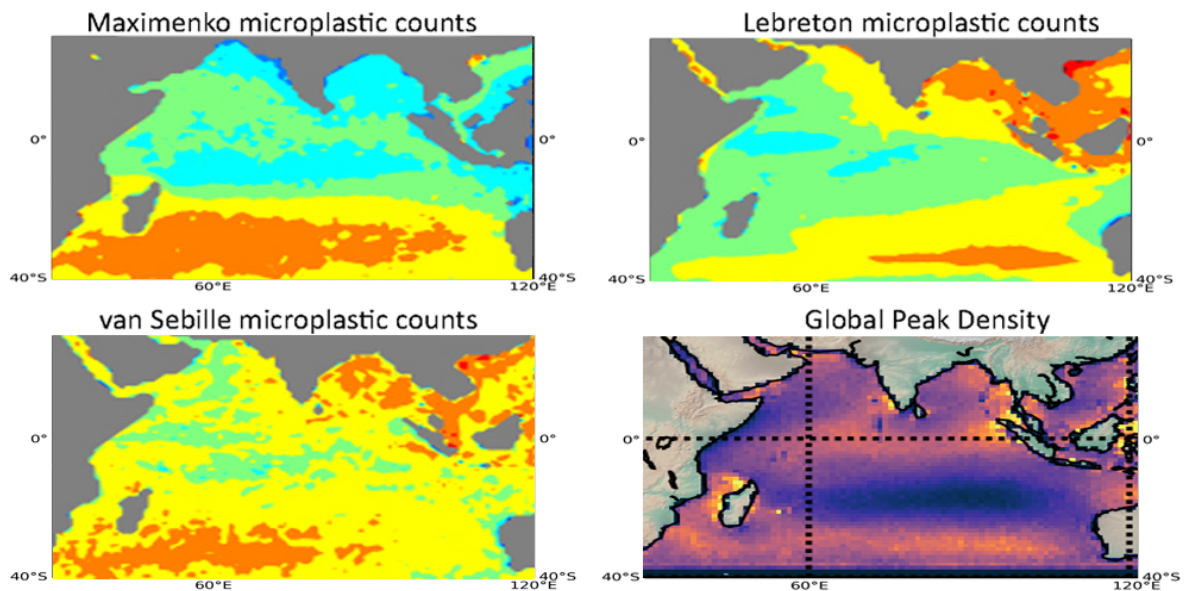


Figure 6.18: Cropped image in the Indian ocean region for the three models for microplastic counts and global peak density retrieved from the analysis of CYGNSS observations.

The plots for the peak densities of the Indian ocean are seen in figure 6.19. The Indian Ocean is the largest basin we examine, having latitudes crossing the equatorial line. For these plots, we observe a higher density and spread of peaks between October 2019 and April 2020. In addition, we observe a specially large spread in the peaks for the months October, March and April. The points seem to spread somewhat evenly throughout the region, with no significant maximum density areas, with the lowest concentration consistently in the middle part of the plots but is seemingly moving around slightly every month. We notice a high amount of peak concentration in the Bay of Bengal east of India, in the waters surrounding Madagascar and the current moving from Australia towards southern Africa.

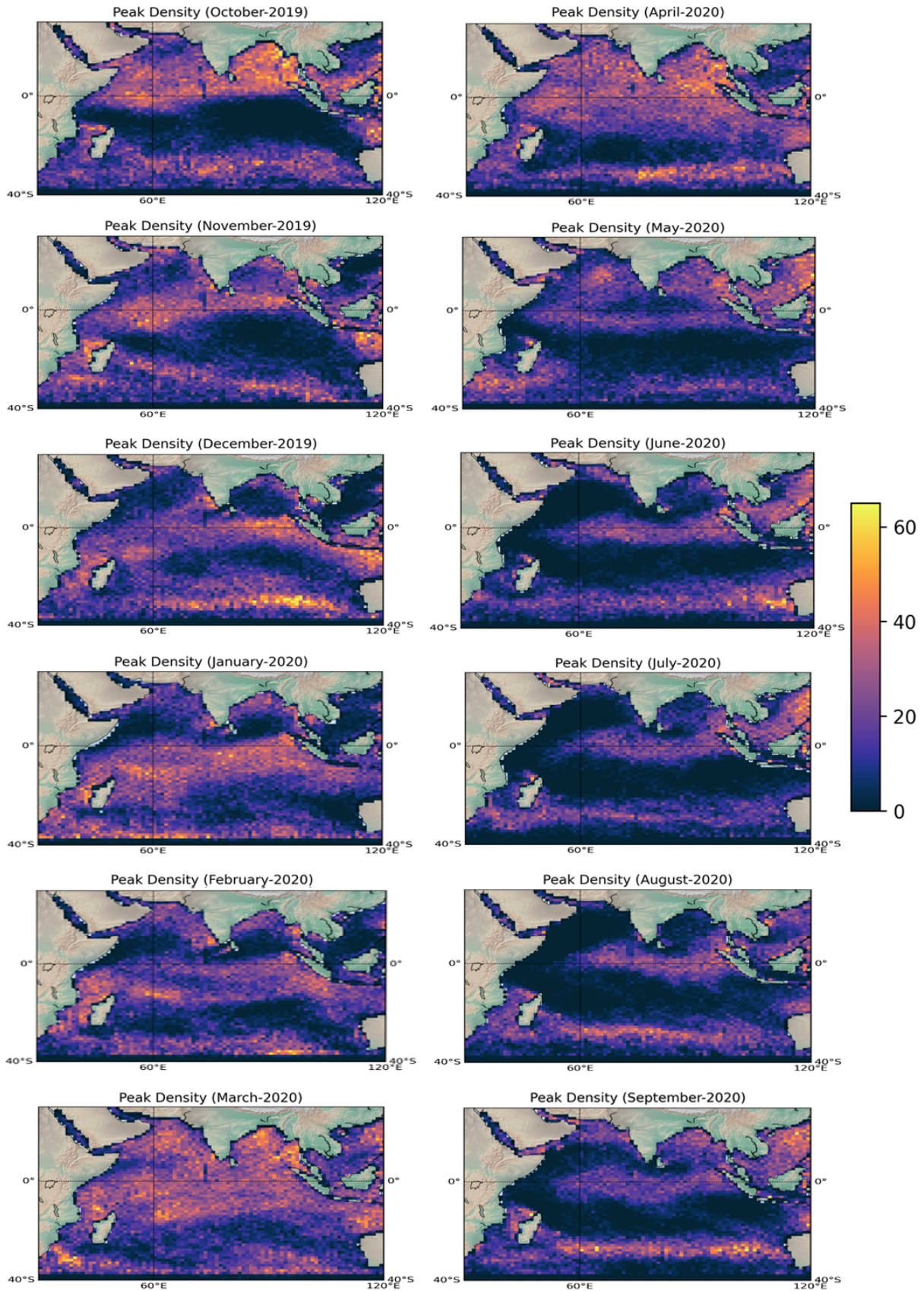


Figure 6.19: The monthly peak density over the Indian ocean region, on a $1^\circ \times 1^\circ$ grid from October 2019 to September 2020.

6.2.6 The Mediterranean Sea

Lastly, we present our observations for the Mediterranean sea, with a boundary region between latitudes 30°North to 40 °North and longitudes 6°West to 40 °East.

The comparisons between the microplastic models and the global peak density for the Mediterranean sea are found in figure 6.20. The Mediterranean sea is a special case. A high concentration of microplastic counts are seen in the Lebreton and van Sebille models. The Mediterranean sea has a relatively low sampling rate of data collected to generate the models. The high concentration for the models could be caused by the high population surrounding the sea. As the Mediterranean sea lies near the northern boundary of the CYGNSS data collection, a complete picture of the peak density could not be produced. However, looking at the global peak density plot, the area has a moderate amount of peaks.

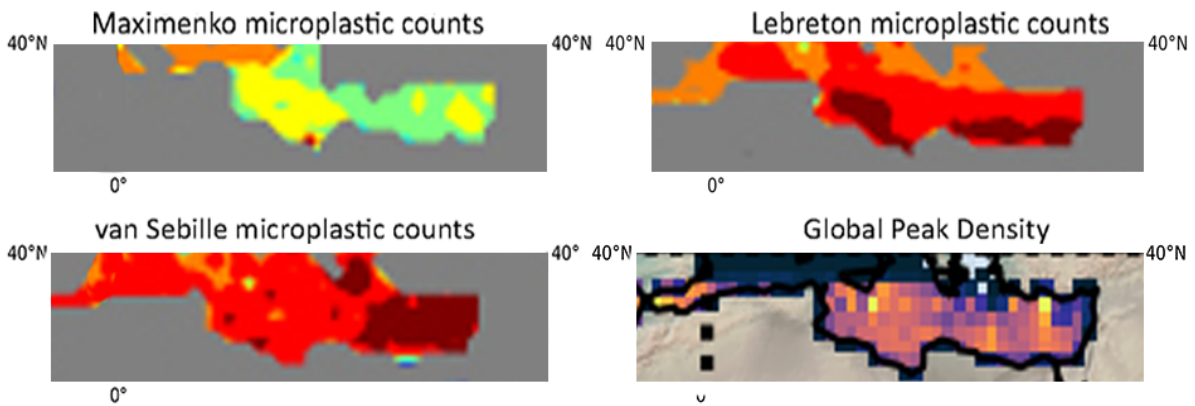


Figure 6.20: Cropped image in the Mediterranean sea region for the three models for microplastic counts and global peak density retrieved from the analysis of CYGNSS observations.

The monthly peak density plots for the Mediterranean sea are presented in figure 6.21. This is the smallest region examined, while also being surrounded by land. The high proximity to land means that it has a higher threshold for land-based noise and generally low surface currents compared to the other basins. The plots show a slightly higher concentration of peaks during October 2019 and from June to August 2020.

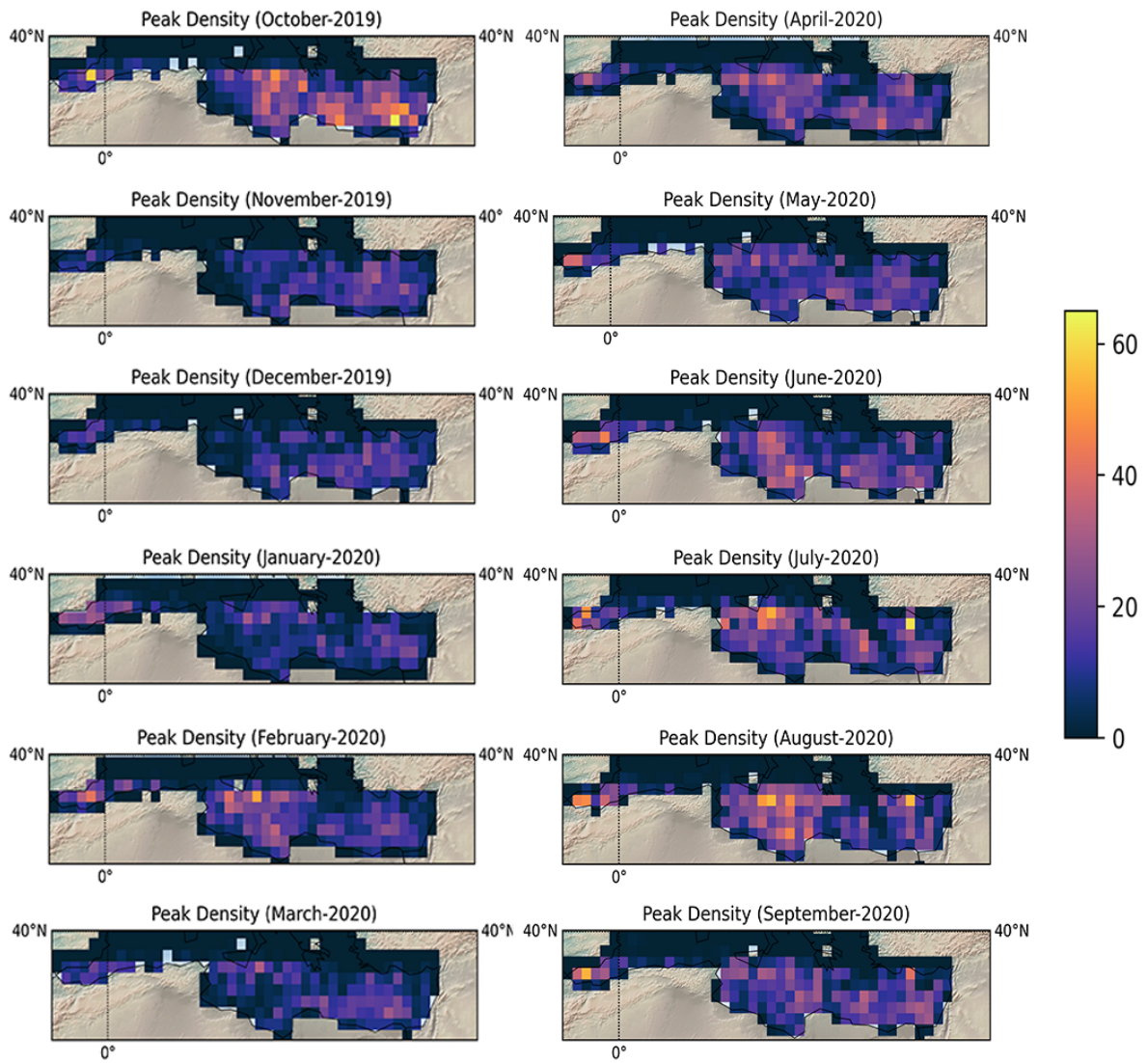


Figure 6.21: The monthly peak density over the Mediterranean ocean region, on a $1^\circ \times 1^\circ$ grid from October 2019 to September 2020.

The time series for the average grid peak density for both the Indian ocean and the Mediterranean sea are presented in figure 6.22. The time series for the Indian ocean seems to follow the trend for the global time series. This is probably because of the latitude band of the basin, spanning over both hemispheres. We can see that the lowest average density usually occurs in June. The rest of the year shows no apparent trend in the maximum density.

The time series for the Mediterranean sea show an overall lower average peak density compared to those of the oceanic basins. However, there is still a clear indication of higher densities during the warmer months. The surrounding proximity to land might cause a lower average density. Another cause is that the region is the smallest examined or due to being so far to the north that it crosses beyond the sample area of CYGNSS data collection.

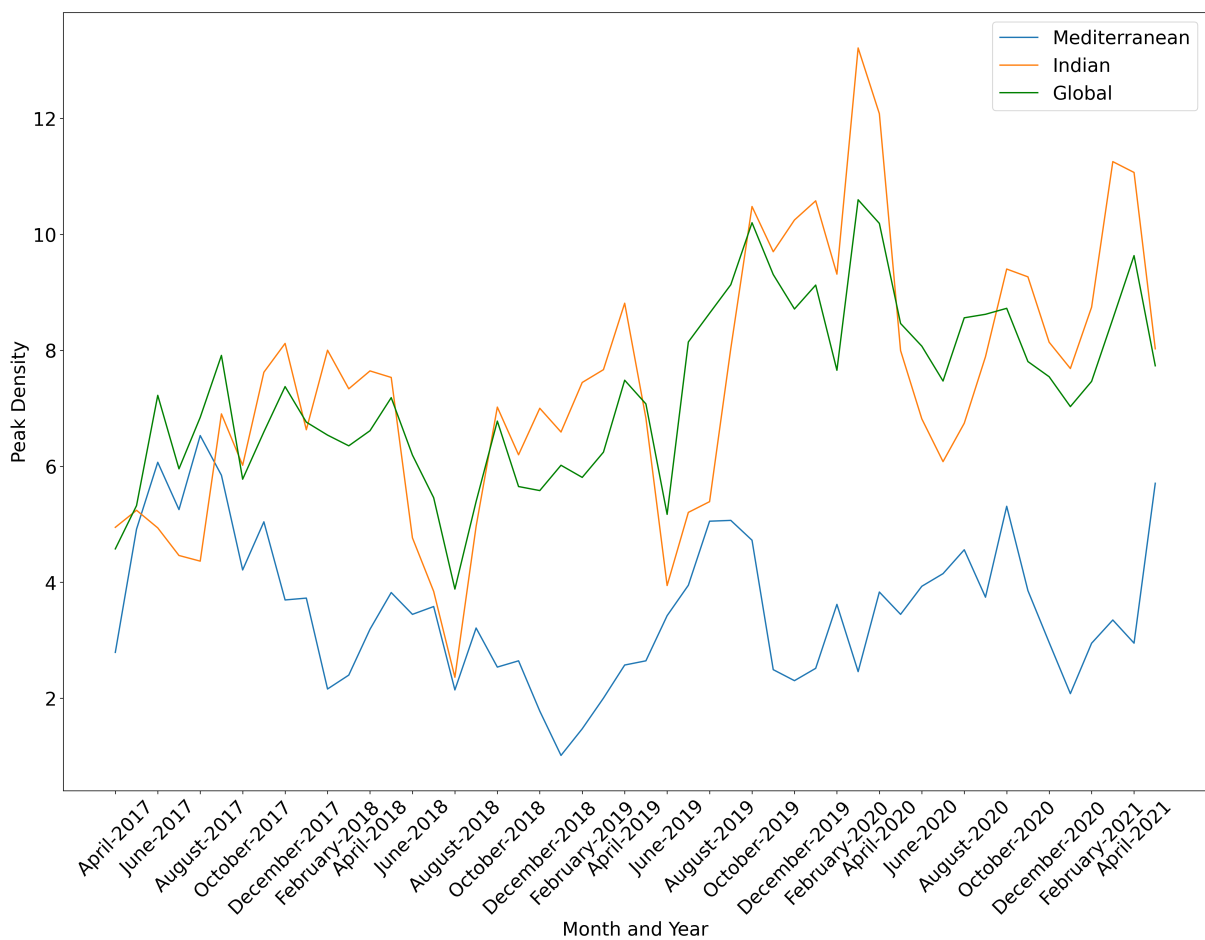


Figure 6.22: A time series showing the average grid peak density over the Indian ocean and Mediterranean sea.

Chapter 7

Conclusion

In this thesis, the applications of spaceborne Global Navigation Satellite System (GNSS) Reflectometry (GNSS-R) to monitor the distribution of microplastics on the ocean surface has been studied. The first stage of this work was designated to develop a web-based software for data representation and superficial analysis. The software includes a back-end and a front-end part, each consisting of different modules for different applications. The front-end part is designed to interact with the users and receive inputs from the user to show processing or data retrieval results. The back-end was designed to handle downloading spaceborne GNSS-R data from a remote repository and to process the data. The developed application modules include a track demonstration module, a data clipping tool, and a module for monitoring microplastics distribution.

The developed software was applied to a big dataset obtained from the NASA Cyclone GNSS (CYGNSS) mission to study the distribution of microplastics on the ocean surface. The dataset covers a period of more than four years, from March 2017 to May 2021. The analysis method for detecting microplastics is based on anomaly detection of the Normalized Bi-static Radar Cross Section (NBRCS) parameter from the CYGNSS Level-1 data products. The anomalies in the NBRCS values were investigated to spot the presence of microplastics. The assumption made for this detection approach is that the values of NBRCS would exhibit sharp peaks in the areas of highly concentrated microplastics. The logic behind this assumption is that microplastics can suppress ocean surface roughness.

Results of the analysis were compared with three recognized microplastics models, i.e. Maximenko, Lebreton, and Van Sebille. The comparison showed a good overall agreement of the results with the models, especially with the Van Sebille model. In addition, five major basins of the ocean and the Mediterranean sea were separately considered for a more detailed analysis. The study shows that based on a relatively short revisit time and full daily coverage of the CYGNSS GNSS-R mission, the monitoring of microplastics on a monthly basis is also possible for near real-time purposes.

Complementary work is suggested to investigate the impact of the surface currents, especially during low wind speeds. The effect of surface currents adds some biases since it can locally change the surface stress leading to a false alarm in the detection of microplastics.

Sources

- [1] A. L. Andrady. “Microplastics in the marine environment”. In: *Marine Pollution Bulletin* 62.8 (2011), pp. 1596–1605. DOI: <https://doi.org/10.1016/j.marpolbul.2011.05.030>.
- [2] J. Awange and J Kiema. “Environmental Geoinformatics”. In: Springer, Cham, Dec. 2018. Chap. GNSS Reflectometry and Applications, pp. 359–369. ISBN: 978-3-030-03016-2. DOI: [10.1007/978-3-030-03017-9_24](https://doi.org/10.1007/978-3-030-03017-9_24).
- [3] R. Berk. *Cannon Beach Reflections*. URL: <https://fineartamerica.com/featured/cannon-beach-reflections-rick-berk.html> (visited on 06/14/2021).
- [4] H. Bitter and S. Lackner. “First quantification of semi-crystalline microplastics in industrial wastewaters”. In: *Chemosphere* 258 (2020). DOI: <https://doi.org/10.1016/j.chemosphere.2020.127388>.
- [5] P. Blau. *CYGNSS Orbit Design*. URL: <https://spaceflight101.com/cygnss/cygnss-orbit-design/> (visited on 07/03/2021).
- [6] M. A. Browne et al. “Accumulation of Microplastic on Shorelines Worldwide: Sources and Sinks”. In: *Environmental Science & Technology* 45.21 (2011), pp. 9175–9179. DOI: [10.1021/es201811s](https://doi.org/10.1021/es201811s).
- [7] E. Cardellach and et. al. “First evidence of mesoscale ocean eddies signature in GNSS reflectometry measurements”. In: *IEEE Journal of Selected Topics in Applied Earth Observations and Remote Sensing* 13 (2019), pp. 102–112. DOI: [10.1109/JSTARS.2019.2952694](https://doi.org/10.1109/JSTARS.2019.2952694).
- [8] E. Cardellach et al. “GNSS-R ground-based and airborne campaigns for ocean, land, ice, and snow techniques: Application to the GOLD-RTR data sets”. In: *Radio Science* 46 (Oct. 2011). DOI: [10.1029/2011RS004683](https://doi.org/10.1029/2011RS004683).
- [9] E. J Carpenter and K.L Smith Jr. “Plastics on the Sargasso Sea Surface”. In: *Science* 175.4027 (1972), pp. 1240–1241. DOI: [10.1126/science.175.4027.1240](https://doi.org/10.1126/science.175.4027.1240).
- [10] J. Cartwright, C. J. Banks, and M. Srokosz. “Sea Ice Detection Using GNSS-R Data From TechDemoSat-1”. In: *JGR Oceans* 124 (2019), pp. 5801–5810. DOI: doi.org/10.1029/2019JC015327.
- [11] C. C. Chew and E. E. Small. “Soil Moisture Sensing Using Spaceborne GNSS Reflections: Comparison of CYGNSS Reflectivity to SMAP Soil Moisture”. In: *Geophysical Research Letters* 45 (2018). DOI: [10.1029/2018GL077905](https://doi.org/10.1029/2018GL077905).
- [12] K. D. Cox et al. “Human Consumption of Microplastics”. In: *Environmental Science & Technology* 53.12 (2019), pp. 7068–7074. DOI: <https://doi.org/10.1021/acs.est.9b01517>.
- [13] L. Denfall and M. Sewell. “Contributing to marine pollution by washing your face: microplastics in facial cleansers.” In: *Marine pollution bulletin* 58.8 (2009), pp. 1225–1228. DOI: <https://doi.org/10.1016/j.marpolbul.2009.04.025>.

- [14] Earth.nullschool. *Map of ocean currents*. URL: <https://earth.nullschool.net/#current/ocean/surface/currents/equirectangular> (visited on 07/10/2021).
- [15] ECMWF. *ECMWF Reanalysis v5 (ERA5)*. 2021. URL: <https://www.ecmwf.int/en/forecasts/dataset/ecmwf-reanalysis-v5> (visited on 06/16/2021).
- [16] M. C. Evans and C. S. Ruf. “Toward the Detection and Imaging of Ocean Microplastics With a Spaceborne Radar”. In: *IEEE Transactions on Geoscience and Remote Sensing* (2021), pp. 1–9. DOI: 10.1109/TGRS.2021.3081691.
- [17] J.L. Garrison, S.J. Katzberg, and M.I. Hill. “Effect of sea roughness on bistatically scattered range coded signals from the Global Positioning System”. In: *Geophysical Research Letters* 25 (13 July 1998), pp. 2257–2260. DOI: <https://doi.org/10.1029/98GL51615>.
- [18] C. Gerlein-Safdi and C. S. Ruf. “A CYGNSS-Based Algorithm for the Detection of Inland Waterbodies”. In: *Geophysical Research Letters* 46.21 (2019), pp. 12065–12072. DOI: <https://doi.org/10.1029/2019GL085134>.
- [19] R. Geyer, J. R. Jambeck, and K. L. Law. “Production, use, and fate of all plastics ever made”. In: *Science Advances* 3.7 (2017). DOI: 10.1126/sciadv.1700782.
- [20] S. Gleason. *Algorithm Theoretical Basis Document Level 1A DDM Calibration*. 2018. URL: https://clasp-research.engin.umich.edu/missions/cygnss/reference/148-0136_ATBD_L1A_DDMCalibration_Rev2_Aug2018_release.pdf (visited on 06/16/2021).
- [21] S. Gleason. *Algorithm Theoretical Basis Document Level 1B DDM Calibration*. 2018. URL: https://clasp-research.engin.umich.edu/missions/cygnss/reference/148-0137_ATBD_L1B_DDMCalibration_Rev2_Aug2018_release.pdf (visited on 06/16/2021).
- [22] C.D. Hall and R.A. Cordey. “Multistatic Scatterometry”. In: *International Geoscience and Remote Sensing Symposium, Remote Sensing: Moving Toward the 21st Century*. Vol. 1. 1988, pp. 561–562. DOI: 10.1109/IGARSS.1988.570200.
- [23] M. Hoseini et al. “First evidence of mesoscale ocean eddies signature in GNSS reflectometry measurements”. In: *Remote Sensing* 12.3 (2020), p. 542. DOI: 10.3390/rs12030542.
- [24] Y. Jia and P Savi. “Sensing soil moisture and vegetation using GNSS-R polarimetric measurement”. In: *Advances in Space Research* 59 (2017), pp. 858–869. DOI: 10.1016/j.asr.2016.11.028.
- [25] B. Jovanović. “Ingestion of microplastics by fish and its potential consequences from a physical perspective”. In: *Integrated Environmental Assessment and Management (IEAM)* 13.3 (2017), pp. 510–515. DOI: <https://doi.org/10.1002/ieam.1913>.
- [26] T. M. Karlsson et al. “The unaccountability case of plastic pellet pollution”. In: *Marine Pollution Bulletin* 129.1 (2018), pp. 52–60. DOI: <https://doi.org/10.1016/j.marpolbul.2018.01.041>.
- [27] S. J. Katzberg et al. “Utilizing calibrated GPS reflected signals to estimate soil reflectivity and dielectric constant: Results from SMEX02”. In: *Remote Sensing of Environment* 100 (2006), pp. 17–28. DOI: <https://doi.org/10.1016/j.rse.2005.09.015>.
- [28] J. H. Kramer. *DMC-1G (Disaster Monitoring Constellation- First Generation) Missions*. 2020. URL: <https://directory.eoportal.org/web/eoportal/satellite-missions/d/dmc> (visited on 06/18/2021).
- [29] David W. Laist. “Impacts of Marine Debris: Entanglement of Marine Life in Marine Debris Including a Comprehensive List of Species with Entanglement and Ingestion

- Records”. In: 1997, pp. 99–139. ISBN: 978-1-4613-8486-1. DOI: 10.1007/978-1-4613-8486-1.
- [30] K. M. Larson et al. “GPS Multipath and Its Relation to Near-Surface Soil Moisture Content”. In: *IEEE Journal of Selected Topics in Applied Earth Observations and Remote Sensing* 3 (2009), pp. 91–99. DOI: 10.1109/JSTARS.2009.2033612.
- [31] A. Lusher, P Hollman, and J. Mendoza-Hill. “Microplastics in fisheries and aquaculture: Status of knowledge on their occurrence and implications for aquatic organisms and food safety”. In: *Food and Agriculture Organization of the United Nations* 615 (2017). URL: <http://www.fao.org/3/i7677e/i7677e.pdf>.
- [32] J. Lynch. *The Plastic That Washes Up on Hawaii’s Beaches Affects Me. Personally*. URL: <https://www.nist.gov/blogs/taking-measure/plastic-washes-hawaiis-beaches-affects-me-personally> (visited on 06/14/2021).
- [33] M. Martin-Neira. “A Passive Reflectometry and Interferometry System (PARIS): Application to ocean altimetry”. In: *ESA Journal* 17 (Jan. 1993), pp. 331–355.
- [34] N. Maximenko et al. “Toward the Integrated Marine Debris Observing System”. In: *Frontiers in Marine Science* 6 (2019), p. 447. ISSN: 2296-7745. DOI: 10.3389/fmars.2019.00447.
- [35] C. J. Moore et al. “A Comparison of Plastic and Plankton in the North Pacific Central Gyre”. In: *Marine Pollution Bulletin* 42.12 (2001), pp. 1297–1300. DOI: [https://doi.org/10.1016/S0025-326X\(01\)00114-X](https://doi.org/10.1016/S0025-326X(01)00114-X).
- [36] NOAA. *Proceedings of the International Research Workshop on the Occurrence, Effects, and Fate of Microplastic Marine Debris*. 2008. URL: <https://repository.library.noaa.gov/view/noaa/2509> (visited on 06/17/2021).
- [37] Kershaw P.J and Rochman C.M. “Sources, fate and effects of microplastics in the marine environment: part two of a global assessment”. In: *GESAMP* 93 (2016). URL: <http://www.gesamp.org/site/assets/files/1275/sources-fate-and-effects-of-microplastics-in-the-marine-environment-part-2-of-a-global-assessment-en.pdf> (visited on 06/17/2021).
- [38] NASA PO.DAAC. *Cyclone Global Navigation Satellite System (CYGNSS)*. URL: <https://podaac.jpl.nasa.gov/CYGNSS> (visited on 06/18/2021).
- [39] L. M Rios, C Moore, and P. R Jones. “Persistent organic pollutants carried by synthetic polymers in the ocean environment”. In: *Marine Pollution Bulletin* 54.8 (2007), pp. 1230–1237. DOI: <https://doi.org/10.1016/j.marpolbul.2007.03.022>.
- [40] A. Rius and E Cardellach. “Springer Handbook of Global Navigation Satellite Systems - Signals and Modulation”. In: May 2017. Chap. 40. Reflectometry, pp. 1163–1185. ISBN: 978-3-319-42926-7. DOI: 10.1007/978-3-319-42928-1_4.
- [41] N. Rodriguez-Alvarez et al. “Soil Moisture Retrieval Using GNSS-R Techniques: Experimental Results Over a Bare Soil Field”. In: *IEEE Transactions on Geoscience and Remote Sensing* 47 (2009), pp. 3616–3624. DOI: 10.1109/TGRS.2009.2030672.
- [42] C. S. Ruf et al. “A New Paradigm in Earth Environmental Monitoring with the CYGNSS Small Satellite Constellation”. In: *Scientific Reports* 8.8782 (2018). DOI: 10.1038/s41598-018-27127-4.
- [43] C. S. Ruf et al. *CYGNSS Handbook*. Apr. 2016. ISBN: 978-1-60785-380-0.
- [44] E. van Sebille and et al. “The physical oceanography of the transport of floating marine debris”. In: *Environmental Research Letters* 15.2 (2020). DOI: 10.1088/1748-9326/ab6d7d.

- [45] E. van Sebille et al. “A global inventory of small floating plastic debris”. In: *Environmental Research Letters* 10.12 (2015). DOI: 10.1088/1748-9326/10/12/124006.
- [46] H. Seo, A. J. Miller, and J. R. Norris. “Eddy–Wind Interaction in the California Current System: Dynamics and Impacts.” In: *Journal of Physical Oceanography* 46 (2016). DOI: doi:10.1175/JPO-D-15-0086.1.
- [47] *The Science of Microplastics in the World Ocean*. URL: <https://microplastics.whoi.edu/the-science-of-microplastics-in-the-world-ocean-international-workshop/> (visited on 06/14/2021).
- [48] UCAR. *Network Common Data Form (NetCDF)*. 2021. URL: <https://www.unidata.ucar.edu/software/netcdf/> (visited on 06/29/2021).
- [49] A. et al. Verschoor. *Quick scan and Prioritization of Microplastic Sources and Emissions*. 2014. URL: <https://www.rivm.nl/bibliotheek/rapporten/2014-0156.pdf> (visited on 06/17/2021).
- [50] W. Wan et al. “Using CYGNSS Data to Monitor China’s Flood Inundation during Typhoon and Extreme Precipitation Events in 2017”. In: *Remote Sensing* 11.7 (2019). DOI: 10.3390/rs11070854.
- [51] S. L. Wright and F. J. Kelly. “Plastic and Human Health: A Micro Issue?” In: *Environmental Science & Technology* 51.12 (2017), pp. 6634–6647. DOI: <https://doi.org/10.1021/acs.est.7b00423>.
- [52] V. Zavorotny and C. S. Ruf. *Algorithm Theoretical Basis Document Level 2 Mean-Square Slope Retrieval*. 2016. URL: <https://clasp-research.engin.umich.edu/missions/cygnss/reference/148-0139%20L2%20MSS%20ATBD%20R3.pdf> (visited on 06/22/2021).

